universität wien

MASTERARBEIT | MASTER'S THESIS

Titel | Title

The α-to-β transition in human hair investigated by in-situ SAXS.

verfasst von | submitted by

Amélia Garance Pellicier

angestrebter akademischer Grad | in partial fulfilment of the requirements for the degree of

Master of Science (MSc)

Wien | Vienna, 2026

Studienkennzahl lt. Studienblatt | Degree programme code as it appears on the student record sheet:	UA 066 876
Studienrichtung lt. Studienblatt | Degree programme as it appears on the student record sheet:	Masterstudium Physics
Betreut von | Supervisor:	Univ.-Prof. Mag. Dr. Herwig Peterlik

Acknowledgments

First of all, I would like to thank my supervisor for this thesis, Univ.-Prof. Dr. Herwig Peterlik, for the opportunity to work on this topic, for the time he took to answer every questions I had, and for the support and advice he gave whenever I needed, especially during the discussion about the results and for the abstract. He always gave me the possiblility and the ressources to discover and deepen new topics and concepts.
I would also like to thank Martin Haßler for his unfailing help throughout the thesis from providing the samples to the data analysis including his valuable assistance with the programms I used and the setup installation, all accompanied by surprinsing musical tastes.
All measurements were taken at the Faculty Center for Nano Structure Research at the University of Vienna. I acknowledge support by the group and especially Stefan Puchegger, for his availability and valuable help in IT-support.

I would then like to thank my friends, my boyfriend and my siblings, who helped me maintain my motivation and confidence throughout the thesis and my master's degree in general. I want to thank all my friends who, even from hundred of kilometers away, supported me and have always been by my side over the past years.
I thank, of course, my family for the trust they have always had in me and the strength they have always given me to pursue my studies.

I am sure that, as always when it is time for acknowledgments, I am forgetting to thank people without whom this thesis could not have existed as it is, and I thank them all warmly.

Table of contents

1. Introduction **1**
- 1.1. Motivation . . . 1
- 1.2. State of the art . . . 1
  - 1.2.1. The α-to-β transition in WAXS patterns . . . 2
  - 1.2.2. Role of stress in the α-to-β transition process . . . 3
  - 1.2.3. Role of humidity in the α-to-β transition process . . . 3
  - 1.2.4. Role of temperature in the α-to-β transition process . . . 4
  - 1.2.5. Limitations by the inner structure (cuticle and core) . . . 4
- 1.3. Limitations and modifications of the set-up . . . 4

2. Theoretical background **9**
- 2.1. Biological material: hair . . . 9
- 2.2. X-ray radiation and production . . . 10
  - 2.2.1. Different types of filament tubes. . . . 12
- 2.3. Principle of scattering . . . 13
  - 2.3.1. Reciprocal space and lattice basis . . . 13
  - 2.3.2. Elastic scattering . . . 14
  - 2.3.3. Powder diffraction . . . 15
  - 2.3.4. Atomic form factor . . . 15
  - 2.3.5. Structure factor . . . 16
- 2.4. Mechanical behaviour . . . 17
  - 2.4.1. Stress-strain curve . . . 17
  - 2.4.2. Loading process . . . 18

3. Experimental set-up **19**
- 3.1. Samples . . . 19
- 3.2. In-situ measurement facility . . . 20
  - 3.2.1. Chamber . . . 20
  - 3.2.2. Tensile-test machine . . . 20
  - 3.2.3. Humidity control . . . 21
  - 3.2.4. SAXS equipment . . . 22
  - 3.2.5. Detector Dectris Eiger2 R 500k . . . 22
- 3.3. Measurement time and procedure . . . 23

4. Data evaluation procedure **25**
- 4.1. Choice of the glue . . . 25
- 4.2. Calibration . . . 26
- 4.3. Integration procedure . . . 26
- 4.4. Background subtraction . . . 26
  - 4.4.1. Measured background and transmission . . . 26
  - 4.4.2. Normalisation . . . 27
  - 4.4.3. Sample background . . . 28
- 4.5. Background at different positions . . . 29
- 4.6. Fitting procedure . . . 29

5. Results **33**
- 5.1. Stress-strain curves . . . 33
- 5.2. Comparison of the peak analysis here and in literature . . . 35
- 5.3. Uncertainties . . . 36
- 5.4. Results for the series at 20% relative humidity . . . 37
  - 5.4.1. Peak position . . . 37

5.4.2. Peak intensities 39
5.5. Results for the series at 40% relative humidity 41
5.5.1. Peak position 41
5.5.2. Peak intensity 42
5.6. Results for the series at around 50% relative humidity 44
5.7. Results for the series at 60% relative humidity 45
5.7.1. Peak position 45
5.7.2. Peak intensity 47
5.8. Results for the series at 80% relative humidity 49
5.8.1. Peak position 49
5.8.2. Peak intensity 51

6. Discussion **55**

Abstract **58**

Kurzfassung **59**

References **63**

List of Figures **65**

A. Appendix **i**
A.1. Results of the series at 50% RH i
A.2. Uncertainties calculation iv
A.2.1. Python code iv
A.3. Programm for background subtraction vii

1. Introduction

1.1. Motivation

Hair is a biological material present in many species living in different environments. It plays a large number of roles such as protection against temperature changes, protection against injuries, camouflage or even distinctions between females and males. It is also in some cases important for the normal functioning of skin.
It is in human societies a strong social and identity marker and all the various treatments that are often daily used can have a strong effect on the structure. For these reasons the haircare industry develops products and investigates properties of hairs to learn about the effect of treatments and stress.
The hierarchical structure of hair at different scales from about 100 µm to 2 nm makes scattering analysis a powerful tool for its investigation [1], and it allows to investigate microscopic changes and properties of proteins such as keratin in natural surrounding.

Proteins and more specifically keratin has been investigated for about one century in order to understand and find a model for the relation of structure and mechanical properties. In particular, the transition from α-helices to a β-sheets structure has been observed under specific conditions: stress, humidity, presence of steam and high temperatures change the protein conformation.

The present thesis aims to examine the possibility to observe the α- to β-transition in-situ only under stress and humid environment in the SAXS facility at University of Vienna and whether there are thresholds on these two parameters for the transition. It is based on the thesis written by Johannes Liebhart MSc and, buoyed by its results, tries to overcome the limitations and challenges of this work.
This could be achieved by the reconstruction of the humidity chamber with a newly developed window, which allowed for a significant reduction of the scattering background.

1.2. State of the art

Hair is a rich and complex material, resistant to strain, and protecting mammals from heat, cold and humidity. While for humans, its role in survival in harsh conditions is not essential anymore, it remains surprisingly strong and of great interest. Its highly ordered structure at different scales has aroused curiosity, whether to understand the origin of the fibre's properties or to study the effects of the environment on these properties. Thanks to modern investigation techniques, we can now describe the structure at different scales, including the in-vivo molecular conformation of keratin.
Keratin in hair has been studied for more than one century to establish a model for these molecules and to investigate the transition of the conformation of the polymer from an α- to a β- configuration [1]. Whereas the α-configuration is the native state in the fibre, molecules in the fibre's core undergo structural transformations when the hair is subjected to certain conditions, that can lead to some molecular and structural rearrangements. Due to the regular arrangement of keratin in the transverse as well as the longitudinal direction of the fibre, X-ray scattering gives key information about the structure and is a non-destructive technique allowing measurements on fibres placed under specific conditions.

1.2.1. The α-to-β transition in WAXS patterns

A model has been proposed for the two conformations that present a regular arrangement of structures and can be investigated using X-ray scattering techniques [2]. This model has of course been adapted and refined but is now generally accepted. What remained under investigation for a longer time was the exact process of the transition between the two configurations.
The q-range for the keratin structure corresponds to the wide-angle scattering region (WAXS) and the pattern shows a meridian sharp peak at 0.515 nm, superimposed with a broader arc at 0.5 nm. These correspond respectively to the α-helix pitch and to the less-ordered coiled-coil domain. The large high-intensity spot at 0.96 nm is shared by the α- and the β-configuration and arises from the distance between the helices for the α-configuration and between the sheets for the β-configuration. [3]
The β-structure is characterised by the vanishing of the meridian peak at 0.515 nm and by the presence of two peaks in the meridian at 0.333 nm and one on the equatorial direction at 0.465 nm. The peak at 0.95 nm remains. The presence of these three peaks is necessary to ensure that the keratin is in its β-configuration [4, 5, 6, 3].
The peak at 0.333 nm corresponds to the distance between the residues, regularly arranged along the β-sheet structure. The 0.465 nm reflection corresponds to the inter-sheet distance (governed by hydrogen bonding between the atoms). The reflection at 0.98 nm remains in both configurations, suggesting a similar distance between the α-helix strands and the β-sheets.
Figure 1.1 is from the paper by Kreplak et al. (2001) [4] and shows the pattern for (a) the wide-angle region and (b) the small-angle region for the α-helix structure, and (c) the wide-angle region for the β-sheets.

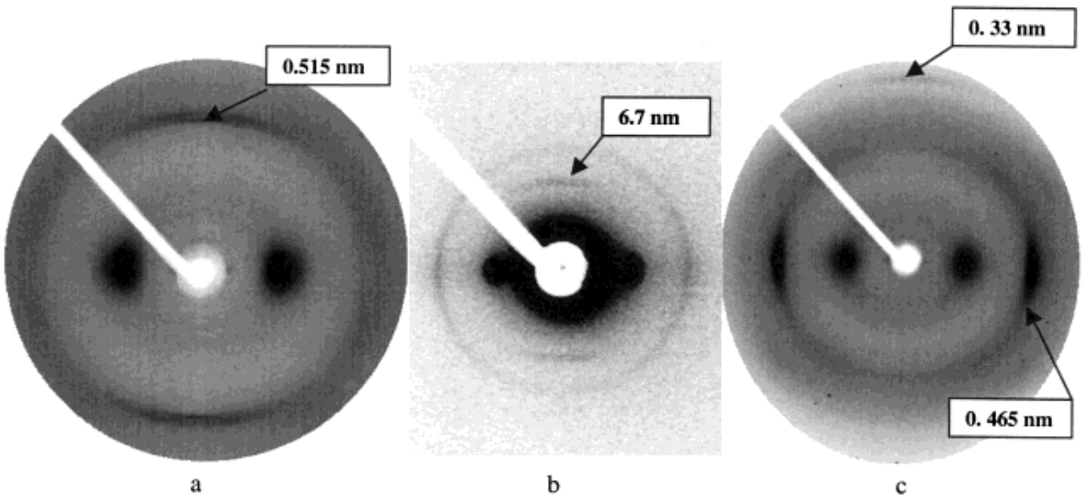

Figure 1.1.: Taken from [4]:«(a) Typical wide angle X-ray scattering (WAXS) pattern of hard α-keratin (horse hair).
The fine 0.515 nm arc is visible on the meridian (vertical) above a broader arc around 0.5 nm, whereas the broad 0.98 nm maximum appears on the equator (horizontal). Notice the weak and diffuse ring around 0.45 nm. (b) Typical small angle X-ray scattering (SAXS) pattern of hard α-keratin (horse hair). The 6.7 nm arc is visible on the meridian (vertical). Our sample was oriented perpendicular to the beam with an error of $\pm 2^\circ$ for the SAXS experiments; this is smaller than the natural angular extent ($\pm 10^\circ$) of the 6.7 nm reflection. The intense ring is due to lipid scattering. (c) Typical WAXS pattern of β-keratin (horse hair stretched to 100% extension in steam). The 0.333 nm arc is visible on the meridian (vertical), whereas the 0.465 nm arc appears on the equator (horizontal) together with a broad 0.96 nm maximum.»

1.2.2. Role of stress in the α-to-β transition process

The process of the transition is a progressive one, described by different authors [2, 7, 3, 4] [4], all of them being consistent with certain necessary conditions, the indispensable condition being a strain applied to the fibre. The easiest method in experimental protocols is an elongation of the hair in the longitudinal direction, or, in other words, simply pulling on the fibres.
In the papers describing this behaviour, the keratin configuration is described with respect to the stress or the strain of the hair. Therefore, the progressive transition is assigned to the different regions of the stress–strain curve.
At small deformations, the fibre exhibits a linear-elastic behaviour (Hookean region) [8], during which the α-helices are deformed and stretched but undergo no structural changes. During this elastic transformation at low extension, the process is reversible, without residual stress even after several extension and recovery cycles, is to be noticed [6].
This elastic transformation is reported to happen up to an elongation of the fibre between 2% and 5%. Then the fibre is further elongated and enters the yield region until about 30% extension of its initial length, to then enter the post-yield region above 30%. Different papers report the α-to-β transition to start when the fibre enters the yield region [1, 5, 7]. During yielding, the α-helices progressively uncoil and reorganize into β-sheets [6, 5]. This region is characterised by a large strain increase with only a small stress, and the coexistance of the two configurations in the fibre at the same time [9].
The transition does not appear to happen uniformly over the length or the cross section. Only at the end of the yield region is the keratin fully changed into β-sheets all along the length [7]. The β-sheets formation starts in the core and propagates to the outside of the fibre, and the β-sheet content varies linearly with the applied strain in this region [3].

Further beyond is the so-called post-yield region, characterised by a second, stronger increase in strain and bond breakages leading to the breakage of the fibre at the macroscopic scale [8].

1.2.3. Role of humidity in the α-to-β transition process

Stress is, as described above, the key parameter for the transition to happen, but the presence of water in the hair changes the mechanical properties of the molecules and hence has an impact on the transition. For hair from different species and also within one species from one individual to another, the permeability varies, but when humidity penetrates the inner parts of the fibres, the structural bonds are in general weakened.
According to Yan Yu et al. [6], the water in hair fibres, in addition to swelling the overall diameter, reduces the interaction between the protein chains and thus increases the mobility of the structure.
This softening of the α-helix is clearly visible in the stress-strain curve with a much higher yield stress for low relative humidity (20%) than for 50% to 100% [6], meaning that keratin loses its resistance and the bonds are destroyed or damaged with lower stress. Wet hair breaks at lower stress but at higher strain than dry hair. The Hookean region is shorter and the plateaued yield region is larger for wet fibres [1].
Steam has also been used in several experiments. Jinan Cao observed the transition for fibres stretched wet and placed in steam for 20 minutes after [5]. Astbury and Street were able to extend the fibres three times more in steam than in dry conditions [1].
With these observations, one can argue that water makes the transition to the β-structure easier and makes the hair more susceptible to respond to stress and to suffer longer-term damage.

Also interesting to note is the impact of water on the relaxation behaviour of stretched hairs: after elongating the fibres, Bendit placed the fibres to relax in water at 50 °C. No change in the configuration could be measured for fibres extended between 0% and

20% in 60% humidity and 20 °C environment, nor for the one extended between 0% and 40% with humidity of 100% and temperature of 20 °C. The peak at 5.1 Å decreases but the one at 4.65 Å does not appear [2]. Astbury and Street also noticed that wet hair returned easily to its original length [1].

1.2.4. Role of temperature in the α-to-β transition process

High temperature damages the cuticle and leads to earlier breakage of the fibre [6]. Temperature can also influence the parallel or antiparallel character of the conformation, as wet hair stretched by 40% to 50% in water at 21 °C presents parallel β-sheets and presents anti-parallel β-sheets in water at 95 °C [10]. This parameter will, however, not be further discussed in this thesis.

1.2.5. Limitations by the inner structure (cuticle and core)

Let us focus now again on the strain parameter needed to trigger the transition. The strain is applied longitudinally to the hair and implies stress on the inner structure. The stress-strain curve shows the response of the fibres to extension but doesn't give information on the influence of the different parts of the hair. It is indeed a composite material with three main distinct parts: the cuticle on the outermost region, the cortex, and the medulla in the center, which is not always present and is a more hollow region (see Figure 2.1). The keratin of interest is contained in the cortex [6] and it is necessary to make sure the cuticle does not play a significant role in the resulting stress of the stretched fibre, so that the keratin molecules experience most of the stress.

First of all, the volume of the cuticle is significantly smaller than that of the core [11]. If both parts had similar Young's moduli, the stress would be taken up mainly by the core but since the mechanical properties of each part separately are not known, it is appropriate to compare the mechanical properties with and without the part that is the easiest to remove. Astbury and Street [1] mechanically damaged the outer part of the fibres, peeling it off using powdered glass. The fibres were then left to rest in water for relaxation, and tested again for tensile properties. It appeared that the tensile properties with or without damaging the cuticle remained unchanged.
In [12], the tensile properties of untreated fibres and of fibres chemically treated with dipersephthalic acid, which strongly damages the cuticle, were compared, and no differences were observed. The fibres were subjected to repeated treatment and observed with SEM to confirm the effective damage to the cuticle. From the first treatment deterioration of the cuticle is noticeable in the SEM, while no changes in tensile properties are observed.
Mechanical and chemical treatments were combined in another experiment [10]. The cuticle was removed using sandpaper and the fibre was treated with ether and ethanol and once again no change was observed compared with the untreated fibre.

These three procedures and their corresponding results suggest a predominance of the core of the fibre in its behaviour during stretching, which on one hand allows to use fibers without needing to treat them to remove the outer part an on the other hand, the fibers don't need to be stored or protected espacially from eventual damage of the cuticle before measurement.

1.3. Limitations and modifications of the set-up

This thesis aims to solve a few problems in the set-up from the Master's thesis "In-situ Measurement of the α-to-β Transition in Human Hair under Varying Conditions" by Johannes Liebhart MSc [13].

The following sections summarise these experimental shortcomings:
One of the problems encountered was the kapton exit window of the humidity chamber:

the kapton presents a strong scattering peak in the range of the keratin pattern, which is much weaker and completely overshadowed by the kapton peak.
Besides, the window was quite small and could not offer a complete view in one direction in the high-q region.

In the previous thesis, image plates were used as detectors. Two slightly different plates are alternatively used to reduce the time loss between two measurements. But this requires evaluating the images from each plate separately, measuring one background and one calibration for each. This is an obstacle to automatisation and leads to possible additional offset within one series.
The image plates need to be manually changed and read-out after each measurement: this is time-consuming and increases the risk of human mistakes. Additionally, the reader has sometimes positioning and pixel errors which is overcome by either reading-out the plate a second time or shifting the reading area. After that the images must be re-shifted to re-match the beam centers before any evaluation. This is done by eye and is another source of imprecision. When it is possible to only read the images a second time the signal is weaker which is problematic for measurements of biological materials presenting low signal and background from amorphous regions.

To overcome those problems, the exit window has been changed to the size of the chamber and made of plastic backing foil, which is, different to the kapton foil, mainly amorphous. The patterns obtained with the old and new setups are shown in Figure 1.2.
To be noted is the rotation by 90° of the pattern with the Dectris detector on Figure 1.2c and with image plates on Figure 1.2b: the horizontal direction for one coresponds to the vertical direction in the other one.
The first pattern is the pattern from Johannes Liebhart's thesis and the circular window is obscurring the righten part of the pattern. Two sharper and more intense arcs are clearly visible, overlapping the sample peaks, see Figure 1.2a.
Differently, the second pattern obtained after set-up modifications has a higher signal intensity and the window border is larger than the complete pattern of the hair. The pattern is not cut off anymore, and most importantly the foil doesn't have any strong peak but only a faded ring of intensity in the order of the sample pattern and not at the exact same position than the peak of the data in Figure 1.2b. This is therefore a strong improvement since it can simply be removed during the background subtraction.

After a series measured with image plates, the detector used in this thesis for evaluation is a Dectris 500K and the pattern produced is showns in Figure 1.2c. The background from the chamber is once again much lower and the spots are clearly visible with bare eyes. These two improvements will be reflected after integration, giving smoother and clearer integrated data (Figure 1.3). Figure 1.3a shows the waterfall plot of the integrated data from Johannes Liebhart's thesis, for which the kapton window peak clearly overrides the signal between $13\,\mathrm{nm}^{-1}$ and $14.5\,\mathrm{nm}^{-1}$. The waterfall plot of the pattern recorded with the Dectris detector and the new chamber window in Figure 1.3b is possible to analysis from the region of the direct beam until the end of the pattern at about $25\,\mathrm{nm}^{-1}$.

Another advantage of the Dectris detector over the image plate is its full automatisation, with the possibility to run the measurements overnight, to open the chamber only once to remove the sample for the background measurement and the same relative position to the sample.
On the other hand, the Dectris detector is smaller than the image plates and prevents the analysis of both the meridional and equatorial direction. In this thesis only the equatorial part of the pattern will be considered. To have access to the other direction another set of measurement needs to be done, with the detector rotated by 90° and its long axis being oriented vertically. Also a new set of samples is required. This limitation also needs to be kept in mind and gives some limits to the full automatisation of the Dectis detector and raises the question of the reproducibility of the samples since

the transition under the same conditions would be investigated with different samples.

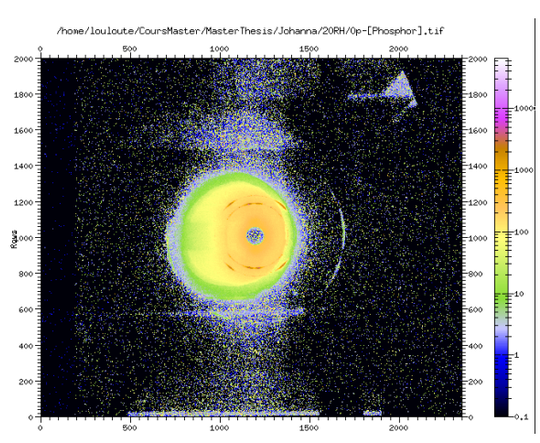

(a) From Liebhart's data [13]: (Pattern with the old set-up with image plates.

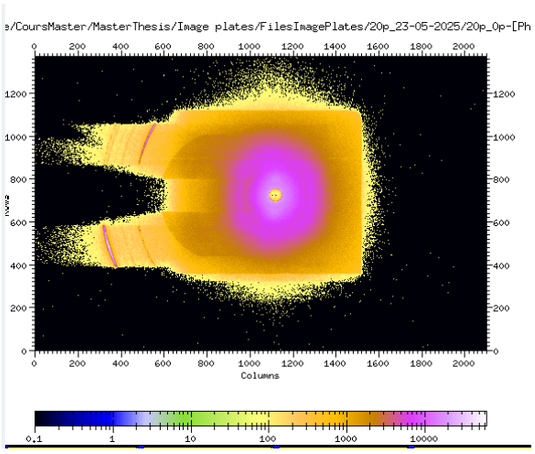

(b) Pattern with the new set-up and the image plate.

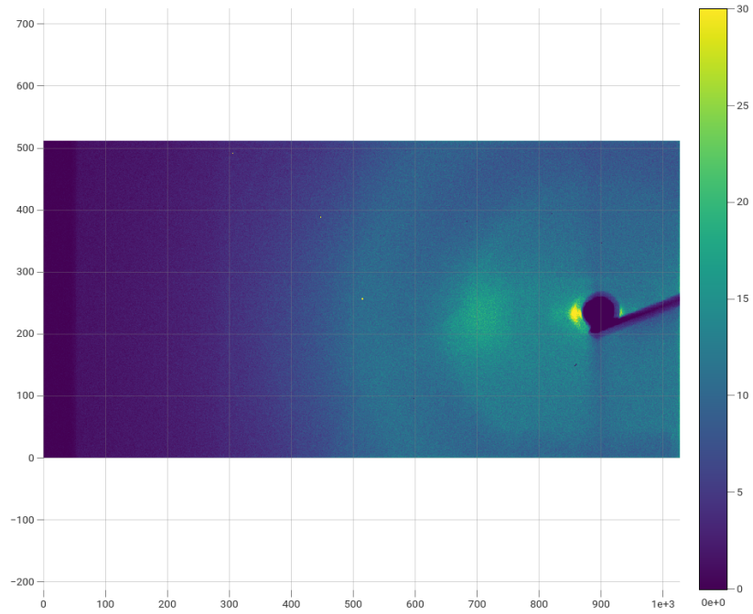

(c) Pattern with the new set-up and Dectris detector.

Figure 1.2.: Comparison of the 2-D patterns with the old and the new set-up with a relative humidity of 20% at 0% extension. The high intensity Kapton peak between $q = 13\,\mathrm{nm}^{-1}$ and $14.5\,\mathrm{nm}^{-1}$in Fig. 1.2a from Liebhart's thesis is clearly absent in the new set-up in the corresponding range $q = 1.3$ to $1.45\,\mathrm{\AA}^{-1}$ in Fig. 1.2b. Important to note is the rotation by 90° between the images from the image plates and from the Dectris detector.

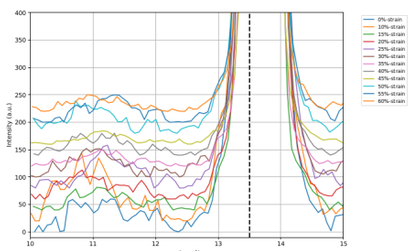

Figure 4.13.: Waterfall plot of the measurement series at 40% relative humidity in horizontal orientation. The vertical line shows the location of the expected peak at $q = 13.5$ nm^{-1}.

(a) From Liebhart's thesis (page 34)[13]: Integration of equatorial direction at 20% humidity and successive elongation with previous set-up.

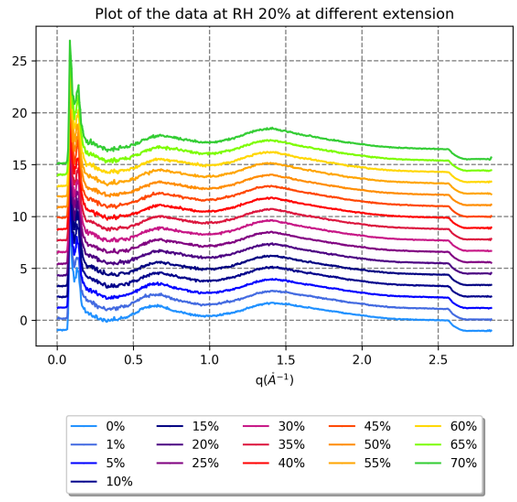

(b) Integration of equatorial direction at 20% humidity and successive elongation with new set-up and Dectris detector.

Figure 1.3.: Comparison of the integration with the old and the new set-up with a relative humidity of 20% at varying fibre strains.

2. Theoretical background

2.1. Biological material: hair

Hair is a biological material that a lot of mammals have, with specific properties depending on the living environment as well as on the respective location on the body of the animal. Especially for animals living in extreme conditions, different types of fur with different lengths and textures are combined to provide optimised protections.

The hair fibres exhibit a hierarchical organisation at its different scales. A scheme of the internal arrangment is presented in Figure 2.1 and is taken from Alexander Müllner in [14]. First, the fibre's outermost region is the cuticle, composed of four distinct layers, each with its own molecular composition. Scales a few µm long, partially covering each other along both the fibre length and the transversal direction, constitute the surface of the fibre and point all toward the tip of the hair. They form a hydrophobic outermost layer around the hair due to the proteins and the bonds constituting them [15]. As the cuticle is rich in lipids, the SAXS pattern will present a ring at a distance of 4.62 nm which is the typical distance between the lipids in the cuticle. [14]

The next part, toward the core, is the cortex, presenting a regular arrangment of macrofibrils, surrounded by a so-called intermicrofibrillar matrix. The macrofibrils are themselves constituted of microfibrils regularly arranged called intermediate filaments embedded in a microfibrillar matrix [15].
The intermediate filament (written IF in the rest of this thesis), measuring around 7 nm in diameter, exhibits a crystalline arrangement of molecules in both longitudinal and tranverse directions, providing the basis for scattering analysis of its structure. The mean distance between molecular arrangement of the IF along the fibre direction is visible in the SAXS pattern as an arc at about 6.7 nm in real space on the meridian. [4, 14].

The medulla is the inner part of the fibre and the less dense (or even hollow) part of it. Its presence, its size and appearance differ from one species to another, but also from one hair to another. It is clearly visible in the image of the section of the fibre. Figure 2.2 shows hair(s) from human (left) with barely no medula, and from dog (right) which presents a more porous and even hollow region in the middle of the fibre. In the majority of human hairs the medulla is not visible and the hair is dense from the cuticle to the center [14].

The keratin contained within the IFs is the part of interest here, and its feature is visible in the wide-angle range. It is important to note that in hair from mammals the keratin is called α-keratin, having a different chemical composition than for example the keratin in feathers of birds which is called β-keratin.
The α-keratin can have different conformations, without changing anything on its composition and unfortunately the conformations are called α and β. The α- and β-configurations mentioned in the thesis always refer to the two conformations of the α-keratin from mammals.
A sketch presenting how one can imagine the α- and the β-configuration is shown in Figure 2.3.

The structure of both configurations has already shortly been presented in Section 1.2 and a possible representation is given in Figure 2.3. The α-configuration is a right-handed helix with a diameter of 1.2 nm and a pitch of 0.52 nm that contains 3.6 residues per turn. Two of these helices are wound into a two-stranded, left-handed coiled-coil.

The distance between the two simple helices is visible in the WAXS pattern obtained by Kreplak et al. and shown in Figure 1.1 (b), as a bright spot at around 0.98 nm (distance in real space). [4]
The sheets of the β-configuration has a width of 0.2 nm, and is folded with a period of 0.7 nm. During the transition, the residues are stacked along the axis over a distance of 1.2 nm. The exact configuration whether parallel or antiparallel of the β-sheets is not specified and seems to depend on the conditions of the transition [10].

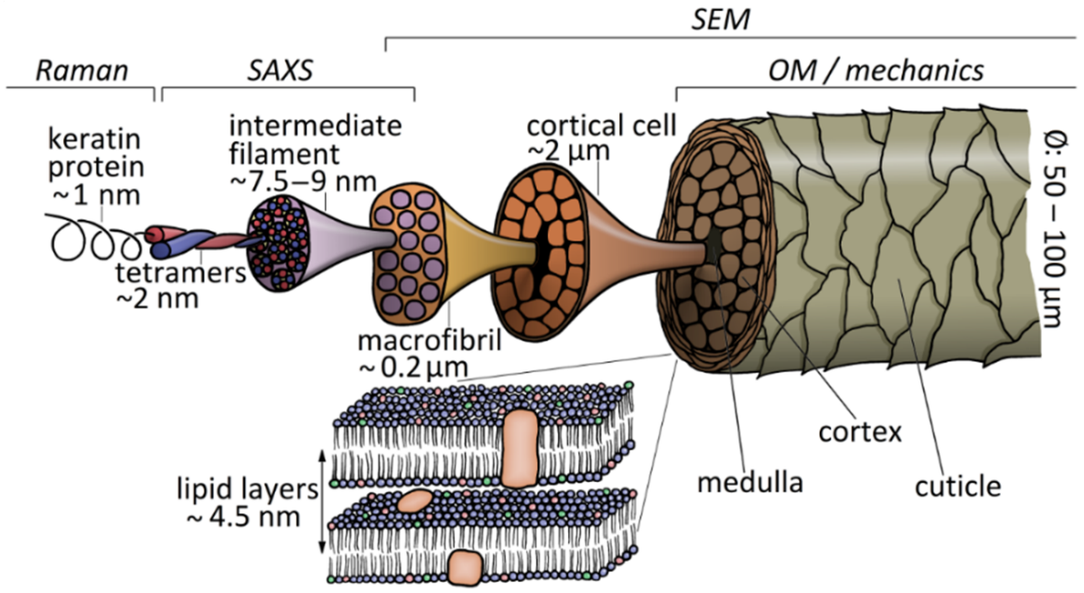

Figure 2.1.: Hierarchical structure of hair under various magnifications. Sketch from Alexander R. M. Müllner et al. [14].

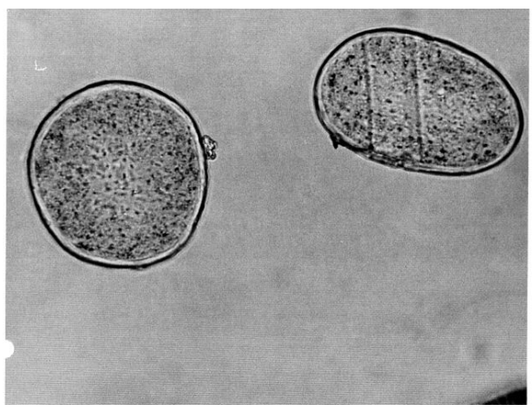

(a) Image with light microscope taken from Robbins and Crawford [12] of human hair in water.

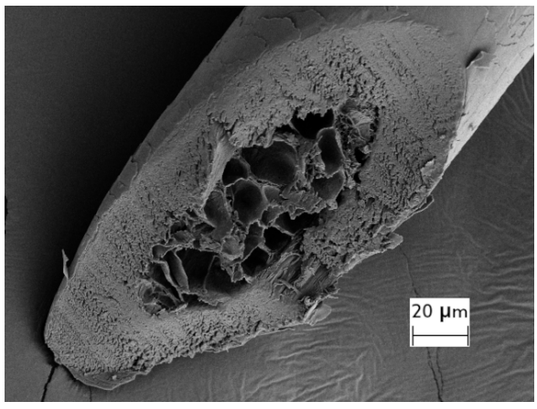

(b) SEM Micrograph of the crossection of a White Swiss Shepherd Dogs hair. Recorded at the Faculty Center for Nanostructure Research, Faculty of Physics, University of Vienna by the Author.

Figure 2.2.: Section view of human hair (left) with light microscope by Robbins and Crawford [12] and dog hair (right), the SEM micrographs showing the difference in the medulla depending on the species.

2.2. X-ray radiation and production

X-rays are electromagnetic waves, with, in the most practical applications, a wavelength ranging from 10×10^{-9} m to 10×10^{-12} m. More specifically, the X-rays used in the SAXS facility in Universtät Wien is originating from the K_α transition of copper atom.

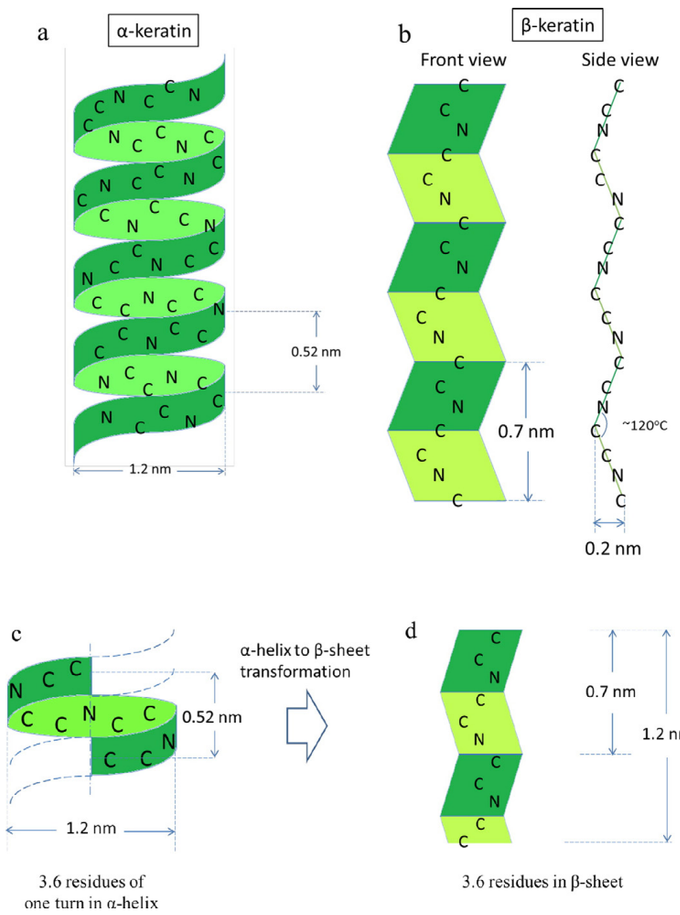

Figure 2.3.: Model of α- and β-configuration, taken from Yang Yu et al. [6]

It has a wavelength equal to the weighted mean of K_{α_1} and K_{α_2}, being respectively 0.1541 nm and 0.1544 nm and corresponding, respectively, to an energy of 8.0478 keV and 8.0279 keV [16]. The X-rays used here have therefore a wavelength of 0.1542 nm and an energy of 8.04 keV.

The spectrum of X-ray radiation produced is composed of two superimposed parts, one smooth and continuous called Bremsstrahlung (breaking radiation) and the other consisting of sharp characteristic rays originating from the energy levels of the electronic shell of the target element [17].
Bremsstrahlung originates directly from the way the radiation is produced. Accelerated electrons are thrown onto the metal target and therefore quickly decelerated by the collision. The fast deceleration of charged particles produces such spectrum, the exact shape of which will depend on the initial acceleration voltage applied to the electron. When the particles are accelerated in the range of a few kilo-electronvolts, the radiation is in the X-ray region [16].
As already mentioned, the sharp peaks are the characteristic X-ray lines of the atoms. When the incident electron, having a certain momentum, hits the electronic shell of the target atom, the energy is partially transferred to an electron from the atom, which will kick it out of it, leaving a vacancy in the shell. For stability purposes, an electron from an outer shell occupies the vacancy left by emitting energy. The emitted energy corresponds to the energy difference between the two electronic shells, which is specific and tabulated for every element, since the linear relation between the wavelength of the X-ray and the Z-number is given by the Moseley's law, with C and σ constants [18]:

$$\sqrt{\mu} = C \times (Z - \sigma) \tag{2.1}$$

The typical spectrum of Molybdenum with 35 kV acceleration for the incident electron, taken from the book «Elements of X-ray diffraction »written by B.D. Cullity [18], is shown in Figure 2.4.

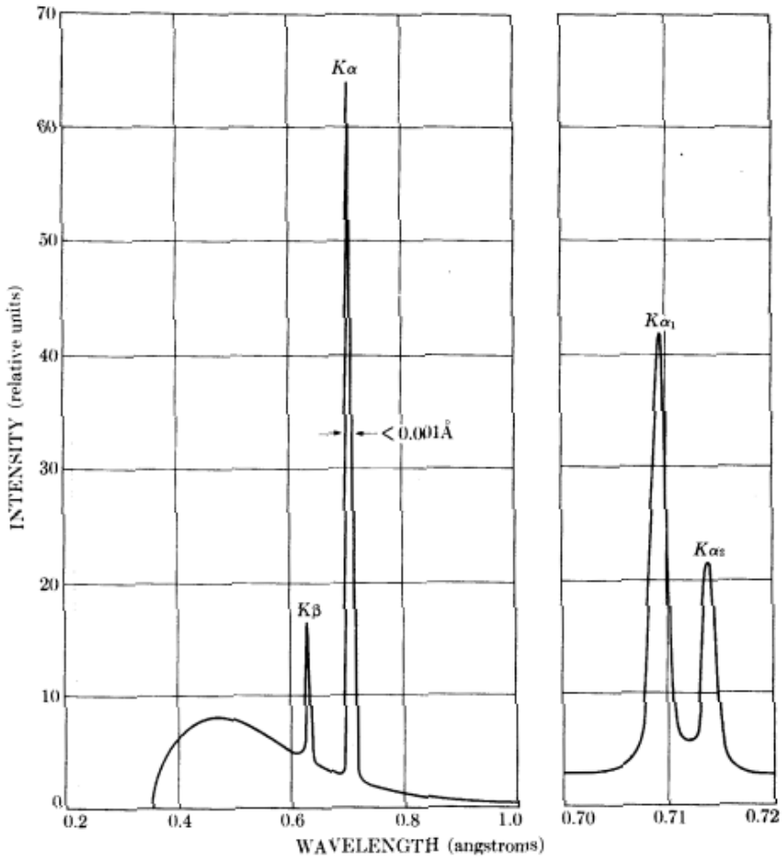

Figure 2.4.: Schematic spectrum of Mo at 35 kV, on the right is the resolved K_α line on an expanded scale [18].

The first source of X-rays that was used in experimental set-ups since the 19th century was gas tubes, also referred to as "cold cathode" tubes to make a clear difference with the X-ray tubes discovered later ("hot cathode") that used a heated filament. Electrons were detached from the cathode by the impact of ions in a low-pressure gas tube. [19]
Gas tubes are now obsolete and no longer in use because of their difficult utilisation.

Filament tubes are the instruments used nowadays and although there are different types, the principle remains the same, with a cathode (generally a tungsten filament) and an anode (generally a block with the desired metal, often copper is used as target). The tungsten filament is heated up and will emit the accelerated electrons towards the water-cooled anode. It is important to keep in mind the necessity to have a small focal point for the electrons on the target to achieve high intensity emitted X-rays.

2.2.1. Different types of filament tubes.

The rotating anode reduces the problem of the corrosion and evaporation of the target over time, which can be an issue for long measurements and lead to a decrease in intensity. They provide indeed much higher intensity radiations than a sealed tube or a microfocus equipment.
This type presents disadvantages in laboratory facilities because of its high cost due to the difficulties involved in their fabrication and installation. These sources also need to be changed often and are more difficult to move.
Another high-intensity source is the liquid metal jet [20], that consists in a liquid metal column as a target. Since it does not involve any solid metals, issues related to melting and the required cooling are not encountered. The disadvantage is that the cost and technical challenges are again higher than for the rotating anode, but they provide higher intensity X-rays.

The X-ray tube used in the SAXS in Vienna is a microfocus tube, which achieves a small focal point thanks to a high negative voltage on the focusing cup around the anode. This is especially useful when small beams are required, the costs are lower and commissioning after installation is quick, as its decommissioning, due to the good stability of the equipment.
Another source, providing high intensity beams and now widely used in the dedicated facilities is synchrotron radiation, originating from particles accelerated to relativistic velocities. The radiation properties are defined by the acceleration specifications and can therefore be monitored.
Synchrotrons sources provide higher intensity beams than any other technics, a stable beam, with low divergence and very short pulses. [16]
However, as they are large scale facilities, an access is in general only possible by writing proposals. This requires a lead time for an experiment of about a year. The possible damages caused by the high intensity of the beam also need to be taken into account, depending on the type of sample and the exposure time needed.

2.3. Principle of scattering

Scattering describes the process that takes place when a wave (electromagnetic or matter waves) interacts with matter, in particular with matter composed of a periodic repetition of units. In the case of a crystal for example, where the atoms and electric charges are regularly arranged in space on a lattice, the atoms act as scattering centers. This occurs when the wavelength of the propagating wave and the spacing between the atoms are of the same order. In the case of structures of the order of an angstrom (1×10^{-10} m), for example crystals or molecules, the energy of the incoming wave should be [17]:

$$\frac{\hbar c}{\lambda} \approx 12 \times 10^3 \,\mathrm{eV} \tag{2.2}$$

which corresponds to the X-ray range.

The diffraction pattern obtained does not reflect distances and geometry in real space but in reciprocal space and the two are connected via Fourier transformation. The pattern, distances and characteristics in real space can then be determined.
The incoming waves, after interacting with matter are deflected in a certain angle, which is directly dependent on the wavelength and the typical spacing of the atoms in the material. This can be described as the emission of vibrations originating from every atom, all interfering with each other, thereby creating an interference pattern. On the scattering pattern, bright spots appear when the scattered rays superimpose through constructive interferences. [19]

2.3.1. Reciprocal space and lattice basis

The reciprocal space is directly related to real space via Fourier transformation, distances and characteristics in a scattering pattern must be analysed under reciprocal space considerations.
First of all, it is important to briefly introduce crystals and their definition in real and reciprocal space, not because they are used as such in this thesis, but because they are essential to the scattering theory briefly introduced in this section.
Crystals are regular arrangements in space of one or more atoms or ions (a basis) regularly placed in space on a lattice. Their geometry can therefore be described by a unit cell, spanned by unit vectors. This unit cell reproduces the complete structure by translation along the unit vectors multiplied by integers.
In the rest of the section the unit vectors in real space are written as $\vec{R}$ and in reciprocal space as $\vec{R}^*$.
The vectors corresponding to the incoming and scattered (outgoing) waves, both in reciprocal space, are respectively $\vec{k}$ and $\vec{k'}$ and are called wave vectors. In the case of

elastic scattering, which is the case in Section 2.3.2, their magnitudes are equal and only their directions change by twice the scattering angle θ. The module is related to the wavelength in real space by:

$$k = \frac{2\pi}{\lambda} \tag{2.3}$$

The so-called scattering vector is here called $\vec{Q}$ and is defined as $\vec{Q} = \vec{k'} - \vec{k}$, the difference between incoming and outgoing wave vectors.
A unit cell in real space having vectors $\vec{a_1}$, $\vec{a_2}$ and $\vec{a_3}$ is transformed into reciprocal space and described by a new set of vectors as following [17]:

$$\vec{a_1^*} = 2\pi \frac{\vec{a_2} \times \vec{a_3}}{\vec{a_1} \cdot (\vec{a_2} \times \vec{a_3})} \tag{2.4}$$

$$\vec{a_2^*} = 2\pi \frac{\vec{a_3} \times \vec{a_1}}{\vec{a_1} \cdot (\vec{a_2} \times \vec{a_3})} \tag{2.5}$$

$$\vec{a_3^*} = 2\pi \frac{\vec{a_1} \times \vec{a_2}}{\vec{a_1} \cdot (\vec{a_2} \times \vec{a_3})} \tag{2.6}$$

After correctly defining the unit vectors for the unit cell of a crystal, any atom position can be written: $\vec{R} = a_1\vec{a_1} + a_2\vec{a_2} + a_3\vec{a_3}$, a_1, a_2 and $a_3 \in \mathbb{N}$.
In reciprocal space, a corresponding position is written:
$\vec{R^*} = h\vec{a_1^*} + k\vec{a_2^*} + l\vec{a_3}$, with $h \propto \frac{1}{a_1}$, $k \propto \frac{1}{a_2}$ and $l \propto \frac{1}{a_3} \in \mathbb{N}$.
The set of indices (h, k, l) are called Miller indices and are used to define crystallographic planes. However, this concept will not be further explained here.

2.3.2. Elastic scattering

One sort of scattering, although ideal and never occurring exactly in practice, is elastic scattering. In this case the incoming and the outgoing waves have the same energy and only their directions change. This means, energy is conserved, but the momentum is changed by the scattering process, i.e. the momentum is transferred from the electron to the photon. At low energies ($< 10\,\mathrm{keV}$) elastic scattering is dominant and the theory below is based on it.
The two main laws to describe the conditions for this process are the Bragg's relation and the Laue's relation. They are equivalent, but describe the phenomenon from two different perspectives.
Bragg's law gives the relationship between the diffraction angle, the wavelength and the typical spacing of the atom arrangement, represented by planes in the crystal separated by a distance d, called interplanar distance. Figure 2.5 shows a scheme of the scattering process. As mentioned above, the path difference must lead to constructive interferences

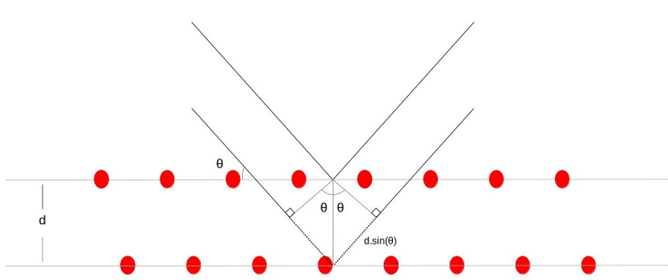

Figure 2.5.: Schematic representation of a wave scattered by a crystal and the geometric construction of the Bragg's relation.

and therefore correspond to a multiple of the wavelength. This directly yields Bragg's relation, where d is the distance between repeated units, θ the Bragg angle equivalent to half of the deflected angle of the rays, λ the wavelength and n an integer [17]:

$$2 \cdot d \cdot sin(\theta) = n \cdot \lambda \tag{2.7}$$

Another way to describe the conditions for constructive interferences is the Laue's formulation. For a wave travelling along the vector $\vec{n}$ and deflected along $\vec{n'}$ by a lattice vector $\vec{R}$, the path difference is again a multiple of the wavelength.

$$\vec{R} \cdot (\vec{n} - \vec{n'}) = m\lambda \tag{2.8}$$

$$\vec{R} \cdot (\vec{k} - \vec{k'}) = 2\pi m \text{ with } k = \frac{2\pi}{\lambda} \tag{2.9}$$

Which can be rewritten as:

$$e^{\vec{R}\cdot(\vec{k}-\vec{k'})} = 1 \tag{2.10}$$

This condition can be rewritten and is fullfilled when $\vec{R}$ and $(\vec{k}-\vec{k'})$ coincide, so when the scattering vector (in reciprocal space) coincides with the lattice vector in real space [17].

2.3.3. Powder diffraction

In light of the previous section, powder diffraction provides a powerful means of characteriing crystals and easily determining their lattice parameters, without the need to align a crystal to a precise orientation. [21]
Because reciprocal lattices are 3-dimensional lattices, one way to access the information about the distances in different crystal planes with a two-dimensional detector is to rotate either the crystal or the detector. This way, the bright spots will be visible on the detector and can be recorded.
If the powder of a crystal is used instead, the sample is constituted of thousands of tiny crystals, oriented in random directions, and therefore presenting different diffracting planes to the incoming beam. It is consequently a practical, easy to handle method with high resolution.
Each grain being a single crystal, it scatters efficiently and only a small amount of powder is needed, which does not lead to excessive absorption of the sample.

The pattern observed is a set of concentric bright rings, centered at the direct beam position with radii corresponding to the typical interplanar distances for all possible orientations.
This powder diffraction technique is typically used for calibration in X-ray scattering measurements, by using powder of pure, well-characterised crystals for which the lattices constants are tabulated. It is also a powerfull method to investigate the influence of doping, temperature or environmental properties of materials.
In the present experiments, we use ceramic powder of aluminum oxide (Al_2O_3) for the calibration, as described in Section 4.2.

2.3.4. Atomic form factor

When a wave, for instance an electromagnetic radiation, meets an atom, the electrons constituting the atom vibrate at the frequency of the incoming wave, becoming coherent sources and interfering. The scattered amplitude depends on the wavelength of the incoming wave, the angle of detection, and the nature of the electronic distribution. This elementary description of the scattering process introduces the role of the entire electronic distribution on the final diffracted pattern. Indeed, the atomic core plays an insignificant role because of its large relative mass, hardly vibrating. [19, 18]
In order to describe quantitatively the behaviour of this scattering process, a factor is introduced called the atomic scattering factor or form factor, which can be defined as the ratio between the scattering amplitude of one single electron and that of the whole atom. This quantity can be interpreted as the efficiency of the scattering depending on the relevant parameters [18].

To describe wide-angle scattering processes, the form factor is the Fourier transform of the electronic density and can be written as the sum of the scattering contributions from individual electrons [17].
The form factor equals Z for the forward-scattering direction, corresponding to a scattering angle $\theta = 0$, and then decreases with increasing θ. Its dependence on $\vec{k} \cdot \vec{r}$ also implies a dependence on $\frac{\sin\theta}{\lambda}$. It decreases as the quantity $\frac{\sin\theta}{\lambda}$ increases.
It also depends then on the wavelength of the radiation, and the form factor decreases as the wavelength shortens. This behaviour can be predicted, since the path differences increases relative to the wavelength, leading to stronger destructive interference effects. [17]

In the case of small-angle scattering, the form factor is described with the overall electronic density of the material and not with the electronic distribution of each atom as described above. The scattering by a single particle is mathematically defined by [22]:

$$f(\vec{q}) = \int_V \Delta\rho(\vec{r}) e^{-i\vec{q}\cdot\vec{r}} \mathrm{d}\vec{r} \tag{2.11}$$

$$\tag{2.12}$$

Where $\Delta\rho(\vec{r})\mathrm{d}\vec{r}$ characterises the electron density difference at position $\vec{r}$.
The form factor is then given by the average of this field aformentioned and here designated as $I(\vec{q})$:

$$I(\vec{q}) = \left\langle |f(\vec{q})|^2 \right\rangle \tag{2.13}$$

$$I(\vec{q}) = 4\pi \int_0^{\mathrm{inf}} \gamma(r) r^2 \frac{\sin qr}{qr} \mathrm{d}r \tag{2.14}$$

$$\tag{2.15}$$

$\gamma(r)$ is here the average of the integrated electronic distribution:

$$\gamma(r) = \left\langle \int_V \Delta\rho(\vec{r_1} \Delta\rho(\vec{r_1} - \vec{r}) \mathrm{d}\vec{r_1}) \right\rangle \tag{2.16}$$

The quantity used to describe the intensity variations depending on the scattering angle is preferably the structure factor, presented in the following Section 2.3.5, describing the electronic density of the atoms spatially placed on the lattice.

2.3.5. Structure factor

After introducing the form factor which gives information on the scattering by a single atom depending on the wave number k and the electronic structure of the atom, the crystal structure itself of the investigated material must be considered. This is achieved through the geometrical structure factor which describes the scattering by the unit cell of a crystal.
Similary to the form factor, it establishes the correspondence between real space and reciprocal space and therefore contains a Fourier transformation that expresses the intensity of the scattered rays by the atoms or ions constituting the basis of the primitive cell.
It is calculated using the form factor (or form factors when the structure contains several elements) and the unit vectors $\vec{R}$ and $\vec{R^*}$ [17]:

$$S_k = \sum_{j=1}^{n} e^{i\vec{R^*}\cdot\vec{R}} \tag{2.17}$$

By re-expressing the product in the exponential according to the type of structure under consideration, one obtains the conditions under which constructive or destructive

interferences, i.e. bright and dark reflections, appear in the scattering pattern.
As an example, a body-centered lattice with lattice constant a and lattice vector $\vec{R}$ has two atoms in the unit cell, which are defined by the vectors $\vec{a_1} = 0$ and $\vec{a_2} = \frac{a}{2}(\hat{x}+\hat{y}+\hat{z})$, and its reciprocal lattice is given by $\vec{R^*} = \frac{2\pi}{a}(h\hat{x} + k\hat{y} + l\hat{z})$. The conditions for bright reflections is then given by [17]:

$$\begin{aligned} S_k &= 1 + e^{i\pi(h+k+l)} \\ &\begin{cases} = 2 & \text{when } h+k+l \text{ is even} \\ = 0 & \text{when } h+k+l \text{ is odd} \end{cases} \end{aligned} \tag{2.18}$$

2.4. Mechanical behaviour

The term mechanical behaviour of a material refers to the way in which the material responds to applied stress and how it deforms and changes, which is described by the strain.
The stress acting on a material is defined as the load applied in a given direction over a surface. On an infinitesimal area ∂A, the stress is defined as:

$$\sigma = \frac{\partial F}{\partial A} \text{ for } \partial A \to 0. \tag{2.19}$$

There are different types of stress, in all cases it is a force applied over an area, defined mathematically by a tensor containing information about the plane and the direction along which the load is applied. A stress applied perpendicular to the plane is a normal stress (which can be tensile or compressive), and a stress parallel to a vector contained in the plane is called shear stress [23].

The tensor σ has diagonal components corresponding to the normal stresses, written σ_{xx}, σ_{yy} and σ_{zz}, corresponding to the different planes in Cartesian coordinates. The tensor itself is symmetric because, if a stress is applied but the object remains motionless, the opposing forces must be equivalent and pointing in opposite directions only. This leads to $\sigma_{xy} = \sigma_{yx}$, $\sigma_{xz} = \sigma_{zx}$ and $\sigma_{yz} = \sigma_{zy}$.
When stress is applied to a body, the strain ϵ refers to the deformation the material undergoes and is defined as the relative variation between initial and final length. [23]

2.4.1. Stress-strain curve

Different materials exhibit similar behaviour under stress which can be observed with the plot of strain against stress. Similar regions are observed for a wide variety of materials. These regions are delimited by critical stress values and include, at low strain, the Hookean region, characterised by a linear relationship between stress and strain. This law is based on the assumption that the material is isotropic, homogeneous, elastic and infinitely divisible into infinitesimal units. These conditions are of course ideal cases and are not fullfilled in most situations, but such linear behaviour is nevertheless observed and holds for small deformations up to a critical load. In this elastic region, the distances between atoms and molecules change, but the initial length is fully or almost fully recovered when the stress is released.
Physical quantities such as Young's modulus E are defined as the proportionality factor in the Hooke's law and are specified for a given material under certain environmental conditions [24]:

$$\epsilon = \frac{\sigma}{E} \text{ in the 1-dimensional case.} \tag{2.20}$$

$$\epsilon_{ij} = S_{ijkl}\sigma_{kl} \text{ or} \tag{2.21}$$

$$\sigma_{ij} = C_{ijkl}\epsilon_{kl} \text{ in the 3-dimensional case.} \tag{2.22}$$

The tensors S_{ijkl} and C_{ijkl} are respectively the compliance and stiffness tensors (the letters used are from old french "souplesse" and "complaisance" respectively).

When the load is increased further and exceeds a certain load, the material enters the plastic region, in which atoms and molecules undergo permanent changes in their structures that are generally not reversible. In the case of (partially) crystallised materials, this permanent deformation occurs through the slippage of atomic planes along adjacent planes. If an even higher load is applied, the material eventually breaks, meaning that atomic bonds are destroyed. [24]

The critical stress values for a material depends on many different parameters both from the material properties and the nature of the applied stress, such as the elements constituting the material and its structure. External parameters, including the rate of loading, atmospheric conditions and temperature variations, as well as prior stress history, also influence the strain behaviour of the material and its repeatability. [24]
As an example, it is worth noticing the so-called "fatigue" effect, which refers to the failure of the stressed body after successive applications of deformation. Indeed, repeatedly applying a stress lower than fracture stress can nevertheless lead to fracture of the material. [23]
In some materials (for example hair), after plastic deformation and subsequent relaxation, the strain does not return to its initial value. The material therefore exhibits a residual strain, and a second extension produces a stress-strain curve similar to that of the first extension, but with hysteresis. [6]

2.4.2. Loading process

Stress can be applied to a body in different ways, leading to different mechanical responses and each method is preferentially used depending on the properties being investigated.
Applying a gradual load, such that the body remains in equilibrium until failure, allows us to neglect fatigue effect and enables the evaluation of properties such as Young's modulus, the elastic limit, the yield point and the strength. Such a load is not maintained, and the effects of time on the body are not considered. [24]
By contrast, long-term static loading refers to a process in which a high load is applied and maintained during testing. This approach is used to investigate material behaviour under constant stress and to determine, for example, the permanent strength. [24]

Another approach is the cyclic loading, which refers to a repeated application of stress and is directly related to the fatigue effect mentioned above.

3. Experimental set-up

3.1. Samples

The samples are human hairs donated by Martin Haßler, cut and glued with the UHU Sekundenkleber Blitzschnell Minis Gel on a paper frame. Different glues were tested and compared regarding their behaviour under tension. The tests and results are described in details in the Section 4.1.
The samples were stored for about one day in a 100% humidity environment and then stored in ambient conditions until measurement. The reasons for this humid storage condition are a strengthening of the superglue with humidity, detailed in 4.1, and the humidity condition during measurement varying from 20% relative humidity to 80%. This way, every sample experiences the highest humidity condition.
Two types of frames have been used, one having a clamping length of 5 mm on both sides and a length of 10 mm. 30 hairs were used here, as it was the number used in the last master's thesis by Johannes Liebhart [13].

For the second one, the clamping length has been increased to 10 mm to strenghten the adhesion during extension. For this type, only 20 hairs are glued together. The two types of samples and frames are shown in Figure 3.1.
The lower number of hairs and the increased length have two advantages: the preparing of the sample is easier due to the limited number of hairs to mount, and it also allows to have a more flat bundle and therefore to avoid sliding of the hairs and to obtain a more uniform strain of the fibres thanks to the higher failure strenght of the glue and the clamps.

The effect on the strain is visible in Figure 3.2 with the strain curve for the two types of samples. The test with the first version with 5 mm clamping length presents a significant drop of the force far before the end of the measurement, during the extension between 4 mm and 5 mm as visible in Figure 3.2a. The curves between two extensions keep the same course which is a linear region followed by the plastic deformation during the extension. It is followed by a relaxation phase during which the strain decreases linearly down to a residual force, slightly higher than that of the previous step. This same behaviour with only a drop on the load indicates that the fibres are still partially held and extended but there is very likely some glue failure and a subsequent stick-slip of the hairs leading to the observed decreasing maximum force.
Figure 3.2b shows the results of a larger glued area on the sample frame and its effect on the load during strain application. The envelope does not exhibit any drop anymore and the load continues increasing until fibre breakage.

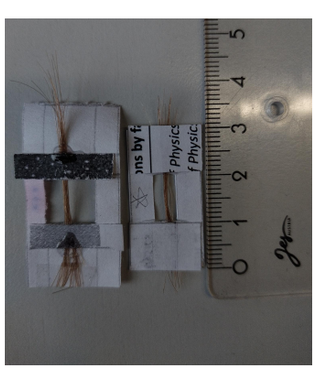

Figure 3.1.: Hairs (10 mm length) glued on the paper frame with clamping length of 5 mm and 30 hairs (left) and clamping length of 10 mm and 20 hairs (right).

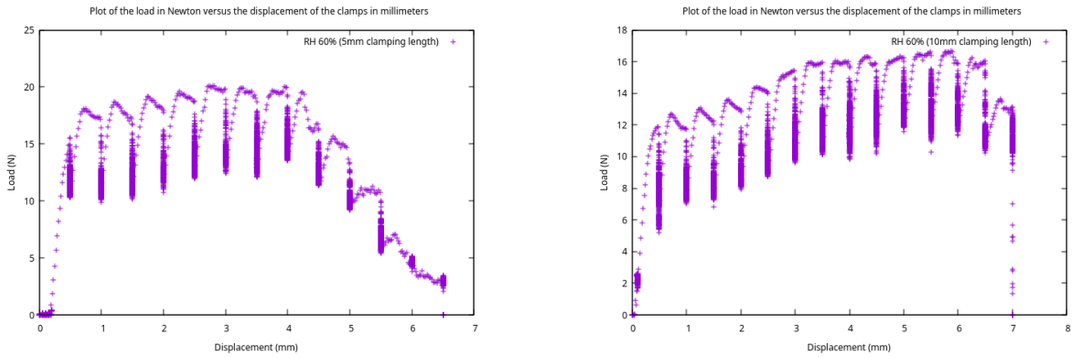

(a) Test on the sample with 5 mm clamping length.

(b) Test on the sample with 10 mm clamping length.

Figure 3.2.: Load versus displacement for RH 60% for the sample with 5 mm gluing length (left) and 10 mm gluing length (right).

3.2. In-situ measurement facility

3.2.1. Chamber

The samples are placed in a closed chamber (Figure 3.3) in which parameters such as humidity or temperature can be also controlled during in-situ measurement. The chamber is made of aluminium with an entrance window closed by an aluminium foil, and an exit window closed with a polymeric foil. Such thin foils are X-ray transparent with a transmission significantly higher than 50%, but keep the required environmental conditions inside the chamber.

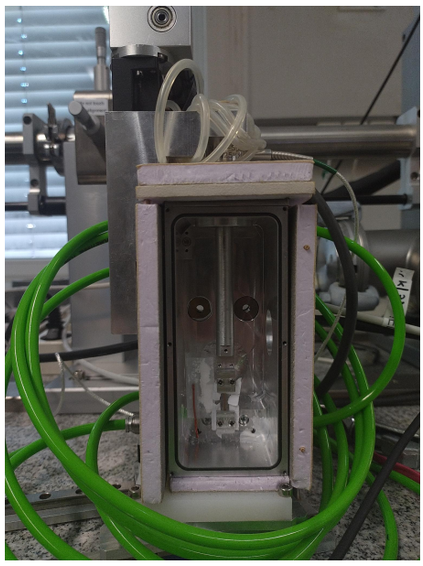

Figure 3.3.: Open chamber with the sample (right) and the calibrant (left). Both sides of the frame have been already cut, the sample is ready for the experiment.

3.2.2. Tensile-test machine

The sample is fixed between two aluminium blocks and screwed to the support.
For the tensile test machine, a 1kN load cell is connected to a Doli EDCi 22 device (Figure 3.4) for both manual and computer control [25]. In the chamber, a motor moves the upper clamp up and down and the distance as well as the force between the clamps is measured and recorded.
The speed as well as the extension can be controlled with the in-house software written by Stephan Puchegger.

Figure 3.4.: Picture of the EDCi 22 controller for performing tensile test experiments.

3.2.3. Humidity control

The humidity is controlled with a ProUmid MHG32 Humidity generator [26] shown in Figure 3.5a. It allows choosing a relative humidity which will be set and maintained by a closed loop control and its humidity sensor directly placed in the chamber. Two nitrogen flows (one dry and one wet) are mixed together in the mixing unit in the correct proportion to achieve the needed relative humidity. The temperature of the bath is adjusted to compensate for evaporation enthalpy. The working principle is shown in Figure 3.5b

(a)

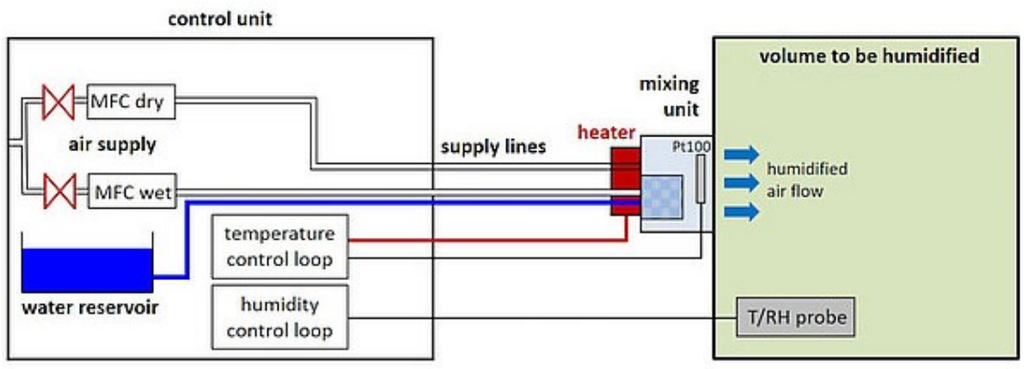

(b)

Figure 3.5.: ProUmid MHG32 Humidity generator and humidity control circuit.
(a) Humidity generator with deionised water container and controls for humidity and bath temperature.
(b) Block diagram presenting the working principle of the ProUmid MHG32. The volume to be humidified being the chamber and the air supply a N_2 bottle, taken from the constructor's webpage [26].

3.2.4. SAXS equipment

The SAXS equipment is shown in short configuration (short sample-to-detector distance) in Figure 3.6. The distance allows scattering measurements in the q-range from about $q = 0.3$ to $10\,\mathrm{nm}^{-1}$. The equipment consists of a copper X-ray source producing the K_α radiation of copper, with a power of $1\,\mathrm{mA} \times 50\,\mathrm{kV} = 50\,\mathrm{W}$.
A Montel optic collimates the beam which will then be also filtered and refined. The two pinholes before the chamber define the beam and suppress parasitic scattering. The beam arriving on the sample is about half a millimeter wide. For this experiment, the tube from the X-ray source to the chamber is in vaccuum and the chamber itself is under ambient pressure. The detector used for the measurement (described in details in Section 3.2.5) is placed inside the SAXS chamber on a platform at about 8 cm from the sample. The beam stop used is fully opaque, unlike the beam stop used for the Vantec detector, so no information on the transmission of the sample can be collected with it.

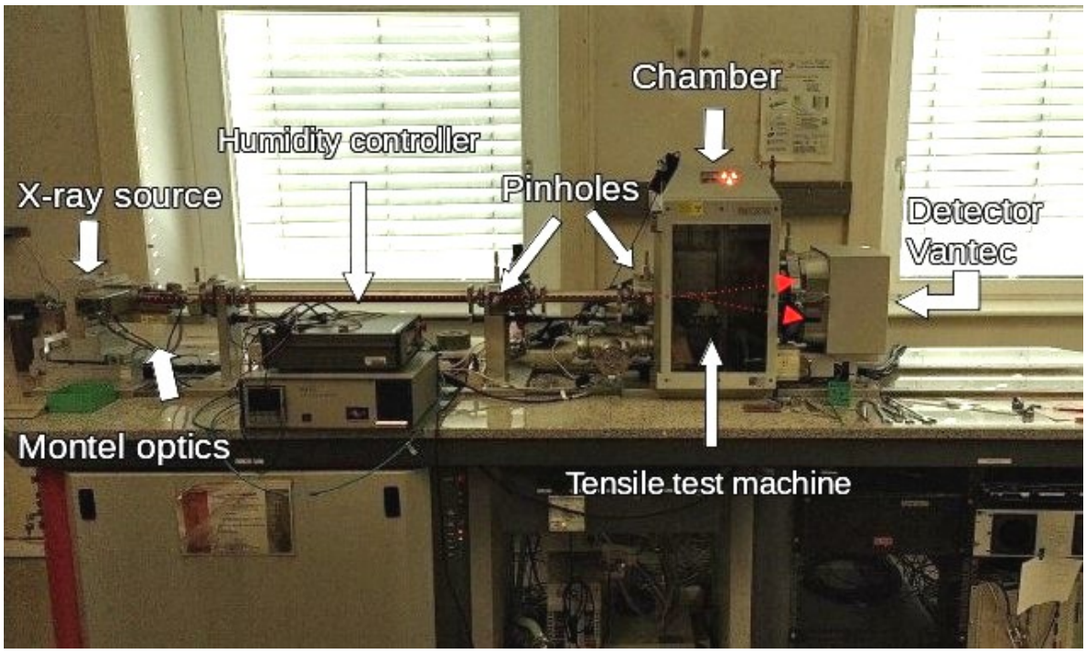

Figure 3.6.: SAXS equipment in short configuration. The X-ray path, the detectors and controller are described on the figure.

3.2.5. Detector Dectris Eiger2 R 500k

The detector used for the data analysis and shown in Figure 3.7 is the Eiger2 R 500k provided by Dectris. It is a hybrid photon counting detector with silicon sensors detecting X-rays having an energy between 3.5 to 40 keV. It is constituted of 526×336 pixels, each of them of a size of $75\,\mu\mathrm{m} \times 75\,\mu\mathrm{m}$, offering an active area of $77.1\,\mathrm{mm} \times 38.4\,\mathrm{mm}$ [27]. Thanks to several corrections and specifications, it offers high quality images and are specifically suitable for scattering analysis with quite low intensity signals.
The detection is made by the pixels independently, allowing a spatial resolution described by a one-pixel point spread function, thus one photon is detected only by one pixel and not more.
It applies a count rate correction, consisting of an instant retriggering unit overcoming pile-up problems and additionally a linearity correction. Both allow to convert the detected number of photons into the number that would be detected by an ideal detector. Additionally, flatfield correction for different X-ray energies, and a mask for the defect pixels (saturated, dead, etc) are available. [27]

Figure 3.7.: Front side of the Eiger2 R 500k detector.

3.3. Measurement time and procedure

The experiment has been conducted at four different relative humidities: 20%, 40%, 60% and 80%. For the series at RH20%, 40% and 60%, measurement was done from 0% until a significant load drop is observed (breakage of the fibres), with steps of 5% strain. For the RH 80%, the images were taken at every 10% of extension also with ten frames per image.

To obtain a good statistics the total measurement time was set to 1800 s (distributed as: 10×180 s).
In the experiment, we decided to measure 10 frames of 180 s and to sum their intensities up. In this way, cosmic rays, appearing as bright trails on the single short-time frames, are removed.
Moreover, with this procedure, it is possible to keep a measurement valid and exploitable even in case of acquisition problem on the detector. Indeed the detector would sometimes give out a saturated image. Figure 3.8 compares a good frame (right) and a saturated one (left) for 60% relative humidity and 10% extension.

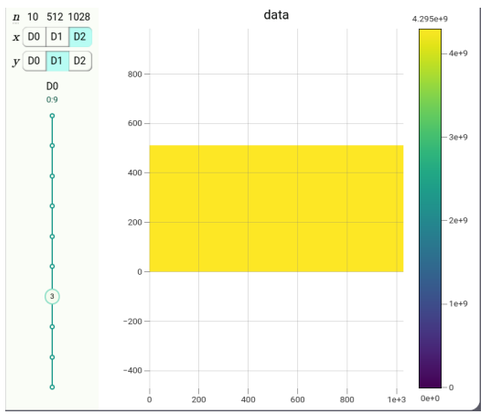

(a) Frame with saturated intensity measured for 180 s.

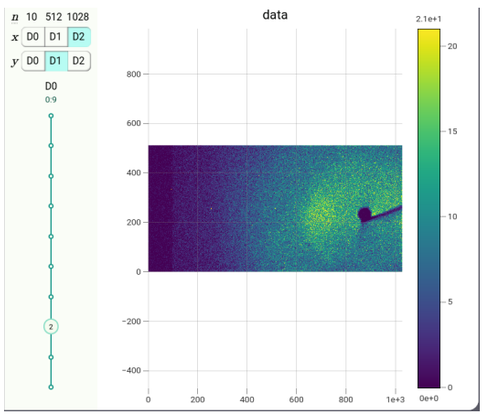

(b) Frame with usable data measured for 180 s.

Figure 3.8.: Two frames for measurement under the conditions 60% relative humidity and 10% extension. The right one shows a clear pattern while the left one should be ignored.

The measurement time is a key point and needs to be be chosen wisely, even more with samples with quite low scattering intensity. The choice for a 1800 s long measurement is a compromise between parameters requiring long measurement and other considerations that are affected by too long ones:
Here, it should be long enough to get good statistics and sufficient intensity to evaluate. This is limited by the scattering volume and the fraction of crystalline material in the sample but also to the equipment and the X-ray beam intensity.

On the other hand, the samples are subject to strain and mechanical deformations, in which relaxation time plays an important role. With this duration, the load drop is considerably smaller than the maximum load, and is chosen to be a good compromise. The load curve for each experiment was already presented in Figure 3.2b.

4. Data evaluation procedure

4.1. Choice of the glue

In order to mount them into the tensile test machine, the hair bundles are glued onto a paper frame. To reach the desired extension of the fibres (higher than 60% of the intial length) without ripping out of the frame, the glue should be able to keep adhesion in both stress and humidity during measurement.
Two different tests are conducted. The first one with a Molybdenum wire of 15 mm length and 0.6 mm diameter. The wires have been extended by 3 mm, for each glue and at 15% and 100% humidity. For the hairs, a bundle of 30 hairs of 15 mm length are extended by about 9 mm. Both are glued on a similar frame, with a gluing and clamping length of 5 mm. In order to reach an equilibrium, each sample has been placed in the chamber at the right relative humidity and zero load for 20 minutes.
Figure 4.1a presents the results and shows a neat difference between the Epoxy and the super glues (from UHU and Loctite). The load with the Epoxy stays relatively low and drops earlier than with the super glue-like glues. Similarly with the hairs presented in Figure 4.1b, the Epoxy does not seem to have a sufficiently good holding capacity.
The comparison of the super glue Loctite with the super glue UHU gives similar results under same humidity conditions. In humid conditions, the plastic deformation regime is reached later (see Figure 4.1a). This can be explained by the compositon of the super glue: it is based on cyanoacrylates that need humidity as an initiator to form polymeric chains.
Based on these measurements, we decided to use the UHU superglue in gel for the further experiments, the same as already used in the previous thesis. The gel version is used to limit penetration of the glue into the hair fibres and possible changes in the composition of the hair, or leakage out of the frame what would make the hair more rigid along its whole length.

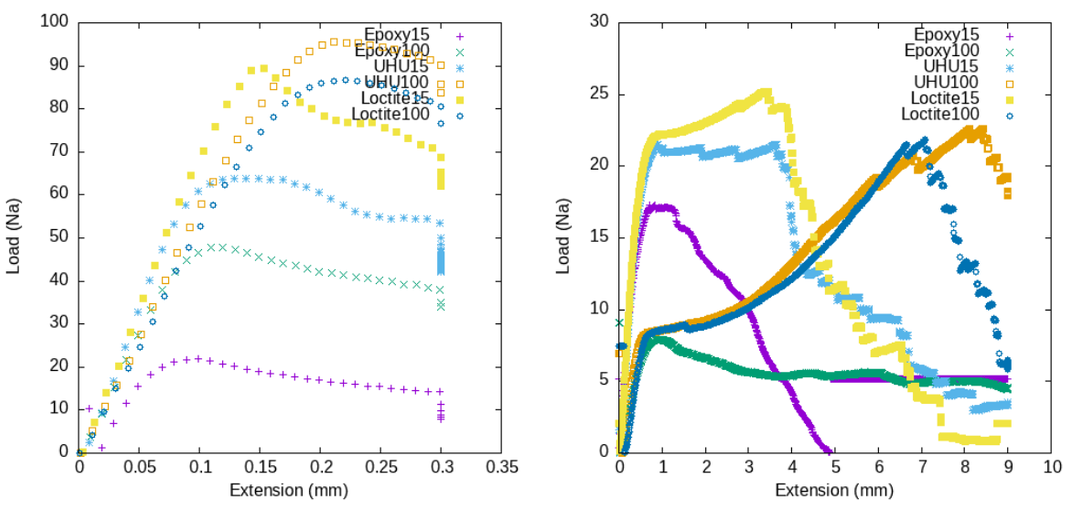

(a) Test with Molybdenum wire.

(b) Test with the hairs.

Figure 4.1.: Glue testing: plots of the load against extension with epoxy glue (by UHU) and super glues (by UHU and Loctite). The numbers 15 and 100 in the text correspond to the tests at 15% and 100% humidity.

4.2. Calibration

In order to determine with precision the distance between the sample and the detector as well as its tilting angle, an image of the scattering pattern of a calibrant is taken before each series. In this measurement, a ceramic powder (Al_2O_3) was used as calibrant, which has its first three peaks at $2\theta = 25.349°$, $2\theta = 34.834°$ and $2\theta = 37.432°$, corresponding respectively to maxima in q at $1.79\,\text{Å}^{-1}$, $2.44\,\text{Å}^{-1}$ and $2.62\,\text{Å}^{-1}$. [28]
We have Cu $K_{\alpha 1}$ with $\lambda_{\alpha 1} = 1.5406\,\text{Å}$ and Cu $K_{\alpha 2}$ with $\lambda_{\alpha 1} = 1.5444\,\text{Å}$, with an intensity weight of $\lambda_\alpha = 1.5418\,\text{Å}$. The relationship between the wavelength and the scattering angle is $q = \frac{4\pi}{\lambda} \cdot \sin(\theta)$ from geometrical considerations, when 2θ is the angle between the incident and the deflected beam. [17] The powder consists of tiny crystals with random orientations and the scattering pattern presents therefore concentric circles at the crystal reflections. The calibrant diffraction pattern is shown in Figure 4.2.
A bit of powder is glued in tape and placed next to the sample. The assembly was already shown in Figure 3.3.

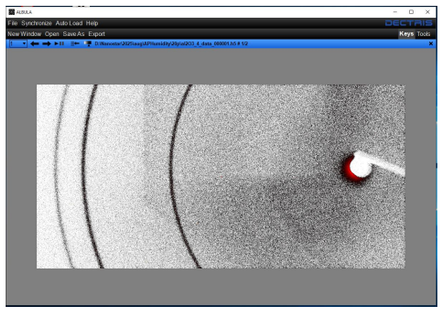

Figure 4.2.: Scattering pattern of the Al_2O_3 at 20% humidity.

4.3. Integration procedure

The Dectris detector provides a 2-D scattering pattern as shown in Figure 1.2c.
The calibration and the integration of the pattern were done using the software DAWN [29]. It allows to define the integration process, which will be used for every series.
First of all the peaks in the calibration pictures are found with the "Powder Calibration" tool, and the information of the geometry of the detector is saved. The pattern are then calibrated, the threshold mask is used, keeping only the intensities between 0 and 100. This was used to eliminate the defect pixels of the detector, showing a much higher intensity. The cosmic rays possibly remaining are also eliminated by this procedure.
The solid angle correction implemented in the software is then applied. For the integration, the azimuthal integration tool is used, between the angles 150° and 210°. The radial range spans between $q = 0\,\text{Å}$ (matching the position of the direct beam) and the edge of the image. It gives the plot of the intensity versus q(Å).

4.4. Background subtraction

4.4.1. Measured background and transmission

The images obtained include different types of backgrounds that need to be subtracted in order to analyse only the relevant parts of the pattern, i.e. the positions and shapes of the X-ray peaks. Our interest focuses on changes of these parameters.
The first background which is subtracted from the images is the one measured after each measurement at the same relative humidity but without sample. It includes the air scattering, the possible reflections due to the different objects along the beam path, and also the background noise from the detector. It is recorded at the same position as the sample measurement to have the same position of the possible shadows of the objects in the chamber. Since the clamps move during the measurement, the background

is recorded only once. The effect of the position of the clamps on the background is discussed in Section 4.5.
For subtraction, the background image is integrated following the same procedure than for the other images, and its intensity is subtracted from the intensity of the data files at each q, with the relation:

$$I_{sub}(q) = I_{total}(q) - I_{measured_{BG}}(q) \times 0.9 \tag{4.1}$$

The factor 0.9 corresponds to an estimated transmission of the sample, which is of course an approximation, but can be determined to be of this order by the intensity recorded during 1 second during the search of the sample.

The sample is located in the intensity record in Figure 4.3 between 34.5 mm and 35 mm for the position of the x-motor and 68 mm and 72 mm for the position of the y-motor in the sample chamber. The average intensity of the sample is 6763 counts/second and the average intensity of the background is 7544 counts/second. That makes an estimated transmission of $t = \frac{6763}{7544} \times 100 = 89.7\%$. Figure 4.3 is a 2-D screenshot of the

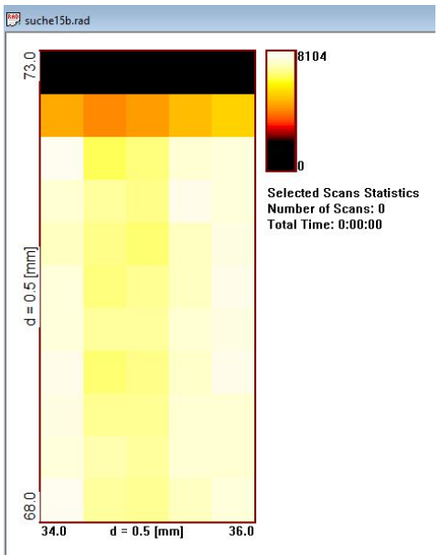

Figure 4.3.: Screenshot of the image recorded to search for the sample at RH 80% with 1 second acquisition. The sample is visible in the vertical direction as a slightly lower intensity due to the absorption of the X-ray intensity by the hair with a transmission of about 0.9.

intensities, which allows for finding the sample and estimating the transmission.

In Figure 4.4, one sees the original data (in dark red), the background intensity (in grey) and the subtracted intensity (in light red), exemplarily for one measurement at 20% and at 80% relative humidity at zero extension.

4.4.2. Normalisation

In order to get comparable intensities, the data intensities should be normalised in a region for which no specific structure of the hair are involved but only dependent on the scattering volume that is the amorphous phases. For this data set the region chosen is the high-q region at about 2.5 Å but just before the drop in intensity visible at high q which is globally lower intensity is presumably due to some shadowing of the chamber. This high-q region is visible on Figure 4.4. The intensity of the few last points of the plateau (about 20 points, the rightmost being the last before significant intensity drop) has been averaged and the normalisation point is chosen as:

$$\begin{aligned} q_{\text{averaged}} &= \frac{q_{\max} - q_{\min}}{\text{number of points}} \\ I_{\text{averaged}} &= \frac{\sum_{\text{last few points}}(I(q))}{\text{number of points}} \end{aligned} \tag{4.2}$$

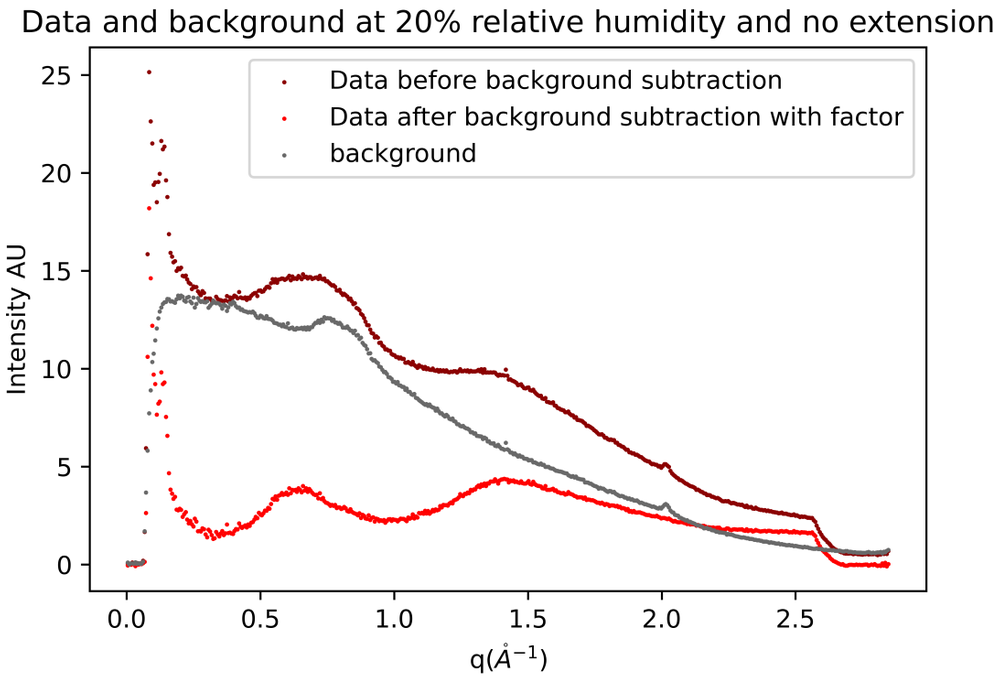

(a) Relative humidity 20%.

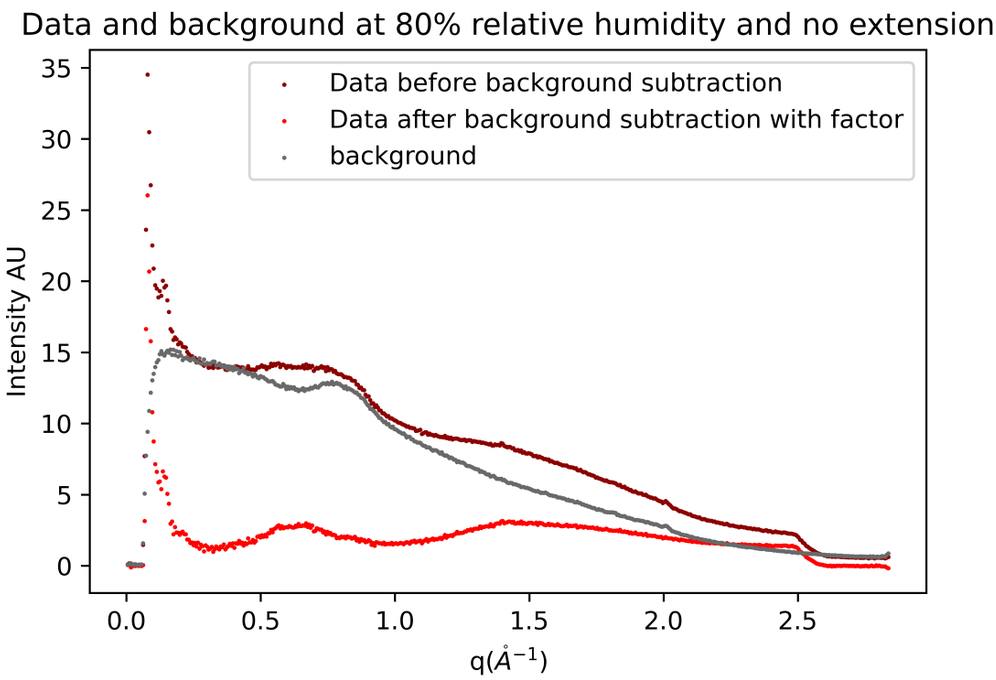

(b) Relative humidity 80%.

Figure 4.4.: Plot of the intensity against q of the data before and after background subtraction, (a) 20% relative humidity, (b) 80% relative humidity.

The normalised intensity is calculated as:

$$I_{\text{norm}}(q) = \frac{I_{\text{sub}}(q)}{I_{\text{averaged}}} \tag{4.3}$$

.

4.4.3. Sample background

The last step before analysis is to remove the amorphous background from the sample. It is constructed as a straight line $f(x) = a \cdot x + b$ (Figure 4.5) which will be subtracted

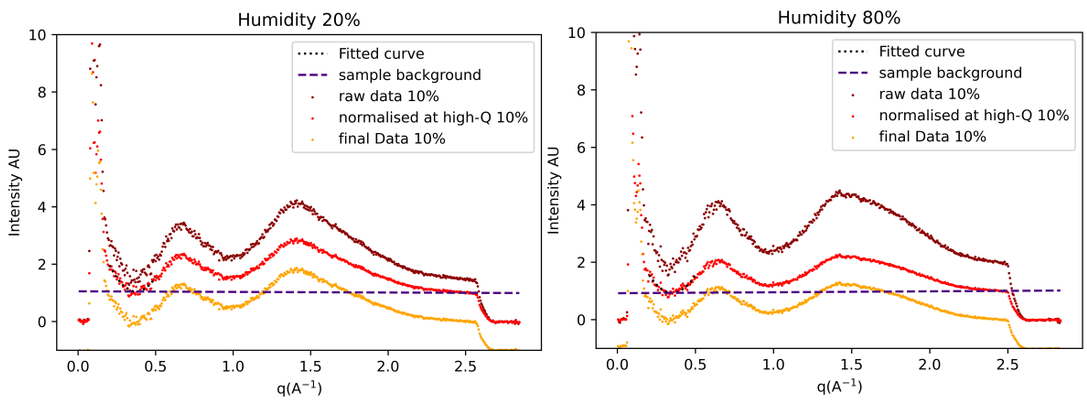

(a) RH 20%. (b) RH 80%.

Figure 4.5.: Plot at the different steps of background subtraction: raw data (dark red), after subtraction of the chamber background (red) and after subtraction of the sample background (orange). The fit with parabola to define the minimum of the region is in black dashed line and the linear function is shown in blue.

from each point. This is necessary because of the presence of amorphous parts in the samples which affect the broadening of the peaks and the general scattering intensity. By this, all peaks from the ordered structure start at the same intensity.

This background will be the linear function spanned by two points: the point used for normalisation at high q, and the minimum of the parabola between the small- and wide-angle region in the valley before the first peak we are interested in ($q \approx 0.4\text{Å}^{-1}$). To do so, a simple parabola is fitted around the minimum, and the point $(q_{min}, I(q_{min}))$ is used. The straight line is defined as the interpolated linear function $f(q)$ between $A = (q_{min}, I(q_{min}))$ and $B = (q_{averaged}, I_{averaged}))$.

$$I_{final}(q) = I_{norm}(q) - f(q) \tag{4.4}$$

The data obtained after this process and their analysis are presented in Section 5.

4.5. Background at different positions

For each series, the background is recorded with the clamps of the tensile test machine at the last position of the measurement, meaning the largest distance they had during measurement. To make sure the position of the clamps does not influence significantly the background, it has been recorded once at different distances.
Figure 4.6 shows the different backgrounds, measured at 20% humidity, for a distance of 10 mm, 13 mm and 16.5 mm. A gradual shift of the intensity to higher values is observed when the distance between the clamps increases. The peak positions do not seem to change.
The change in the background at different clamp positions is small in comparison to the sample intensities, of about maximal 4%, with a maximum intensity shift between the first and the last of 0.5 (in arbitrary units, a.u.), while the first peak is at an intensity of about 12 a u . A small influence on the evaluated peak heights and positions could not be fully avoided, but is expected to be rather small.

4.6. Fitting procedure

The fitting has been done with a programm written by Martin Haßler with which it is possible to fit several peaks at once and to fix some parameters in order to have a several steps fitting procedure.
For the data analysis, the functions chosen should be as simple as possible and therefore having analytical formula with a limited number of parameters. The characteristics of

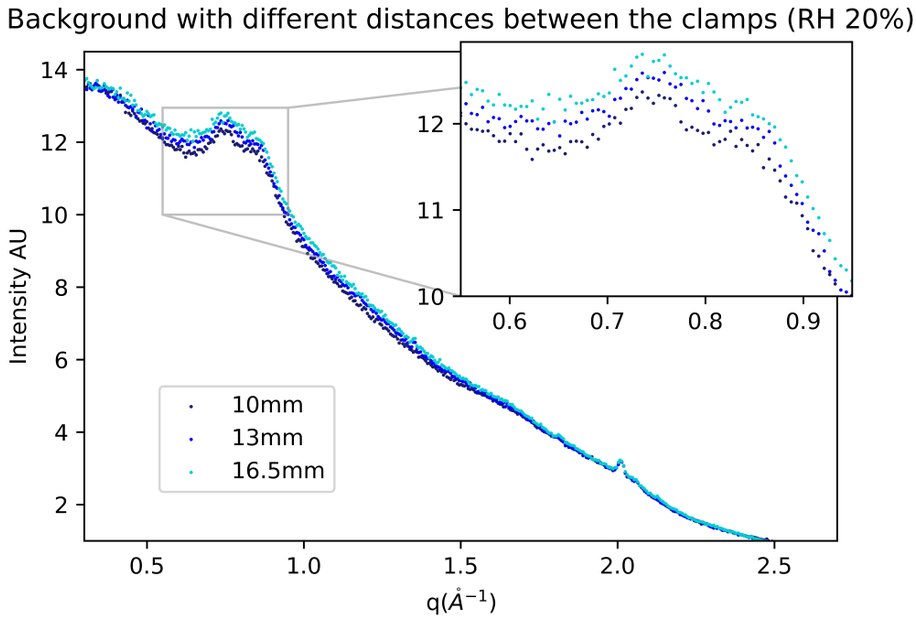

Figure 4.6.: Plot of three backgrounds with clamps at distance: 10 mm (dark blue), 13 mm (blue) and 16.5 mm (light blue).

the peaks we are interested in are their positions (mode), their intensities, their mean positions and variances.

Three peaks are to be fitted: the first one at around 0.70 $Å^{-1}$ corresponding to 9.0 Å in real space, the second at around 1.4 $Å^{-1}$ corresponding to 4.5 Å in real space and the last at around 1.7 $Å^{-1}$ so 3.7 Å, hardly visible because it is close to the second peak and with a lower intensity. It is nevertheless possible to fit it.

For the first step of integration the function used is a skew Gaussian for the first peak summed with a skew Lorentzian for the second and the last (fitted together in the first step). This allows a more stable fit than by fitting at once the three peaks separately. From this first fit, the data obtained for the first peak as a skew Gaussian are kept as final parameters.

For the second step the parameters of the first peak are kept fixed and only the last two peaks are fitted, the second with a Lorentzian distribution and the third with a Gaussian distribution.

Figure 4.7 shows a typical example for the experimental data, the fits and the residuals. The top one is the first step with the skew Gaussian for the first peak and the skew Lorentzian for the two last peaks. The bottom figure is the final fit and again the relative residues. Important to note is that the graph has been adapted for the needs of these data set, and therefore the legend does not always label the peaks correctly. In the case of the first step, whose result is presented in Figure 4.7a, "PeakPos/Mode" refers to the position of the maximum of the function, and "Mean" is the mean position, different than the peak position since the function is not symetric. In the case of the second step, shown in Figure 4.7b, "PeakPos/Mode" is the peak position of the second peak, fitted with the Lorentz distribution and "Mean" refers to the peak position of the third peak, fitted by a Gaussian distribution.

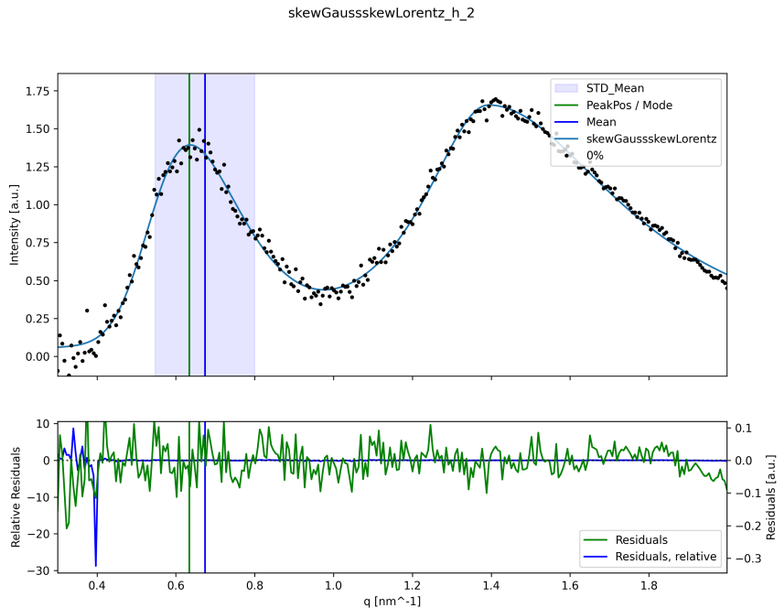

(a) Fit of the first peak with a skew Gaussian and the second and third together with a skew Lorentzian.

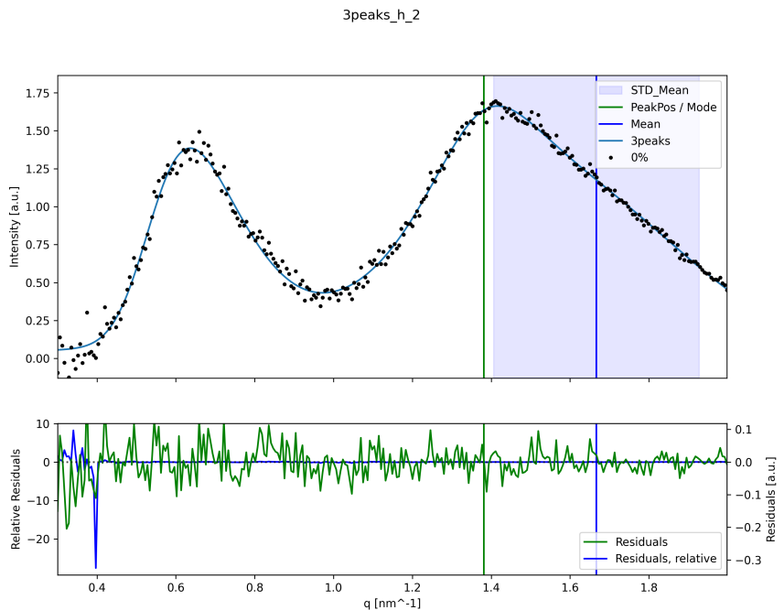

(b) Fit of the second peak with a Lorentzian and the third with a Gaussian fit. The first peak is fitted from the first step of the procedure with skew Gaussian.

Figure 4.7.: Results of the fit of the experimental data for the two step steps of the fitting procedure. The data are for the 20% relative humidity and 0% extension.

5. Results

After background subtraction, the integrated data are presented for each relative humidity in waterfall plots, showing all the extensions from 0% up to fracture. As specified in Section 3.3, the three series at 20%, 40% and 60% are recorded at every 5% extension of the initial length, whereas the series at 80% is recorded every 10%.
From the literature [4] for which the results are presented in Figure 1.1, each of the three peaks could be assigned to a specific arrangement of the keratin molecules in the hair samples. As stated above, only the equatorial direction is accessible in this experiment, meaning that the accessible information on the α-structure accessible corresponds to the typical distance between the α-strands along the transverse direction of the fibre, which appears as a bright spot at about 9.6 Å. Also visible is the diffuse ring at about 4.49 Å, arising from some other structures along the equator, larger than the distance between α-strands. A feature characteristic of the β-sheets configuration in the equatorial direction is the sharp peak at 4.7 Å, corresponding to the typical distance between the chains constituting the β-sheets.
It is nervertheless important to note that the exact description of the peaks and what feature they arise from in the hair is not well-defined and authors of different papers can have different interpretations for them.

The fits, which were performed according to the procedure given in detail in Section 4.6, return a set of parameters that characterises the different peaks arising from the crystalline structure of the hair fibres. Among the parameters analytically accessible for the different functions, the most relevant based on the paper by Kreplak et al. (2004) [3], are the relative intensities of the different peaks and the peak positions.
In the following sections a comparison between all the waterfall plot lines with respect to the positions of the three peaks, as well as to their relative intensities, is presented as a function of tensile strain.
The waterfall plots give an idea of the general behaviour of the fibres under extension and show the possible disappearance or emergence of peaks during extension.
For every extension value, the plot presents the SAXS intensities. The low-q region is not possible to fit but it is followed by the peaks from the α-configuration at about 0.6 Å^{-1} and the broad intensity, fitted as two peaks, but hardly distinguishable to the naked eye.

5.1. Stress-strain curves

The environment, in particular the level of humidity, strongly influences the stress-strain behaviour of hair fibers.
As observed by several authors in previous works and discussed in Section 2.4, the main variation concerns the limit between the elastic and plastic deformation regions. All the stress-strain curves are shown in Figure 5.1. These lines at the bottom arise from the installation of the sample in the chamber and from returning to zero after fracture. The strong final drop in load is due to fibre breakage or to the manual release of the clamps at the end of the measurements, and is therefore not relevant.
At the lowest humidity, 20% RH, the elastic region extends up to between 5% and 10% strain. Indeed, after the first two extensions, respectively to 1% and 5%, the relaxation of the fibres indicates elastic deformation. From the third extension onwards (i.e. to 10%), the curve exhibits plastic deformation at each step. Despite the partial relaxation of the fibres at each step, due to the relatively long measurement time, a typical quasiplastic deformation curve is observed. In the following we write plastic instead of

quasiplastic for simplicity, although plastic is usually reserved for metals.
For 20% RH, the load drops at around 30% extension.

For the other series, the elastic region ends earlier during the second extension step, that is between 1% and 5%.
It is also worth noting that the fibres withstand larger extensions and start to break later than at 20% RH: around 50% extension for 40% RH, 60% for 60% RH and 80% at 80% RH. The measurement at 50% relative humidity was stopped earlier and therefore provides only partial results, but these do not contradict the trends observed in the other series.
This observation suggests that humidity increases the plasticity of the fibre, indeed wet fibers present a lower yield stress and tensile stress. In summary a wet hair will break later at higher strain but the plastic transformation and fracture occurs at lower stress. [6]

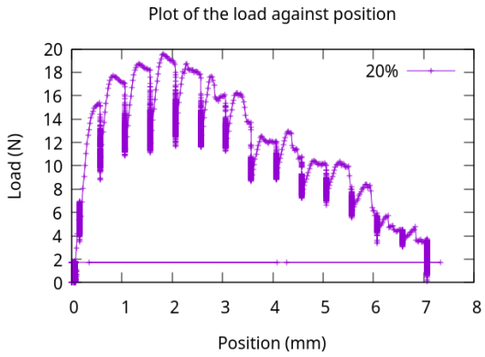

(a) Plot of the stress-strain curve for the series at 20% relative humidity.

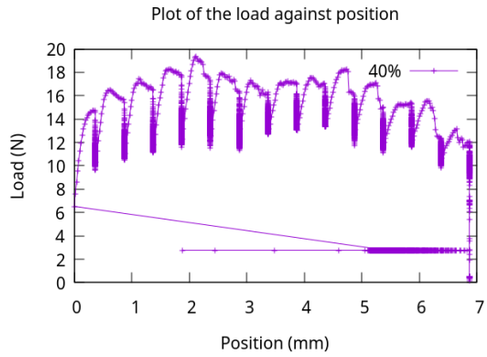

(b) Plot of the stress-strain curve for the series at 40% relative humidity.

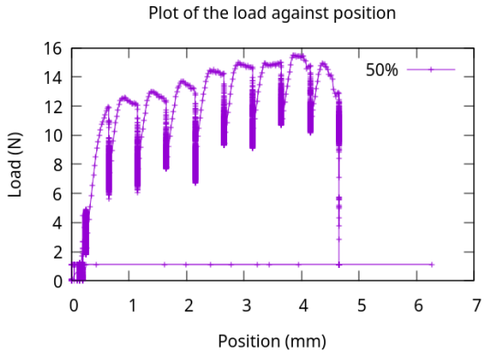

(c) Plot of the stress-strain curve for the series at 50% relative humidity.

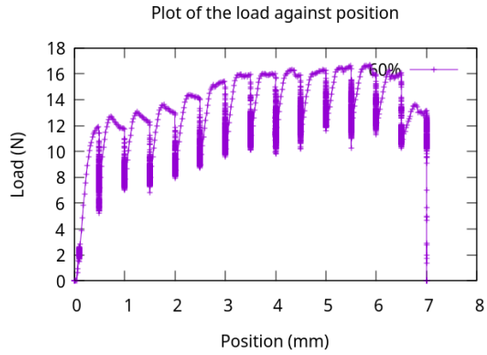

(d) Plot of the stress-strain curve for the series at 60% relative humidity.

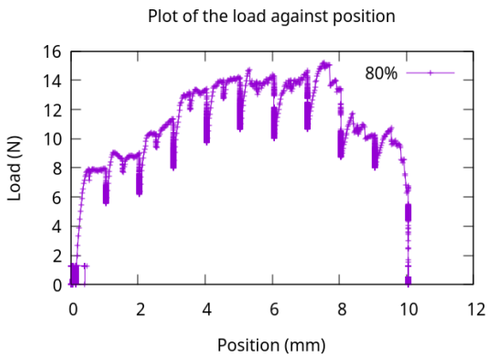

(e) Plot of the stress-strain curve for the series at 80% relative humidity.

Figure 5.1.: Stress-strain curves for different relative humidities.

The compliance of the machine has not been measured for this experiment, and

the values are taken from Johannes Liebhart's master's thesis [13]. The compliance obtained there for the machine was $C_{machine} = (1.47 \pm 0.03) \times 10^{-3}\,\mathrm{mm\,N^{-1}}$, which is much smaller than the load involved in the experiment with human hair. It is to be expected since hair are relatively soft materials, easily deformable.

5.2. Comparison of the peak analysis here and in literature

The ratio between the heights of the different peaks was evaluated in the paper by Kreplak et al. (2004) [3] and the plots, shown in Figure 5.2, presenting the profiles obtained with the measurement of horse hairs, along the equator direction at 0%, 24%, 35% and 50% macroscopic strain. The evolution of the normalised intensity of the peaks at real space distances of 0.465 nm and 0.95 nm is also presented and shows a first linear increase between 0% and 10% macroscopic strain, followed by a plateau until 20% macroscopic strain. The relative intensity increases then again linearly until the end of the measurement at 52% macroscopic strain.
Comparing this to our results at 20% relative humidity, the intensity of the second peak is initially higher than the first one, and shows a much less pronounced linear decrease until 15% extension from 1.25 to 1 in intensity, and then remains more or less constant between intensities of 1 and 1.1 (Figure 5.11).

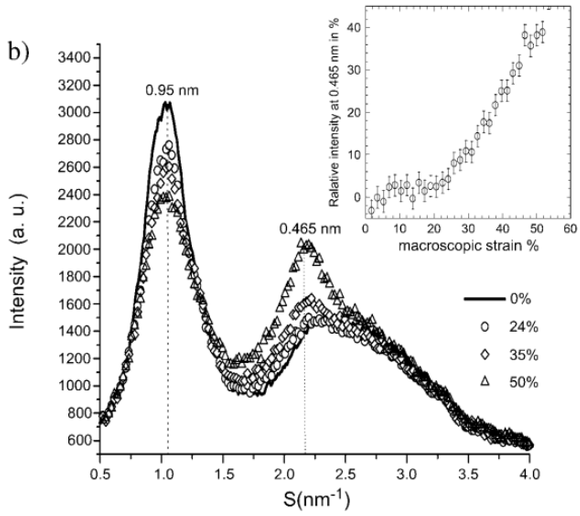

Figure 5.2.: Plot taken from the paper by Kreplak et al. [3] presenting the profile extracted along the equator at 0, 24, 35 and 50% extension. The inset is the relative intensity of the second peak at 0.465 nm to the first peak at real space distance of 0.95 nm.

In comparison, a similar analysis has been done here and will be presented in more details in the following sections for each series. The ratios between the different peak intensities as well as the normalised intensity of each peak (normalised by the intensity at the beginning of the experiment). One plot, of the series 20% relative intensity at 0% of macroscopic strain, is given as an example for the data obtained in Figure 5.3.

The relative intensities of the peaks are also discussed in the paper by Kreplak et al. (2004) for horse hairs. First of all it is important to note that the first peak at 0.5 nm for horse hairs is much higher than the one appearing at 0.465 nm, whereas in the case considered here, human hair exhibits peaks with comparable relative intensities. Indeed, it is not surprising that different species may exhibit different scattering intensities.

In the two experiments, it can be noticed that even though the general course is in both cases comparable, the peaks have not been identified and fitted with the same procedure. Figure 5.4b aims to give a simplified representation of the peaks identified

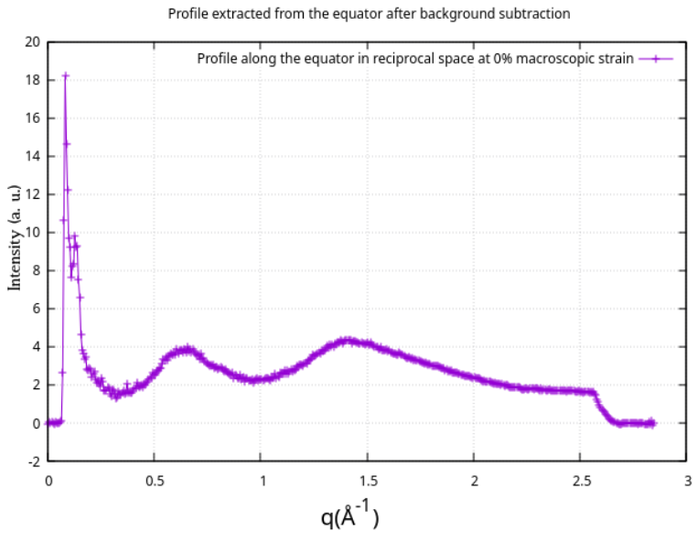

Figure 5.3.: Data extracted from the equator, in reciprocal space, of the measurement at 20% relative humidity and 0% macroscopic strain for human hair.

in the paper by Kreplak et al. (2004) [3], whereas Figure 5.4a shows our fit approach for human hair.

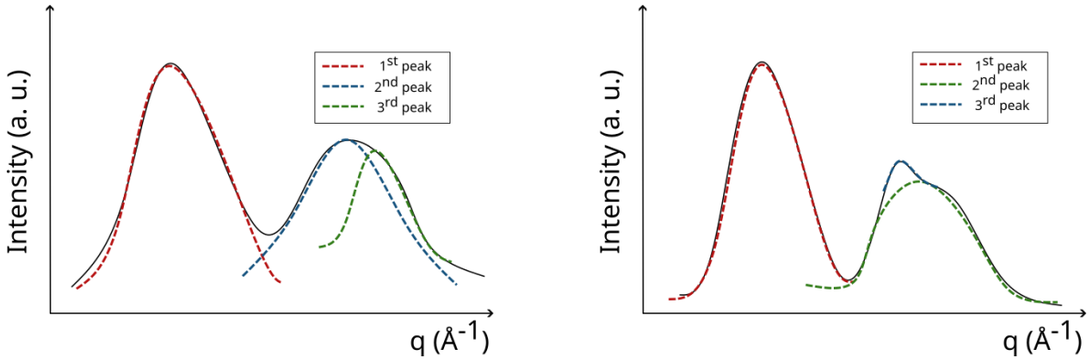

(a) Sketch of the data obtained with human hair and the peaks fitted.

(b) Sketch of the data obtained with horse hair and the peaks fitted. The original plot is from Kreplak and et al. and in Figure 5.2.

Figure 5.4.: Comparison between the data and the fit in this thesis 5.4a and in the paper by Kreplak et al. (2004)[3] 5.4b.

5.3. Uncertainties

In this experiment, the uncertainties affecting the final results arise from different sources and processes. The aim of this section is to give a better description of them and to clarify which ones can be quantified and which can only be evaluated qualitatively.
The possible breakage of some fibres in the bundle during extension will influence the scattering intensity since it changes the scattering volume, affecting in particular the later stage of the experiment.
Similarly, an extension not exactly the same for each fibre, or fibres having naturally slightly different mechanical properties, will impact the analysis of the peak positions.
On the plots presenting the peak heights in Sections 5.4.2, 5.5.2, 5.7.2 and 5.8.2, where the trend is a plateau, the small variations are probably partially do to this type of uncertainties.

Another source of uncertainty concerns the errors in the fitting models and the fitting procedure itself. The standard deviations were given by the fit programm, as well as the uncertainties in the different parameters: peak positions, ratio of the peak heights, and relative heights. They have been computed with a program written by Martin Haßler, which is provided in Appendix A, and have been added to each plots in Sections 5.4, 5.5, 5.7 and 5.8. The uncertainties in the ratios have been computed directly with a Gnuplot script, using for the error propagation the formula:

$$\sigma_{I_{ratio}} = I_{ratio} \times \sqrt{\left(\frac{\sigma_{I_1}}{I_1}\right)^2 + \left(\frac{\sigma_{I_2}}{I_2}\right)^2} \tag{5.1}$$

$$\text{with } z = x/y \tag{5.2}$$

The experimental set-up can also be the cause of uncertainties, for example with the position of the detector or the acquisition procedure, but these cannot be quantified with this set-up and will therefore not be discussed here. It is a possible but probably minor additional error source.

The following details about the errors obtained and the results discussed in the present section apply to each series. The errors on the peak positions are typically between 1% and 5% of the data value, which is small enough to describe the general course of the plots. Moreover, the errors are presented for each strain and therefore we don't have statistical errors within a series. The general trends can thus be disscused even with error bars larger than the general evolution.
However, the oscillations around a mean value in the region at high strain can be safely considered as a plateau, since the variations arises very probabaly here from statistical uncertainites, for example coming from the scattering process.
For the relative heights, the typical error lies between 20% and 50%. because the scatter of single measurements is in this range, we describe and discuss the data and its evolution on the basis of the mean values.
In the case of the ratios between two heights, the errors on the ratios are between 20% and 60%, although the values vary less than for the other parameters. Once again, the descriptions are made with respect to the mean values and conclusions need to be taken in the light of the uncertainties.

5.4. Results for the series at 20% relative humidity

In the waterfall plot for the 20% relative humidity, shown in Figure 5.5 from 0% to 70% extension, There do not seem to be any new peaks appearing for elongated samples, as it would be expected, if the transition between α-to-β- configuration takes place [3].

5.4.1. Peak position

We first consider the variation of the peak position. In the case of horse hairs described by Kreplak et al. (2004) [3], the peak position of the first peak hardly changed and no value was given in the paper.
The first peak at about $q = 0.6\,\text{Å}^{-1}$ shows a slight shift during the first few percents of elongation as visible in Figure 5.6. The peak position shifts towards higher values in reciprocal space, meaning that the distance between the α-helix decreases linearly until 20% extension, changing from $2\pi/0.635 = 9.89\,\text{Å}$ without extension, to 9.38 Å at 20% corresponding to a change of 5.5% of the distance in reciprocal space.
When the fibres are further elongated, the distance hardly varies any more, only varying between 9.45 Å and 9.31 Å until the end of the measurement. As the peak arises from the transverse distance of the IFs (intermediate filaments), their distance in real space decreases with increasing strain.

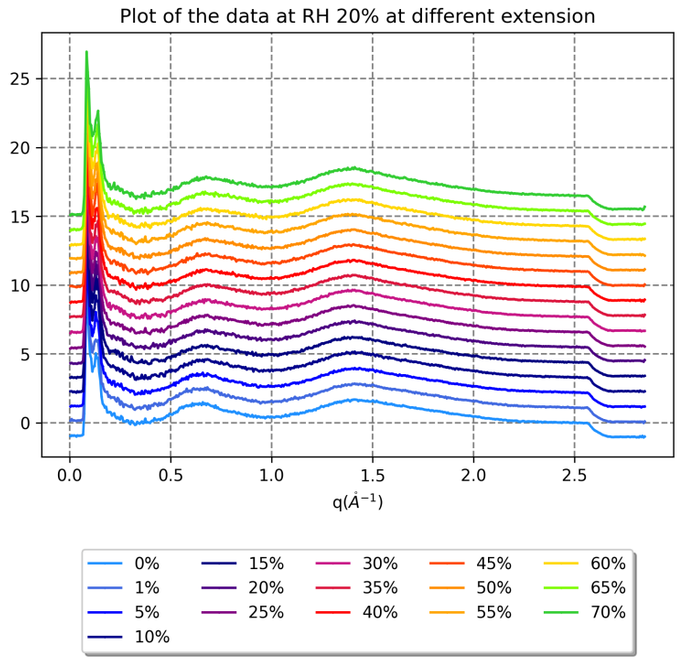

Figure 5.5.: Waterfall plot of the integrated data of the equatorial direction for the series at 20% relative humidity from 0% to 70% extension.

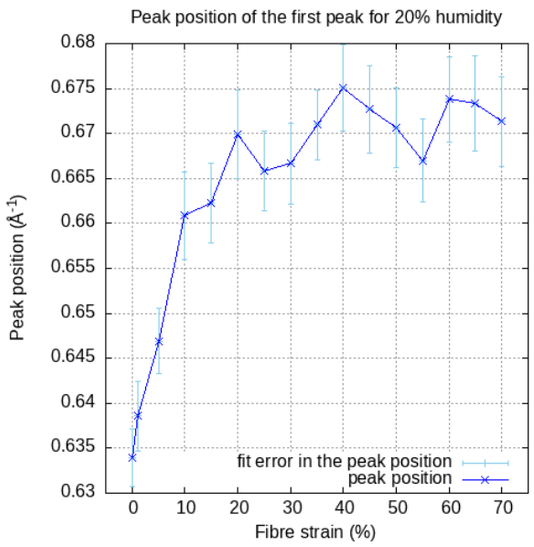

Figure 5.6.: Plot of the first peak position (in Å^{-1}) as a function of the strain in percentage of the initial length.

The second peak, whose position evolution is shown in Figure 5.7a, shifts towards smaller values in reciprocal space. The evolution is quite linear, but the changes are only of about 1.4%.

Similar to the second peak, the position of the third peak (see Figure 5.7b) shifts towards smaller values in reciprocal space, from about $1.67\,\text{Å}^{-1}$ at 0% extension to $1.625\,\text{Å}^{-1}$ at 70% extension, corresponding to a change of slightly more than 2.4%.

The stress-strain curve for the 20% relative humidity shown in Figure 5.1a, exhibits an elastic behaviour until 10% extension and exhibits a plastic region beyond.

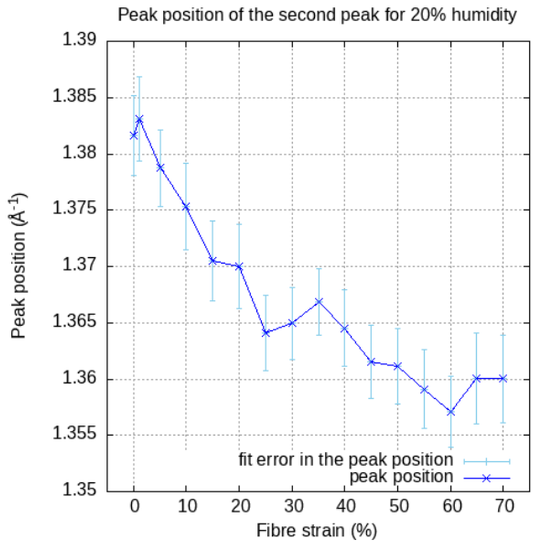

(a) Plot of the second peak position (in q-space in $Å^{-1}$) as a function of the elongation in percentage of the initial length.

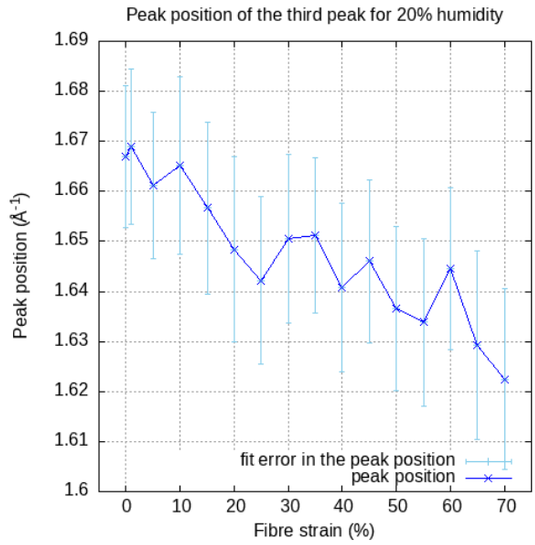

(b) Plot of the third peak position (in q-space in $Å^{-1}$) as a function of the elongation in percentage of the initial length.

Figure 5.7.: Positions of the second and third peak as a function of the extension percentage.

5.4.2. Peak intensities

The height of the peaks for the series at 20% relative humidities, normalised to its initial value, is shown for the first peak, the second peak and the third peak. Concerning the first peak in Figure 5.8, its intensity decreases linearly until a macroscopic strain of 20%, and with a decrease of the about 20% from the intial intensity ratio.
It then slightly increases until the end of the measurement, not regularly with variations of about 2.5%, and end up at 87% of the initial intensity.

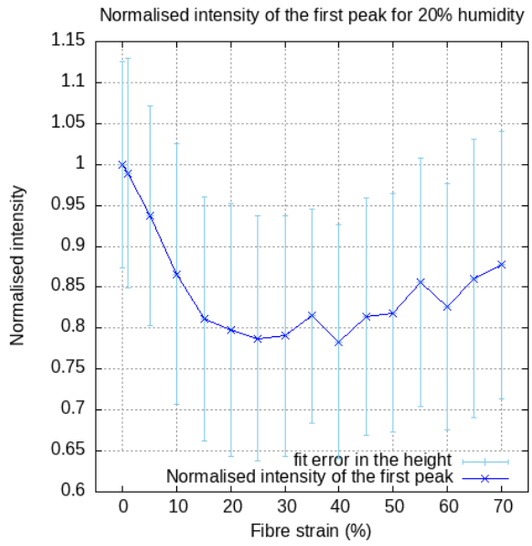

Figure 5.8.: Plot of intensity of the first peak normalised by the intensity at the beginning of the experiment.

The second peak (in Figure 5.9) sees its intensity increasing by 20%, from 0% to about 30% of the macroscopic strain, followed by a plateaued region until the fracture of the fiber and the end of the measurement at 70% macroscopic strain, with oscillations only within the range of 0.5% of the initial intensity.

The normalised intensity evolution of the third peak is more difficult to describe and to extract a general behaviour from. It is shown in Figure 5.10. It reaches a lowest point at 30% of macroscopic strain, before increasing again until the end at 70% macroscopic strain. The intensity values exhibit some scatter, but seem to increase at strains highers than 25% macroscopic strain.

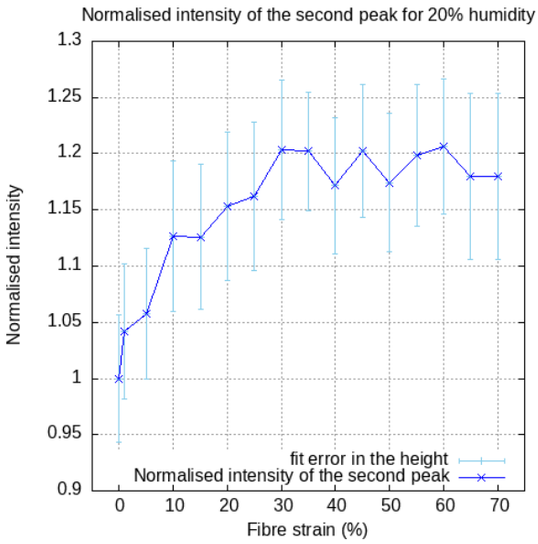

Figure 5.9.: Plot of the normalised intensity of the second peak.

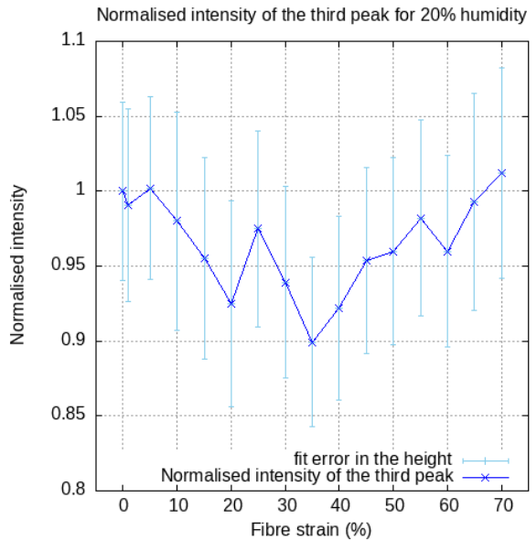

Figure 5.10.: Plot of the normalised intensity of the third peak.

Figure 5.11 shows the ratio of the intensities of the second and first peak. There is a linear increase of this ratio until about 30% macroscopic strain up to an increase of 50% of the second peak comparing with the first, before a slight decrease until the end of the measurement, reaching a ratio equal 1.35. The two peaks start at about the same height, and the second reaches 1.35 times the height of the first one.

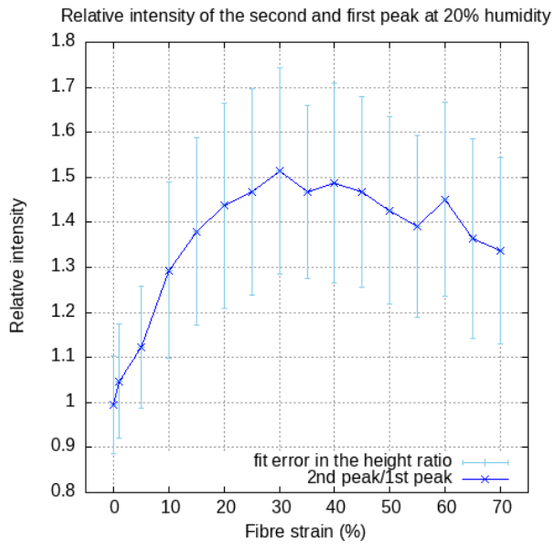

Figure 5.11.: Plot of the relative intensity between the second and the first peak.

For the third peak, its relative intensity with the first and second peaks are plotted respectively in Figures 5.12 and 5.13. Figure 5.12 shows an increase of about 18% of the relative intensity of the third peak with respect to the first one between 0% and 25% fibre strain. This tendency is similar to the evolution of the second peak relative to the first one. Both exhibit an intensity increase during elongation relative to the first peak.
Considering Figure 5.13, the ratio between the third and the second peak decreases

by around 18.5% between 0% and 20% elongation. After a local maximum at 25% macroscopic strain, the curve had its global minimum at 35% strain, corresponding to an decrease of 25% comparing with the initial ratio. The last region between 35% and 70% strain exhibits an increase and ends up with the ratio being 19% smaller than the one at 0% strain.
In short, the intensity of both the second and third peak increases during the elastic region between 0% and 20%, the second more than the third, while the intensity of the first peak decreases. The first peak intensity changes significantly more than the one of the second and third peak.

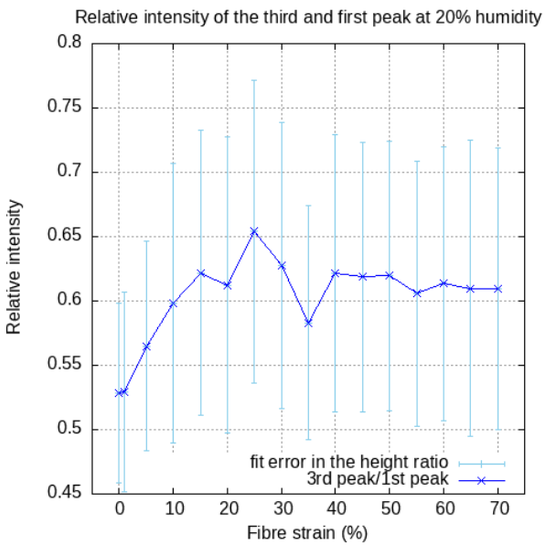

Figure 5.12.: Plot of the relative intensity of the third and the first peak.

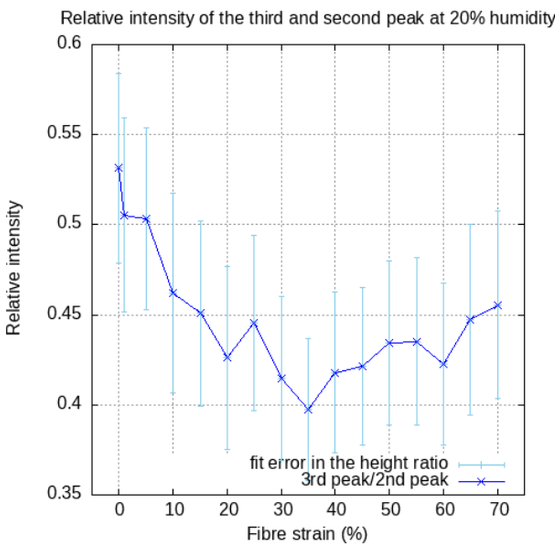

Figure 5.13.: Plot of the relative intensity of the third and the second peak.

owards smaller values in reciprocal space space by less

To summarise the first observations, there are clear differences between our results for human hair and the results from Kreplak et al. [3] for horse hairs: As similarities we have an initial increase and the plateau of the intensity ratio between the second and the first peak, but at a much higher value (>1 instead of about 0.1). Differently, we do not observe the strong increase of a new peak evolving at macroscopic strains higher than 25%.

5.5. Results for the series at 40% relative humidity

As for the previous series, the waterfall plot in Figure 5.14 doesn't suggest any apprearance of a new peak at around 0.46 nm while the sample is elongated.

5.5.1. Peak position

For the position of the first peak 5.15, the behaviour is similar than for the series at 20% RH, with a linear displacement of the peak until 25% extension. It corresponds to a decrease of the mean distance between α-helix stands in reciprocal space by about 6.2%, from 9.7 Å to 9.3 Å.
Beyond this point and until the end of the measurement at 70% of the extension of the fibre, the distance in q-space increases again by 1.4%, less regularly than during the first part of the measurement.

The second and third peak positions vary of about the same percentage at 40% than at 20% humidity and are shown respectively in Figure 5.16a and Figure 5.16b.

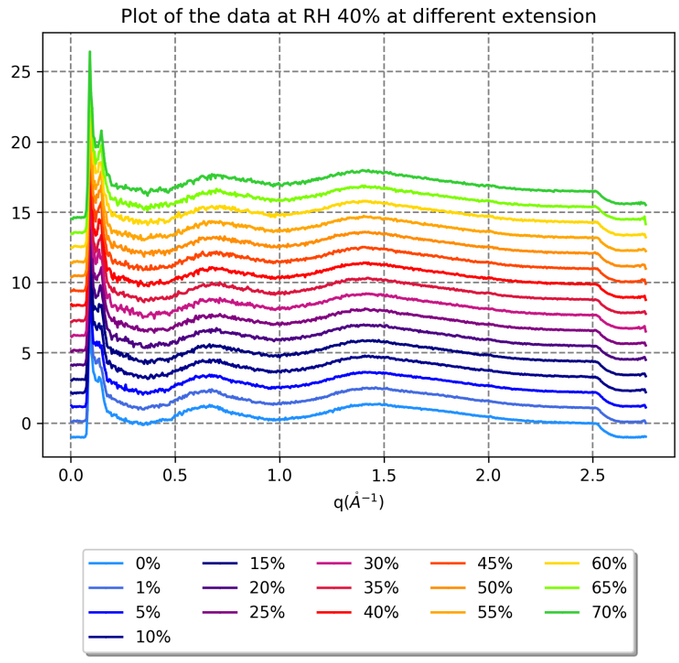

Figure 5.14.: Waterfall plot of the integrated data of the equatorial direction for the series at 40% relative humidity from 0% and 70% extension.

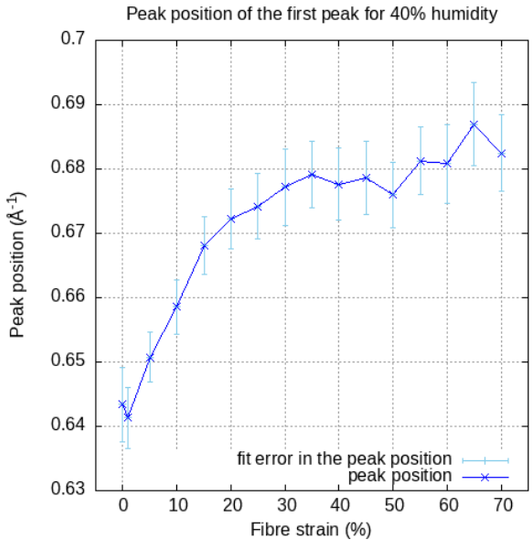

Figure 5.15.: Plot of the first peak position (in Å^{-1}) depending on the elongation in percentage of the initial length.

The position of the second peak is located at the beginning at 1.39 Å^{-1} and shifts again slightly towards smaller values in reciprocal space by less than 2%.
The third peak also slightly shifts towards smaller values by about only 3%.

5.5.2. Peak intensity

Similarly to the previous series, the normalised intensity of the first peak, presented in Figure 5.17, decreases with linear behaviour from 0% until 25% macroscopic strain, with intensity diminution of about 16%. The intensity stays then relatively equal, varying between 84% and 87% comparing with the initial intensity.

The second peak in Figure 5.18 is also varying the same than previously, with a smoother increase than in series at 20% RH, until 25% macroscopic strain, reaching about 18% more than the initial intensity. It is decreasing tendentially by about 5% -

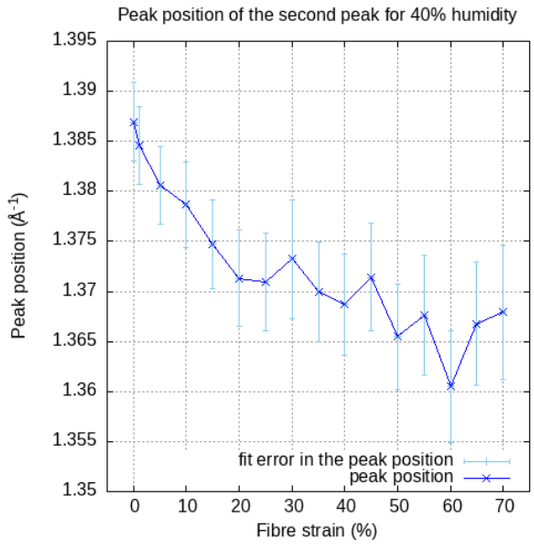

(a) Plot of the second peak position (in $Å^{-1}$) depending on the elongation in percentage of the initial length.

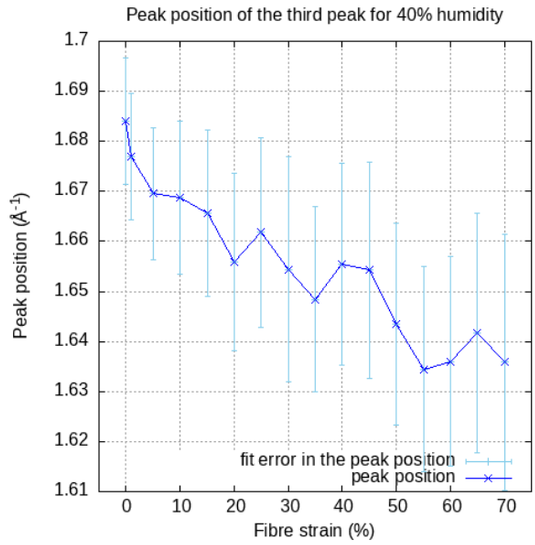

(b) Plot of the third peak position (in $Å^{-1}$) depending on the elongation in percentage of the initial length.

Figure 5.16.: Positions of the second and third peak depending on the fibre strain.

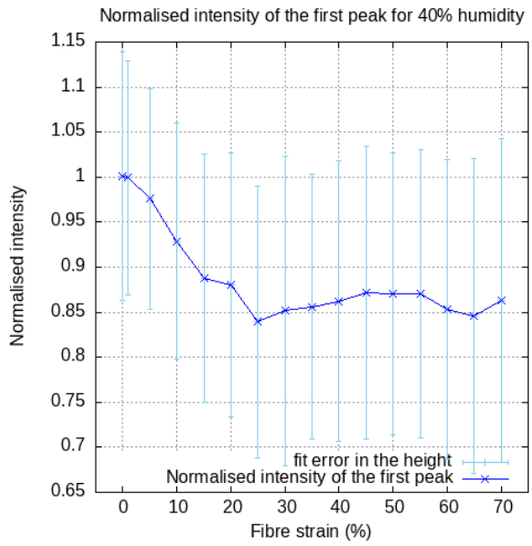

Figure 5.17.: Plot of the normalised intensity of the first peak.

6%, to end up 12% higher than the initial intensity at the end of the measurement at 70% macroscopic strain.

In the case of the third peak (in Figure 5.19), while it was decreasing before increasing again for the series at 20% RH, for this case at 40%, it decreases regularly although not smoothly until the end, ending up at an intensity 20% lower than at the beginning of the measurement.

The plot of the ratio of the second and first peak intensities against the strain in percent is shown in Figure 5.20.
The curve presents in a first step a linear behaviour from 0% extension up to about 25%, starting at an intensity of about 0.85 until 1.22 so an increase of 43.53%.
With further increase the two peaks keep a more constant intensity ratio, with an unregular evolution, ending up at strain 70% at an intensity of 1.1, leading to a general decrease of 9.84%.

The peak height ratios of the third and first peak (the plot is shown in Figure 5.21)

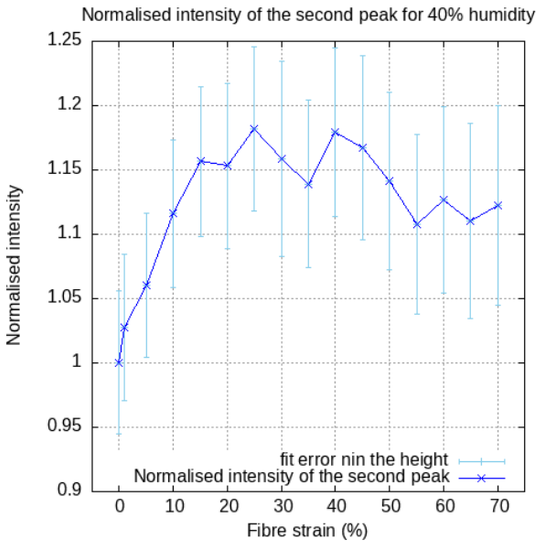

Figure 5.18.: Plot of the normalised intensity of the second peak.

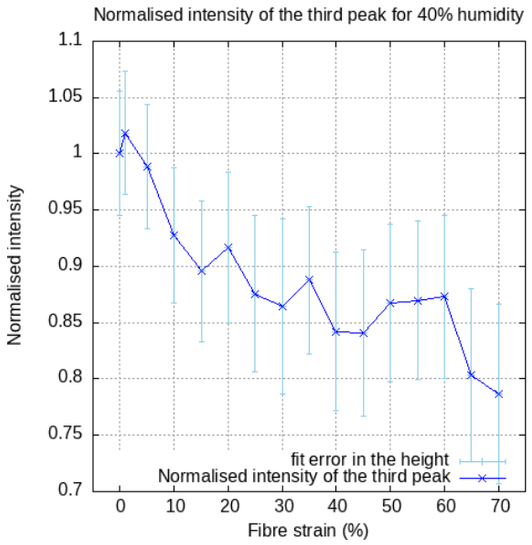

Figure 5.19.: Plot of the normalised intensity of the third peak.

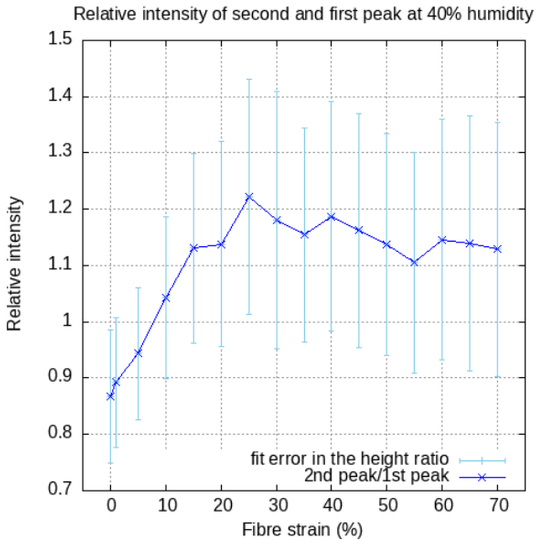

Figure 5.20.: Plot of the relative intensity of the second and the first peak.

looks a bit different than for the series at 20%, with tendentially constant values from the beginning of the measurement until 60%, with maximal variations of intensity within a window between 0.635 and 0.59. A drop is then observed during the last 10% extension from 60% and 70% from relative intensity 0.62 to 0.55.

The ratio between the intensities of the third and second peak (Figure 5.22), on the other hand, is similar to the series at 20% RH. The ratio drops significantly from 0% to 15% of fibre strain, from intensity ratio 0.7 to 0.55 (so about 21%) and is followed by a more gradual decrease until 0.5.

5.6. Results for the series at around 50% relative humidity

The series at 50% relative humidity was not carried through to completion, but only up to a macroscopic strain of 40%. Moreover, due to operational issues, the humidity during the measurements was not maintained as stable as in the other series.
As a result, even though comparing the values in this series from this series with those of the others could help to support the observations made, a full analysis of the peaks

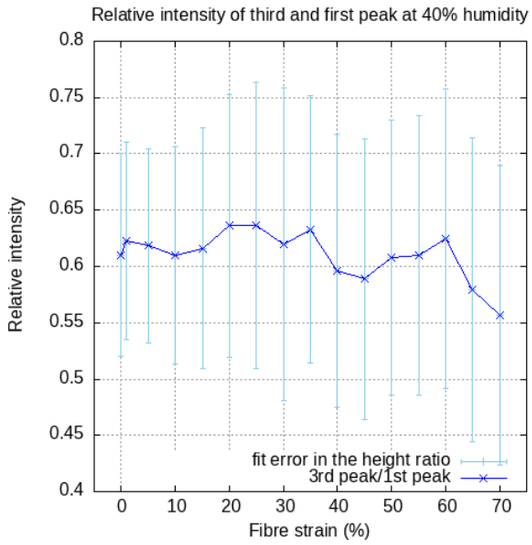

Figure 5.21.: Plot of the relative intensity of the third and the first peak.

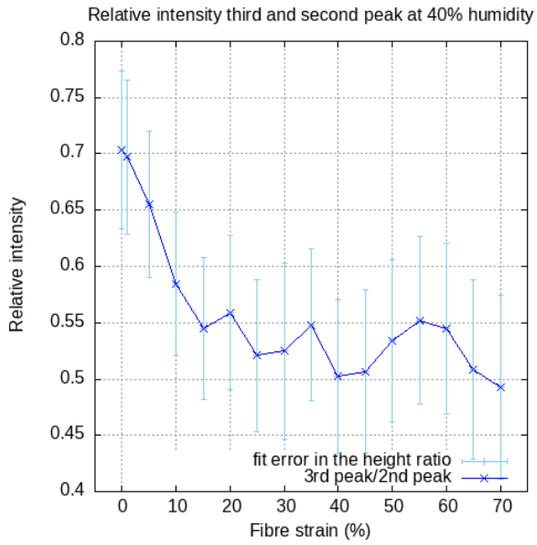

Figure 5.22.: Plot of the relative intensity of the third and the second peak.

would be incomplete and is therefore not undertaken here. The plots are nevertheless in the Appendix A.

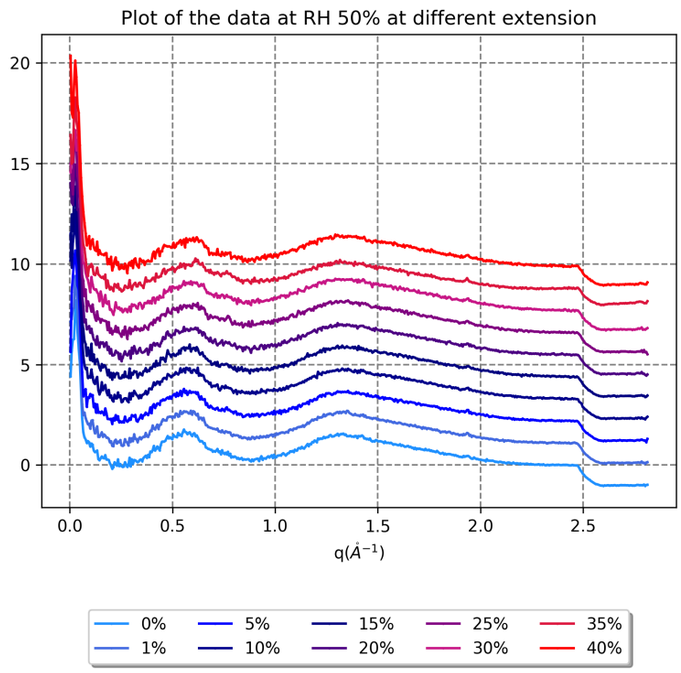

Figure 5.23.: Waterfall plot of the integrated data of the equatorial direction for the series at around 50% relative humidity from 0% and 40% extension.

5.7. Results for the series at 60% relative humidity

The waterfall plot, shown in Figure 5.24 is, similarly than for the previous series, giving an overview of the intensities at different strains and a humidity of 60%.

5.7.1. Peak position

For the series at 60% relative humidity, the general course of the curve presented in Figure 5.25 and showing the evolution of the position of the first peak is similar than

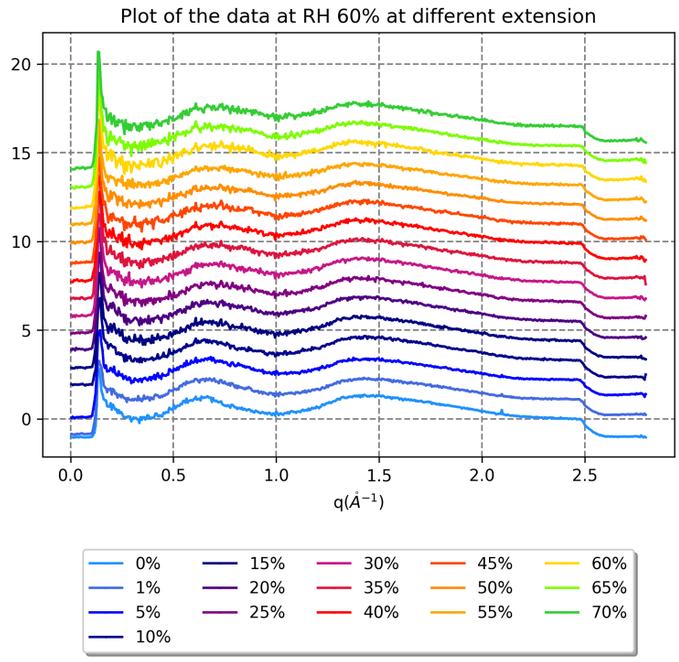

Figure 5.24.: Waterfall plot of the integrated data of the equatorial direction for the series at 60% relative humidity from 0% and 70% extension.

for the other series, with again a neat increase until about 30% extension, followed by a more flat region increasing only by about 1.5%.
At the beginning of the extension of the fiber, the position of the first peak starts at 0.63 Å^{-1} and increases up to 0.685 Å^{-1} when 30% extension is reached. That makes a change of about 8.7% which is higher than for the previous series.

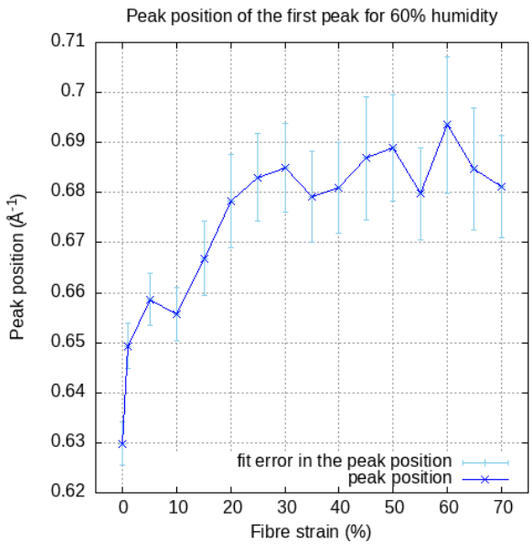

Figure 5.25.: Plot of the first peak position (in Å^{-1}) depending on the elongation in percentage of the initial length.

The peak position of the second peak follows again a similar course than the previous series, with a region between 25% and 50% where the position does not change a lot. The plot is shown in Figure 5.26a. The second peak shifts towards lower values in reciprocal space, with a linear tendancy, but large deviations. The peak position at the beginning of the measurement is at 1.38 Å^{-1} and is at 65% at about 1.35 Å^{-1}. The last point at 70% fibre strain is a bit higher at about 1.36 Å^{-1}.

For the third peak, whose plot is presented in Figure 5.26b, the evolution of the position is also similar than what have been observed in the previous series. It is located at the beginning of the measurement at $1.68\,\text{Å}^{-1}$ and shifts again towards smaller values in reciprocal space down to $1.642\,\text{Å}^{-1}$ at 60% fibre strain and $1.645\,\text{Å}^{-1}$ for 70% fibre strain.

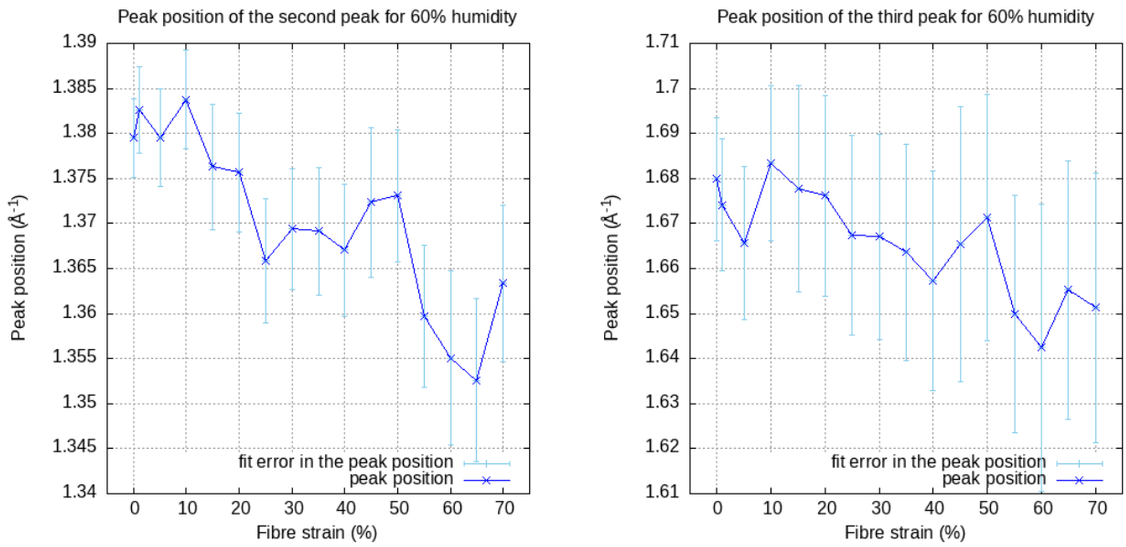

(a) Plot of the second peak position (in Å^{-1}) depending on the elongation in percentage of the initial length.

(b) Plot of the third peak position (in Å^{-1}) depending on the elongation in percentage of the initial length.

Figure 5.26.: Positions of the second and third peak depending on the fibre strain.

5.7.2. Peak intensity

For consistency within this series and because the values for 0% and 10% seem off the general tendencies in each intensity plot, the description of the evolution will be done in this section only from 5% macroscopic strain on. Since the peak positions of the two peaks did not present such singularity nor the stress-strain curve presented in Section 5.1, it is possible that this arises from an unprecise positioning of the sample at the beginning of the experiment.

The first peak, shown in Figure 5.27, starts as the previous series, with a decrease of its intensity until 25% fibre strain and droping by 15%. Follows then a constant region between until 45% strain, followed by a decrease until 50% strain, down to 78% of the intial intensity. Intensity increases again after, to end up at about 92% of the initial intensity.

The second peak follows closer the behaviour of the previous series and its plot is in Figure 5.28. It starts increasing from 5% until 20% fibre strain by an increase of 20% of the intensity at 5% fibre strain. It then decreases more slowly, before a strong drop and equally fast increase around 55% strain, to end up at the end of the measurement at an intensity 10% higher than the first intensity.

The normalised intensity of the third peak (from 5% fibre stain) shown in Figure 5.29 stays stable around the intial value until approximatly 40% macroscopic strain, it drops then until 50% strain down to an intensity 18% lower, followed by an increase up to 60% strain up to an intensity 5% lower than the initial one at 5% strain.

All peaks have a significant drop of intensity at 55% macroscopic strain, which could then be a systematic feature, due to the experiment conditions and not changes in the sample.

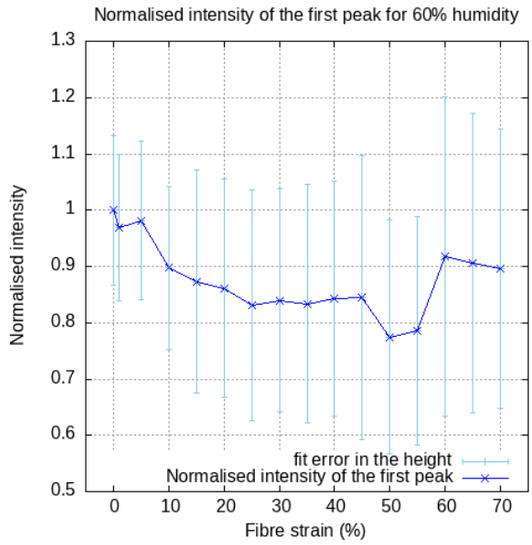

Figure 5.27.: Plot of the normalised intensity of the first peak.

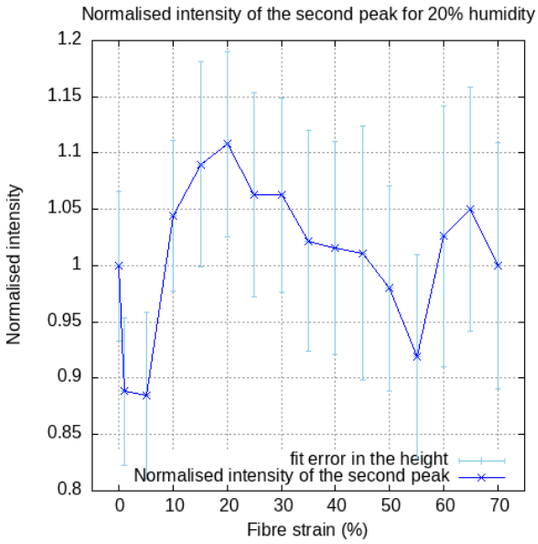

Figure 5.28.: Plot of the normalised intensity of the second peak.

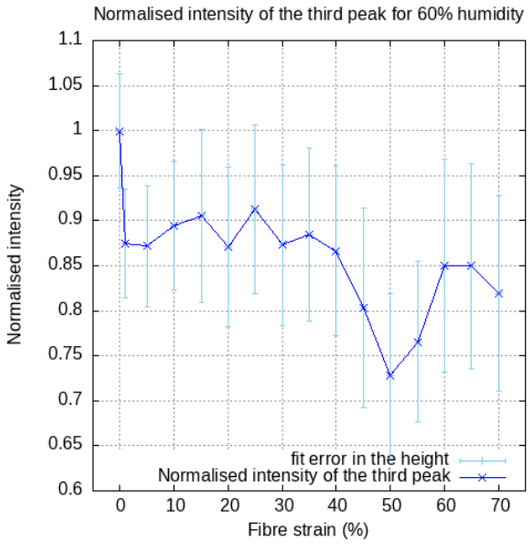

Figure 5.29.: Plot of the normalised intensity of the third peak.

The relative intensity for the series at 60% RH, between the second and the first peak is presented in Figure 5.30.
From 5% extension on, the ratio increases strongly until 20% strain from ratio 0.75 to 1.1, meaning the second peak gets higher than the forst one. The ratio decreases then until the end of the measurement down to 0.95 (except for a higher point at around 50% strain, coinciding with the singularities already observed.

The ratio between the intensity of the third and the first peak is presented in Figure 5.31. The first point for 0% strain is again higher than the one at 1%. From 1% on and until 25% strain, the ratio increases, similarly than the previous series, with an intensity starting at 0.58 and going up to 0.71 (22% increase). This ratio decreases then down to an intensity of 0.59 at 70% strain, even though the deacrese is there not regular or smooth.

About the ratio between the third and second peak height (in Figure 5.32), the course is once again similar to the one of the curve in the previous series: the ratio drops rapidly between 0% and 20% of the fibre strain, from intensity 0.76 down to 0.6 corresponding to a diminution of 20% of the initial value. The ratio stays then relatively constant, until the end of the measurement at a strain of 70%. The intensity is oscillating between 0.58 and 0.66 but does not present any general trend.

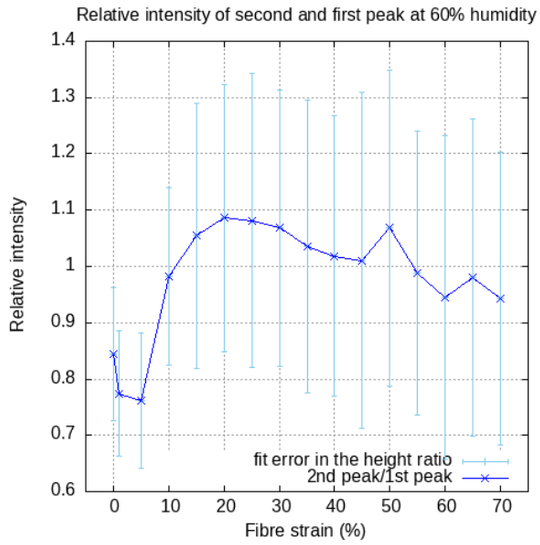

Figure 5.30.: Plot of the relative intensity of the second and the first peak.

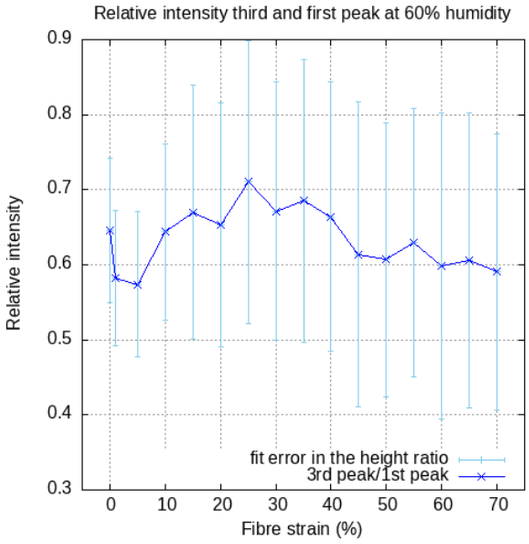

Figure 5.31.: Plot of the relative intensity of the third and the first peak.

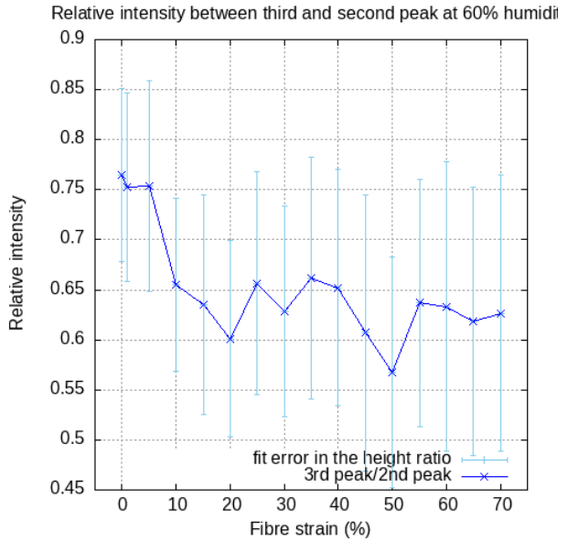

Figure 5.32.: Plot of the relative intensity of the third and the second peak.

5.8. Results for the series at 80% relative humidity

This series is a slight different measurement since measurement was done every 10% extension instead of every 5%. The extension speed as well as the time between steps were however kept the same in order to not have any variation in the relaxation process of the fibers.
In this series the variation of the distance is difficult to describe precisely also due to the smaller number of points.
Figure 5.33 shows a waterfall plot of the intensities at 80% humidity and different strains.

5.8.1. Peak position

The position change of the first peak is shown in Figure 5.34. It presents again a rapid shift towards higher values in q-space, from 0% until 40% strain. The peak is initially at $0.63\,\text{Å}^{-1}$, and ends up at $0.56\,\text{Å}^{-1}$ at 40% strain, corresponding to a decrease of 3.1%. The plot presents a plateau between 40% and 70% strain, remaining around $0.655\,\text{Å}^{-1}$. A further increase up to $0.67\,\text{Å}^{-1}$ is observed from 70% to 100%, which corresponds to 2% more, and a total shift of 6.3%.

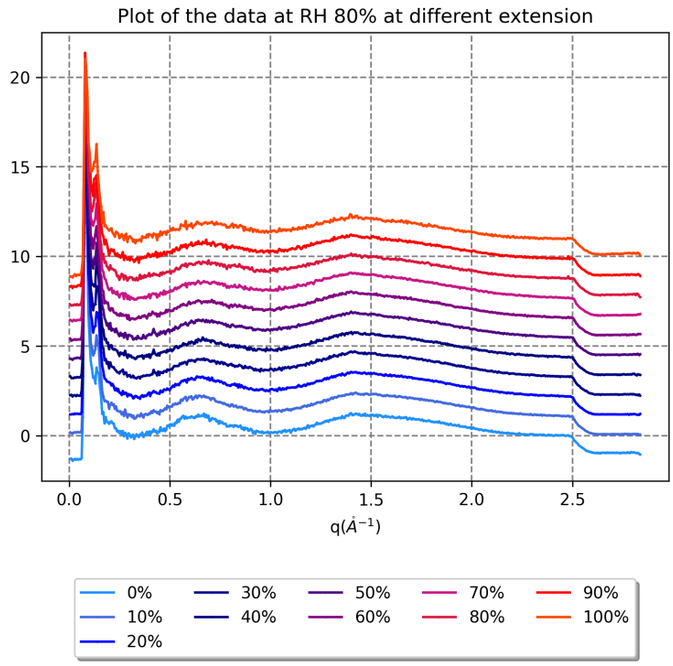

Figure 5.33.: Waterfall plot of the integrated data of the equatorial direction for the series at 80% relative humidity from 0% and 70% extension.

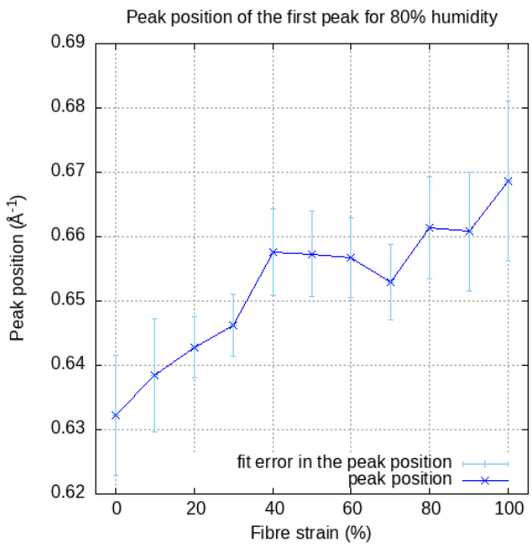

Figure 5.34.: Plot of the first peak position (in Å^{-1}) depending on the elongation in percentage of the initial length.

About the evolution of the second and third peaks, the plots are presented respectively in Figure 5.35a and in Figure 5.35b.
The second peak follows a similar evolution than the ones observed previously for the other relative humidities: it starts at $1.39\,\text{Å}^{-1}$ and reaches $1.372\,\text{Å}^{-1}$ at the end of the measurement at 100% strain. It is a change of about 1%, and is, as an example, shifting by half of the value in the course of the experiment at 20% RH.

The third peak is more difficult to describe, since the peak is located at $1.695\,\text{Å}^{-1}$, increases up to $1.725\,\text{Å}^{-1}$, then decreases back to $1.695\,\text{Å}^{-1}$ at 70% strain. There is then another small increase to $1.715\,\text{Å}^{-1}$ at 80% and going down again to $1.7\,\text{Å}^{-1}$ at 100% strain. All the variations are, however, small and the smaller amount of points makes the description of the general course more difficult.

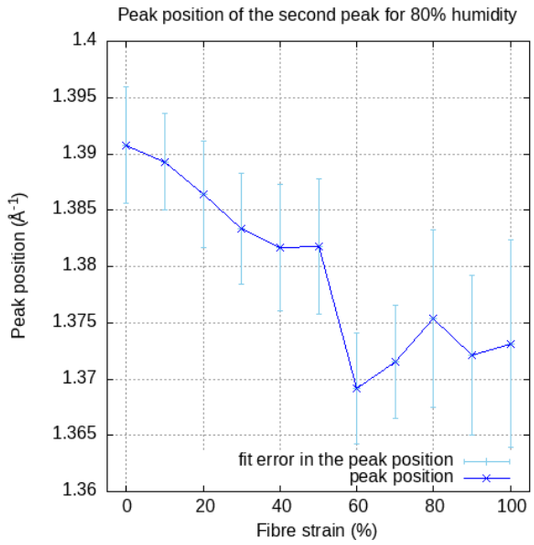

(a) Plot of the second peak position (in $Å^{-1}$) depending on the elongation in percentage of the initial length.

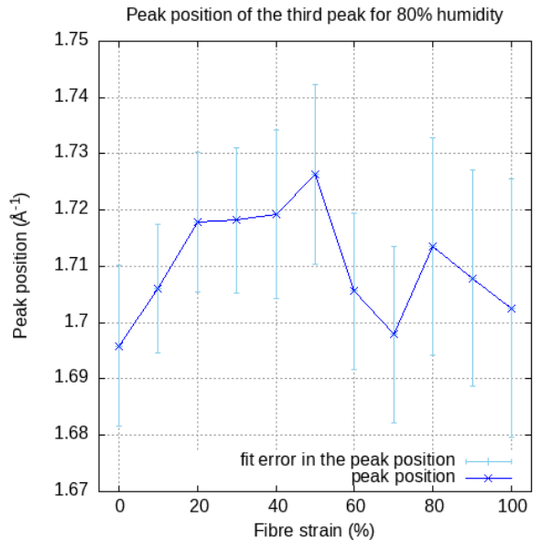

(b) Plot of the third peak position (in $Å^{-1}$) depending on the elongation in percentage of the initial length.

Figure 5.35.: Positions of the second and third peak depending on the fibre strain.

5.8.2. Peak intensity

The next figures show the evolution of the intensities of all peaks. Between the strain of 80% and 100%, every plot presents a significative change of course. Because the stress-strain curve of this experiment presents a net decrease from 80% strain on, this late drop is probably not relevant for the experiment and only due to the important breakage of some fibres.

The first peak, whose plot is presented in Figure 5.36, shows a smooth decrease from the measurement start until 40% of macroscopic strain, dropping to 75% of the initial intensity. Between the strains 40% and 80%, probably fibre fracture occured.

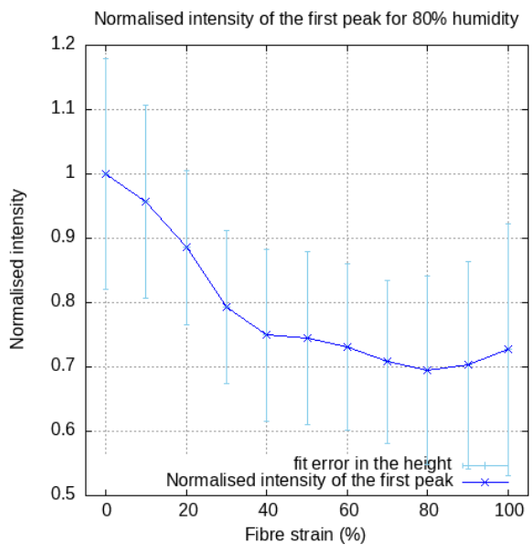

Figure 5.36.: Plot of the normalised intensity of the first peak.

The next plot (in Figure 5.37) is the normalised intensity of the second peak. Once again it follows a comparable course than for the previous series. It starts with increasing rapidly between 0% and 20% strain (up to an increase of 27%), continues until 50%, reaching an intensity increase of 37%.

The third peak intensity (Figure 5.38) tendentially decreases during the whole mea-

surement, with a peak between 50% and 80% of the fibre strain, reaching a maximum at 60% for an intensity reaching 90% of the initial one. At the end of the measurement the intensity is about 74% of the initial intensity.

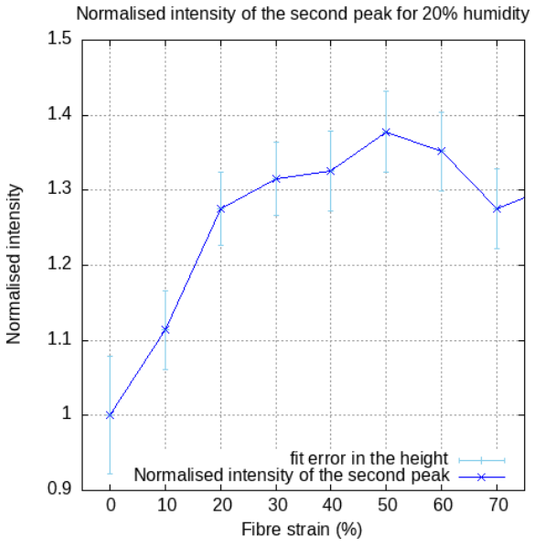

Figure 5.37.: Plot of the normalised intensity of the second peak

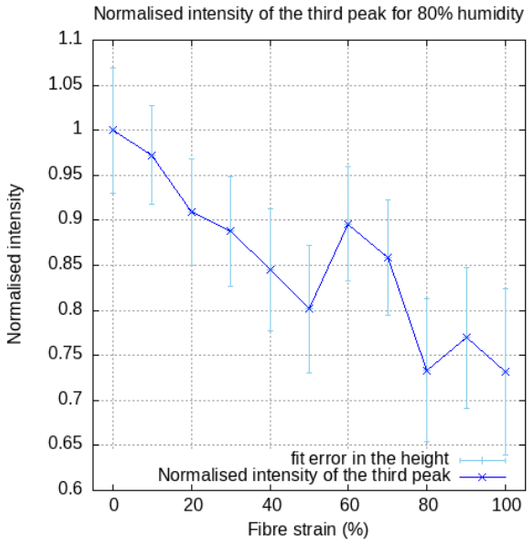

Figure 5.38.: Plot of the normalised intensity of the third peak.

The curve of the ratio between the second and first peak is shown in Figure 5.39. Its course is similar than for the series at 20% RH. It increases strongly between 0% and 50% from intensity of 0.75 up to 1.4, corresponding to an increase of the ratio of about 86%. It is then followed by a region until 80% where the intensity ratio doesn't vary significantly.

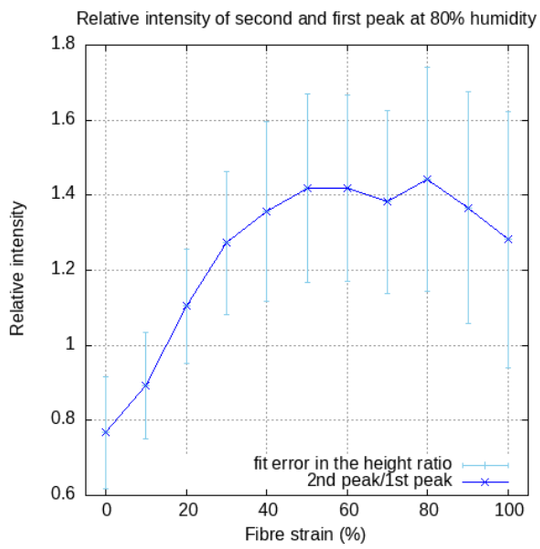

Figure 5.39.: Plot of the relative intensity of the second and the first peak.

Figure 5.40 shows the ratio between the intensity of the third and the first peak. This one in particular suffers from the lack of point measured. What can be observed is a general increase from the beginning of the measurement until 60%, from 0.68 until 0.82. The ratio decreases then again until reaching the initial ratio of 0.68 at the end of the measurement.

The evolution of the relative intensity of the third and the second peak, whose plot is show in Figure 5.41, is similar to the one for the previous series, with a net decrease between 0% and 50% strain from 0.9 to 0.5 (decrease of 44%). It then stays globally

constant until the end of the measurement at 100%, with few variations between intensities 0.5 and 0.6.

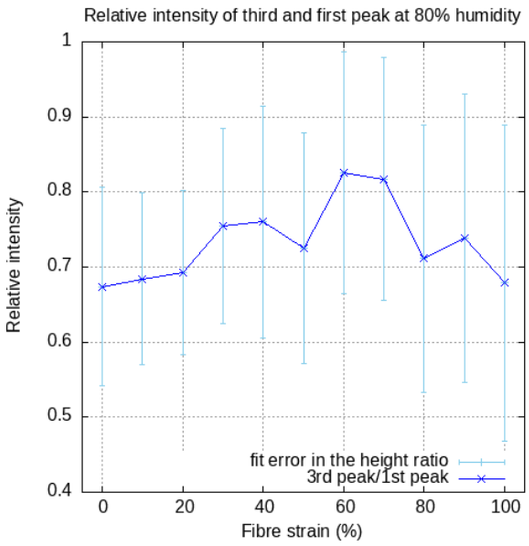

Figure 5.40.: Plot of the relative intensity of the third and the first peak.

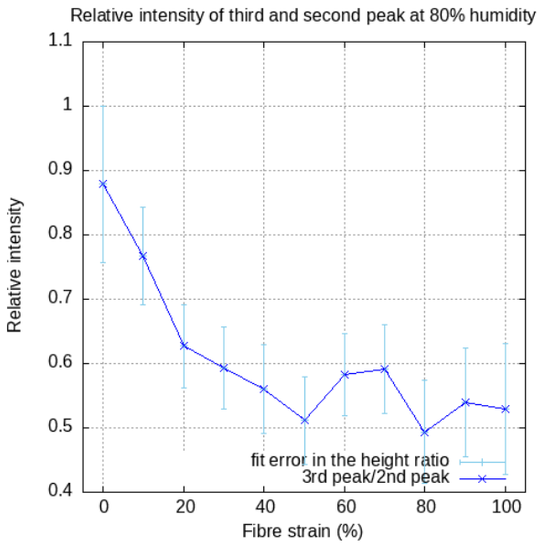

Figure 5.41.: Plot of the relative intensity of the third and the second peak.

6. Discussion

The results of this experiment, aiming to better understand and characterise the α-to- β transition of keratin within the intermediate filaments of human hair fibres, are compared with earlier works, in particular with the results obtained by Kreplak et al. in the paper "New Aspects of the α-Helix to β-Sheet Transition in Stretched Hard a-Keratin Fibers" (2004)[3], in which the experiment was conducted on horse hair, dry, in water and with steam.
There are notable differences between the results presented in this thesis, shown in Figure 5.3 for human hair and those from the aforementioned paper shown in Figure 5.2 for horse hairs: first of all, the X-ray intensities of each peak are different, which also leads to different peak assignments during the data analysis. The first peak and the two next peaks have, for human hair, about the same intensity, while the first peak for the horse hair is much higher than the others.
In the model presented by Kreplak et al, a strong peak on the equatorial direction at about 4.7 nm arises when the β-sheets configuration appears. In that sense, one can hypothesise that there are initially more β-sheet regions in human hair than in horse hair, also without any strain.
The general shape of the profile is also likely influenced by both the species of hair used and the experimental setup: Kreplak et al. [3] conducted the experiment with a synchrotron radiation source and used a single fibre, whereas the results of the present thesis were obtained with a laboratory X-ray source using a bundle of 20 fibres.
Previous studies [1, 6] have discussed the impact of extension rates on the mechanical behaviour of materials, such as complex polymer-like structures like hair. The procedure of straining used in Kreplak et al.'s paper was of 1.7% macroscopic strain per step [3], which is less than what was used here and this extension rate variation could also have an influence. Regarding the exposure time, it was 10 minutes for horse hair, and it is said that some relaxation was observed. With the exposure time of 30 minutes here for human hairs, the relaxation was therefore probably not much different in the experiment by Kreplak et al. to the one conducted here on human hair. [3]

The aspect of molecular and structural differences depending on the species has been presented by D. A. Greenberg and D. S. Fudge in [30] and S. Breakspear et al. in [31], where the different mechanical behaviour corresponding to the matrix content compared with the IFs in the hair is discussed.
Indeed, in the two papers cited above, the mechanical characteristics of the different parts of the hair fibres are described and give a deeper understanding of differences that can arise from hair from different species, depending on the intermediate filament and matrix proportion.
Feughelman proposed in 1959 [32] a model of the matrix embedding the IFs, a model used again by Breakspear et al. [31] The matrix, typically described as a relatively amorphous cross-linked polymeric material [31] containing a large variety of proteins including amorphous keratin, appears to be less hydrophilic than the IFs and therefore protects the IFs from hydration and prevents the α-keratin softening, which happens in wet conditions. [30]
The tensile modulus or Young's modulus also varies depending on the matrix proportion. The more matrix there is in the fibre, the higher is the tensile modulus [30].
The composition of hair from different species, the percentage of matrix and the different parameters, is provided in Greenberg and Fudge's paper [30]. The data on the matrix were measured using techniques from different papers [33, 34, 35]. According to the table in [30], human hair is constituted of more matrix than horse hair, the matrix comprising 31.5% and 24.0% of the fibre, respectively.
It is therefore very likely that this also has an effect on the structural change of hair

during loading at different levels of humidity, which could explain the differences between the experiment conducted here and the one carried out by Kreplak et al. in 2004 [3]. With a larger proportion of matrix material, human hair will be less sensitive to humidity and the elastic and plastic regions happen for human and horse at different strain. Typically, the elastic region reaches higher stress for horse hair than for human hair, as presented in Figure 2 in the reference [30].

We will now discuss the results in greater detail, starting with the normalised peak intensities and the intensity ratios. For horse hair (shown in Figure 5.2), the intensity of the peak labelled as the third peak in Figure 5.4b increases when the fibre is extended in steam, with a plateau between 10% and 20% macroscopic strain, and with a second strong linear increase from 20% until the end of the measurement.
With human hair, the peaks appear very similarly for every series at different relative humidities. In general, the first peak decreases and continues into a plateau. Some slight variations are visible, but since the peak intensity data also have large uncertainties, care should be taken to not over-interpret these results.
What is, however, clear is the absence of the second linear increase observed by Kreplak et al. This suggests no peak arising or disappearing during straining and thus no continuous α-to-β transition. It gives once again the idea that there could be more β-sheets in human hair fibres from the beginning.

The second parameter observed here for human hair, and that Kreplak et al. did not look at in their paper [3], is the evolution of the peak positions during the measurement. For each series at every humidity, the evolution of the peak position, directly linked to the typical distances within the structures, varies similarly with fibre strain. Although it does not suggest any structural transition that would be implied or facilitated by humidity, the evolution of the peak position can give hints as to how the structures are deformed.
The first peak, corresponding to a distance of about 0.9 nm, for which the literature suggests that it arises from the typical distance of keratin strands in the IFs, clearly decreases with fibre strain, and this occurs at all humidities. This behaviour is the simple and expected evolution for the most common type of materials undergoing elongation. Indeed, as the volume remains the same, an increasing length implies a decrease of the cross-section, meaning that such materials have positive Poisson's ratios, being defined in the article by Lakes as "the negative transverse strain divided by the axial strain in the direction of stretching force". [36].
In contrast, the next two peaks (labelled here second and third) show a shift towards larger values (in q-space) when the fibre is strained. Although this mechanical behaviour may seem counterintuitive at first sight, it is observed in materials with specific structures, and was first theorised by Roderic Lakes in 1986 [36]. Such materials are called auxetic materials and they exhibit a negative Poisson's ratio. This surprising property comes from an internal structure which is built in such a way that a strain in a certain direction will lead to an increase of the distances in the direction perpendicular to the strain. Examples of such structures are shown in the literature [36, 37] and one typical example is depicted in Figure 6.1. It can be realised for polymeric foams and porous materials, when for example the network does not have cross-links everywhere and the different elements of the structure can therefore draw away from each other [37].
Since matter is conserved, such processes lead to material density variations, for instance a decrease in density.
In our case, the two peaks presenting increasing distances during extension very probably arise from smaller structures in the IFs, like the molecular arrangements of proteins within the keratin strands or sheets. A possible interpretation could be the signal from lateral distances between chains in the β-sheet structure [3]. A reason that can be given for such distance increase during extension would be the anti-parallel β-sheets from two strands, whose distance (called d2 in the scheme 6.2) increases whereas the distances (d1 in the same scheme 6.2) between the pleated β-sheets consisting of two strands decreases. It is also suggested that unwinding of the two coiled strands during elongation leads to an increase distance of the amino-acids of the two strands. A model

presenting this auxetic behaviour of hair at the nanoscale is presented in Figure 6.2. The distance d1 shown by the green arrow is decreasing and the distance d2 shown by the red arrows is increasing. The black spots represent the carbon groups present along the strand that are not connected with the neighbouring group, and the dashed black lines are the hydrogen connections existing in anti-parallel β-sheets configuration along the strands between oxygen atoms and nitrogen-hydrogen groups, as described in the Figure 1 in Chapter 6 in Reference [38].
Such a hypothesis would, however, need further investigation in order to be validated. In order to better determine the origin of each peak and be able to trace the origin of the differences observed between the results in Kreplak's paper in this thesis, a second experiment should be done with horse hair, following the same procedure as what has been done with human hair in the present thesis. The results should then be compared once again with the existing ones to better compare each peak.

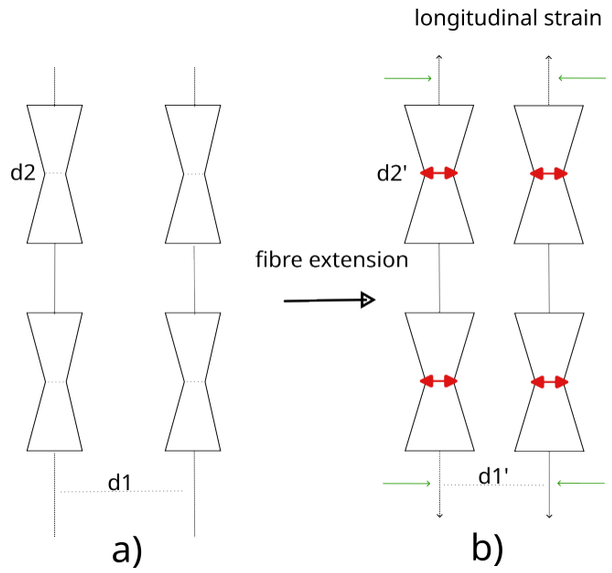

Figure 6.1.: Possible auxetic behaviour of two polymeric strands when strained in the logitudinal direction. a) the structure before extension and b) the distance modifications when strain is applied: d1>d1' (green arrows) and d2<d2' (red arrows)

The general trends of the peak positions for the series at 20% and 80% relative humidities (to take the extreme cases), present the same behaviour, with the difference that the evolution at 80% relative humidity is smoother, with a more uniform appearance of the position/elongation curve and a less pronounced plateau. This tendency is also visible in the mechanical behaviour. The stress-strain curve is similar for these two series but with a stress increasing slower with load at high humidity. It is also worth to note that this behaviour is gradually appearing with humidity increase, and do not axhibit any kind of thresholds. This also supports the hypothesis of no sudden transition.

Summarising, the differences between the experiment conducted by Kreplak et al. [3] and the results in the present thesis might arise from the use of human hair, the use of relative humidity instead of steam, the absence of transition from α- to β-configuration or the larger part of β-sheets initially or the set-up characteristics (number of fibres in the sample, measurement time ...).

An important open question is the amount of α-helices and β-sheets in human and horse hair. We were not able to measure the peak at 0.333 nm because of the size of the detector, for that reason a series with this peak visible would be helpful since one should observe the peak at 0.333 nm arising from the distance of residues in β-sheets [3].

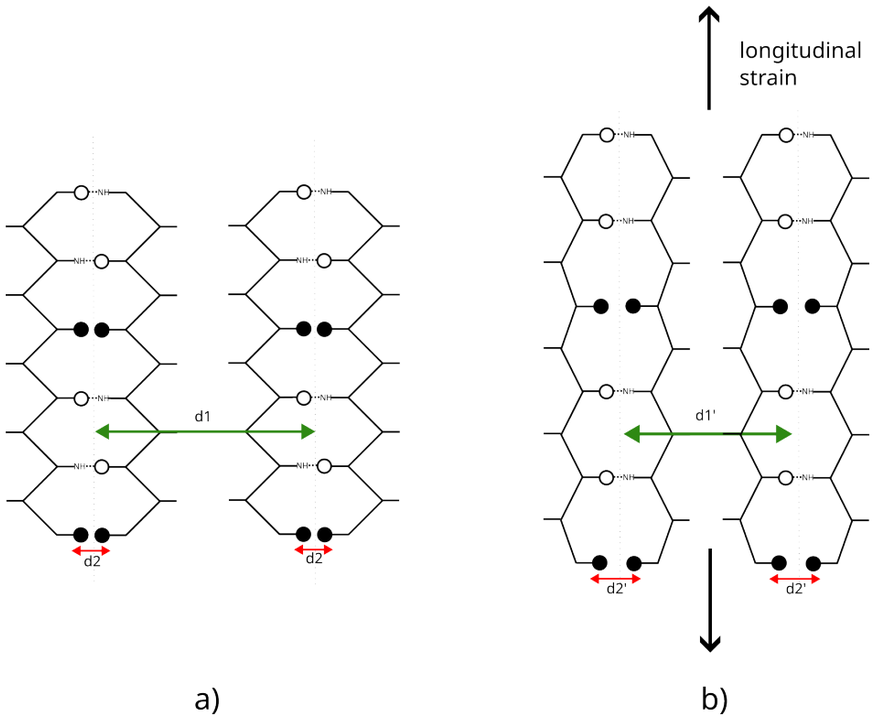

Figure 6.2.: Scheme of the auxetic behaviour of two β-sheets a) the structure before extension of one double strands and b) the distance modifications when strain is applied: d1>d1' (green arrows) and d2<d2' (red arrows). Two double strands are here shown.

With such second measurement, with horse hair and with human hair, one would access a larger part of the patterns, one could get enlightment on the amount of α-helices and β-sheets in human and horse hair, strained and unstrained, as well as the processes taking place during fibre strain and their origin: is steam required to observed an α-to-β transition? What are the differences between horse and human hairs, in the strained and unstrained state, on the nanoscale?
The use of spectroscopy like FTIR, NMR, circular dichroism, would be very helpful to interpret and classify experimental X-ray measurements, as they allow for a quantification of the amount of α-helices and β-sheets.

Abstract

The present thesis aims to present one aspect of the structural changes in human hair under humid conditions and longitudinal straining of the fibres.
Previous studies of hair fibres have provided evidence of a structural transition in keratin from α- to β-configuration, in different species while the fibre is strained in water or steam, showing the importance of humidity and stress for complex biological materials, such as mammalian hair. This thesis also builds on a previous thesis by Johannes Liebhart, with the goal of solving some of the problems encountered there, and to find out whether steam is necessary and if the α-to-β transition is happening at a certain threshold.
To improve the quality of the results compared with the previous thesis, a new window has been developped which was larger and closed with a plastic foil. The experiment was then conducted at relative humidities of 20%, 40%, 60% and 80%, with the fibre strain progressively increased during measurement, on a bundle of 20 fibres.
The equatorial part of the pattern was investigated here and it reflects, in reciprocal space, the fibre organisation across the cross-section ; for the distances at hand, it provides access to the distance between intermediate filaments, the size of the keratin strands, the distance between them, and their evolution under straining.

During extension, and that at any humidities, no significant peak changes, such as appearance or vanishing were observed. However, and during all the straining process, gradual changes occurred in the SAXS images and the mechanics of the fibres from low to high humidity. These results suggest no sudden transition from α-helices to β-sheets, but the changes in the peak positions as well as in the peak intensities give hints about how human hair deform during extension.

These results fundamentally vary from the ones found in literature, where changes have been observed in horse hair in the SAXS pattern, and which have been interpreted as a α-to-β transition of the keratin. These changes are absent in human hair, and such difference could be attributed to differences in the inner compositions and structures of human and horse hair. Another possible cause could be that both strain and steam are necessary to observe such changes.

Further SAXS investigations on horse hairs and human hair, as well as additional spectroscopy measurements, should clarify the differences between the two species.

Kurzfassung

Die vorliegende Arbeit hat zum Ziel, einen Aspekt der strukturellen Veränderungen in menschlichen Haaren unter feuchten Bedingungen und longitudinaler Belastung der Fasern darzustellen. Frühere Studien zu Haarfasern haben Hinweise auf einen strukturellen Übergang in Keratin von α- zu β-Konfiguration bei verschiedenen Arten geliefert, während die Haarfasern in Wasser oder Dampf gedehnt wurden. Dies zeigt die Bedeutung von Feuchtigkeit und Spannung für komplexe biologische Materialien wie Säugetierhaare. Diese Arbeit baut auch auf einer früheren These von Johannes Liebhart auf, mit dem Ziel, einige der dort auftretenden Probleme zu lösen und herauszufinden, ob Dampf notwendig ist und ob der α- zu β-Übergang ab einer bestimmten Schwelle stattfindet. Um die Qualität der Ergebnisse im Vergleich zur vorherigen Arbeit zu verbessern, wurde ein neues Fenster entwickelt, das größer war und mit einer Kunststofffolie verschlossen wurde, um die Feuchtigkeitsbedingungen zu garantieren. Das Experiment wurde dann bei relativen Luftfeuchtigkeiten von 20 %, 40 %, 60 % und 80 % durchgeführt, wobei die Belastung eines Bündels von 20 Fasern während der Messung schrittweise erhöht wurde. Der äquatoriale Teil des Musters wurde hier untersucht und spiegelt im reziproken Raum die Faserorganisation über den Querschnitt wider; Für die vorhandenen Entfernungen bietet es Zugang zum Abstand zwischen den intermediären Filamenten, zur Größe der Keratinketten, deren Abstand und deren Entwicklung unter zunehmender Spannung.

Bei unterschiedlichen Dehnungen und bei jeglichen Luftfeuchtigkeiten wurden keine signifikanten Änderungen wie Erscheinen oder Verschwinden von Peaks in den Röntgendiagrammen beobachtet. Während des gesamten Dehnungsprozesses traten jedoch nur allmähliche Veränderungen in den SAXS-Bildern und in der Mechanik der Fasern von niedriger zu hoher Luftfeuchtigkeit auf. Diese Ergebnisse deuten auf keinen plötzlichen Übergang von α-Helices zu β-Sheets hin, aber die Veränderungen in den Peak-Positionen sowie in den Peak-Intensitäten geben Hinweise darauf, wie sich menschliches Haar während der Dehnung verformt.

Diese Ergebnisse unterscheiden sich grundlegend von denen in der Literatur, in denen man bei Pferdehaar eine signifikante Änderung der Röntgendaten fand, die als α-zu-β-Übergang interpretiert wurden. Solche grundlegenden Unterschiede zwischen menschlichem und Pferdehaar - der α-zu-β-Übergang in Pferdehaar, der im menschlichen Haar fehlt, könnten auf Unterschiede in ihrer inneren Zusammensetzung und Struktur zurückgeführt werden. Eine weitere mögliche Ursache könnte sein, dass beide, Spannung und Dampf, notwendig sind, um solche Veränderungen zu beobachten.

Weitere SAXS-Untersuchungen an Pferdehaaren und menschlichem Haar sowie zusätzliche Spektroskopiemessungen sollten die Unterschiede in der Haarstruktur der beiden Lebewesen, Pferd und Mensch, klären.

References

[1] W. T. Astbury and A. Street. "X-ray studies of the structure of hair, wool, and related fibres.- I. General". In: *Philosophical Transactions of the Royal Society of London. Series A* 230 (Sept. 17, 1931), pp. 75–101. ISSN: 0264-3952, 2053-9258. DOI: 10.1098/rsta.1932.0003.

[2] E. G. Bendit. "The α–β Transformation in Keratin". In: *Nature* 179 (Mar. 9, 1957), pp. 535–535. ISSN: 0028-0836, 1476-4687. DOI: 10.1038/179535a0.

[3] L. Kreplak et al. "New Aspects of the α-Helix to β-Sheet Transition in Stretched Hard α-Keratin Fibers". In: *Biophysical Journal* 87 (July 2004), pp. 640–647. ISSN: 00063495. DOI: 10.1529/biophysj.103.036749.

[4] L. Kreplak, J. Doucet, and F. Briki. "Unraveling double stranded α-helical coiled coils: An x-ray diffraction study on hard α-keratin fibers". In: *Biopolymers* 58 (Apr. 15, 2001), pp. 526–533. ISSN: 0006-3525, 1097-0282. DOI: 10.1002/1097-0282(20010415)58:5<526::AID-BIP1028>3.0.CO;2-L.

[5] J. Cao. "Is the α–β transition of keratin a transition of α-helices to β-pleated sheets? Part I. In situ XRD studies". In: *Journal of Molecular Structure* 553 (Mar. 2000), pp. 101–107. ISSN: 00222860. DOI: 10.1016/S0022-2860(00)00538-X.

[6] Y. Yu et al. "Structure and mechanical behavior of human hair". In: *Materials Science and Engineering: C* 73 (Apr. 2017), pp. 152–163. ISSN: 09284931. DOI: 10.1016/j.msec.2016.12.008.

[7] J. Cao. "Is the α–β transition of keratin a transition of α-helices to β-pleated sheets. II. Synchrotron investigation for stretched single specimens". In: *Journal of Molecular Structure* 607 (Oct. 2001), pp. 69–75. ISSN: 00222860. DOI: 10.1016/S0022-2860(01)00901-2.

[8] M. Feughelman. "The physical properties of alpha-keratin fibers". In: *Journal of the Society of Cosmetic Chemists* 33 (1982), pp. 385–406.

[9] K. A. Minin et al. "Dynamic Transition from α-Helices to β-Sheets in Polypeptide Coiled-Coil Motifs". In: *Journal of the American Chemical Society* 139 (Nov. 15, 2017), pp. 16168–16177. ISSN: 0002-7863, 1520-5126. DOI: 10.1021/jacs.7b06883.

[10] D. J. Lyman, J. Murray-Wijelath, and M. Feughelman. "Effect of Temperature on the Conformation of Extended α-Keratin". In: *Applied Spectroscopy* 55 (2001).

[11] V. Stanić et al. "Local structure of human hair spatially resolved by sub-micron X-ray beam". In: *Scientific Reports* 5 (Nov. 30, 2015), p. 17347. ISSN: 2045-2322. DOI: 10.1038/srep17347.

[12] C. R. Robbins and R. J. Crawford. "Cuticle Damage and the Tensile Properties of Human Hair". In: *Journal of the Society of Cosmetic Chemists* 42 (1991), pp. 49–58.

[13] Johannes Liebhart BSc. "In-situ Measurement of the α-to-β Transition in human hair under varying conditions". Master of Science (MSc). Vienna: Universität Wien, 2025.

[14] A. R. M. Müllner et al. "Porosity at Different Structural Levels in Human and Yak Belly Hair and Its Effect on Hair Dyeing". In: *Molecules* 25 (May 2020), p. 2143. ISSN: 1420-3049. DOI: 10.3390/molecules25092143.

[15] C. Popescu and H. Höcker. "Hair-the most sophisticated biological composite material". In: *Chemical Society Reviews* 36 (2007), pp. 1282–1291. ISSN: 0306-0012, 1460-4744. DOI: 10.1039/b604537p.

[16] H. Kuzmany. *Solid-State Spectroscopy: an Introduction*. Second edition. Heidelberg: Springer, 2009. ISBN: 978-3-642-01478-9.

[17] N. W. Ashcroft and N. D. Mermin. *Solid state physics*. Fort Worth Philadelphia San Diego [etc.]: Saunders college publ, 1976. ISBN: 978-0-03-083993-1.

[18] B. D. Cullity. *Elements of X-ray diffraction*. Second ed. Addison-Wesley series in metallurgy and materials. Reading (Mass.) Menlo Park (Calif.) London [etc.]: Addison-Wesley publ, 1978. ISBN: 978-0-201-01174-6.

[19] A. Guinier. *X-ray crystallographic technology*. London: Hilger and Watts, Hilger Division, 1952.

[20] M. Boin et al. "Operating Liquid MetalJet X-ray Sources for Materials Research". In: (Dec. 2023). Ed. by Hans-Heinrich Braun et al., 5 pages, 0.718 MB. ISSN: 2673-7035. DOI: 10.18429/JACOW-FLS2023-WE1L4.

[21] B. E. Warren. *X-ray diffraction*. Facsim. ed. Dover books on physics and chemistry. New York: Dover, 1990. ISBN: 978-0-486-66317-3.

[22] O. Glatter. *Interference, Rayleigh–Debye–Gans Theory*. Elsevier, 2018, pp. 1–18. ISBN: 978-0-12-813580-8. DOI: 10.1016/B978-0-12-813580-8.00001-8.

[23] W. F. Hosford. *Solid Mechanics*. 1st ed. Cambridge University Press, Mar. 2010. ISBN: 978-0-521-19229-3.

[24] W. C. Young and R. G. Budynas. *Roark's formulas for stress and strain*. 7th ed. New York: McGraw-Hill, 2002. ISBN: 978-0-07-072542-3.

[25] URL: https://www.doli.de/produkte/edci-tischgeraete/edci22/#c227 (visited on 03/04/2026).

[26] URL: https://proumid.com/products/modular-humidity-generator/mhg32/ (visited on 03/04/2026).

[27] DECTRIS Ltd. *Technical Specifications DECTRIS EIGER®2 R 500K*. (Visited on 03/04/2026).

[28] *Materials Data on Al2O3 by Materials Project*. In collab. with The Materials Project. 2020. DOI: 10.17188/1187823. URL: https://www.osti.gov/servlets/purl/1187823/ (visited on 10/31/2025).

[29] J. Filik et al. "Processing two-dimensional X-ray diffraction and small-angle scattering data in DAWN 2". In: *Journal of Applied Crystallography* 50 (June 1, 2017), pp. 959–966. ISSN: 1600-5767. DOI: 10.1107/S1600576717004708.

[30] D. A. Greenberg and D. S. Fudge. "Regulation of hard α-keratin mechanics via control of intermediate filament hydration: matrix squeeze revisited". In: *Proceedings of the Royal Society B: Biological Sciences* 280 (Jan. 2013), p. 20122158. ISSN: 0962-8452, 1471-2954. DOI: 10.1098/rspb.2012.2158.

[31] S Breakspear et al. "The Matrix Revisited." In: *Journal of Cosmetic Science* 72 (2021), pp. 670–686.

[32] M. Feughelman. "A Two-Phase Structure for Keratin Fibers". In: *Textile Research Journal* 29 (Mar. 1959), pp. 223–228. ISSN: 0040-5175, 1746-7748. DOI: 10.1177/004051755902900305.

[33] J.M. Gillespie and M.J. Frenkel. "The diversity of keratins". In: *Comparative Biochemistry and Physiology Part B: Comparative Biochemistry* 47 (Feb. 1974), pp. 339–346. ISSN: 03050491. DOI: 10.1016/0305-0491(74)90063-7.

[34] J. M. Gillespie, P. J. Reis, and P. G. Schinckel. "The Isolation and Properties of Some Soluble Proteins From Wool". In: *Australian Journal of Biological Sciences* 17 (June 1964), pp. 548–560. ISSN: 0004-9417. DOI: 10.1071/BI9640548.

[35] E. G. Bendit and J. M. Gillespie. "The probable role and location of high-glycine-tyrosinc proteins in the structure of keratins". In: *Biopolymers* 17 (Nov. 1978), pp. 2743–2745. ISSN: 0006-3525, 1097-0282. DOI: 10.1002/bip.1978.360171119.

[36] R. Lakes. “Foam Structures with a Negative Poisson’s Ratio”. In: *Science* 235 (1987), pp. 1038–1040. ISSN: 00368075, 10959203.

[37] S. Puchegger et al. “Changing poisson’s ratio of mesoporous silica monoliths with high temperature treatment”. In: *Journal of Non-Crystalline Solids* 352 (Dec. 2006), pp. 5251–5256. ISSN: 00223093. DOI: 10.1016/j.jnoncrysol.2006.09.002.

[38] S. Saha et al. *Keratin as a Biopolymer*. Ed. by Swati Sharma and Ashok Kumar. Springer Series on Polymer and Composite Materials. Cham: Springer International Publishing, 2019, pp. 163–185. ISBN: 978-3-030-02900-5. DOI: 10.1007/978-3-030-02901-2_6.

List of Figures

1.1. Taken from [4]:«(a) Typical wide angle X-ray scattering (WAXS) pattern of hard α-keratin (horse hair). The fine 0.515 nm arc is visible on the meridian (vertical) above a broader arc around 0.5 nm, whereas the broad 0.98 nm maximum appears on the equator (horizontal). Notice the weak and diffuse ring around 0.45 nm. (b) Typical small angle X-ray scattering (SAXS) pattern of hard α-keratin (horse hair). The 6.7 nm arc is visible on the meridian (vertical). Our sample was oriented perpendicular to the beam with an error of $\pm 2°$ for the SAXS experiments; this is smaller than the natural angular extent ($\pm 10°$) of the 6.7 nm reflection. The intense ring is due to lipid scattering. (c) Typical WAXS pattern of β-keratin (horse hair stretched to 100% extension in steam). The 0.333 nm arc is visible on the meridian (vertical), whereas the 0.465 nm arc appears on the equator (horizontal) together with a broad 0.96 nm maximum.» . . 2

1.2. Comparison of the 2-D patterns with the old and the new set-up with a relative humidity of 20% at 0% extension. The high intensity Kapton peak between $q = 13\,\mathrm{nm}^{-1}$ and $14.5\,\mathrm{nm}^{-1}$in Fig. 1.2a from Liebhart's thesis is clearly absent in the new set-up in the corresponding range $q = 1.3$ to $1.45\,\mathrm{Å}^{-1}$ in Fig. 1.2b. Important to note is the rotation by 90° between the images from the image plates and from the Dectris detector. 6

1.3. Comparison of the integration with the old and the new set-up with a relative humidity of 20% at varying fibre strains. 7

2.1. Hierarchical structure of hair under various magnifications. Sketch from Alexander R. M. Müllner et al. [14]. 10

2.2. Section view of human hair (left) with light microscope by Robbins and Crawford [12] and dog hair (right), the SEM micrographs showing the difference in the medulla depending on the species. 10

2.3. Model of α- and β-configuration, taken from Yang Yu et al. [6] 11

2.4. Schematic spectrum of Mo at 35 kV, on the right is the resolved K_α line on an expanded scale [18]. 12

2.5. Schematic representation of a wave scattered by a crystal and the geometric construction of the Bragg's relation. 14

3.1. Hairs (10 mm length) glued on the paper frame with clamping length of 5 mm and 30 hairs (left) and clamping length of 10 mm and 20 hairs (right). 19

3.2. Load versus displacement for RH 60% for the sample with 5 mm gluing length (left) and 10 mm gluing length (right). 20

3.3. Open chamber with the sample (right) and the calibrant (left). Both sides of the frame have been already cut, the sample is ready for the experiment. 20

3.4. Picture of the EDCi 22 controller for performing tensile test experiments. 21

3.5. ProUmid MHG32 Humidity generator and humidity control circuit. (a) Humidity generator with deionised water container and controls for humidity and bath temperature. (b) Block diagram presenting the working principle of the ProUmid MHG32. The volume to be humidified being the chamber and the air supply a N_2 bottle, taken from the constructor's webpage [26]. 21

3.6. SAXS equipment in short configuration. The X-ray path, the detectors and controller are described on the figure. 22

3.7. Front side of the Eiger2 R 500k detector. 23
3.8. Two frames for measurement under the conditions 60% relative humidity and 10% extension. The right one shows a clear pattern while the left one should be ignored. 23

4.1. Glue testing: plots of the load against extension with epoxy glue (by UHU) and super glues (by UHU and Loctite). The numbers 15 and 100 in the text correspond to the tests at 15% and 100% humidity. 25
4.2. Scattering pattern of the Al_2O_3 at 20% humidity. 26
4.3. Screenshot of the image recorded to search for the sample at RH 80% with 1 second acquisition. The sample is visible in the vertical direction as a slightly lower intensity due to the absorption of the X-ray intensity by the hair with a transmission of about 0.9. 27
4.4. Plot of the intensity against q of the data before and after background subtraction, (a) 20% relative humidity, (b) 80% relative humidity. . . . 28
4.5. Plot at the different steps of background subtraction: raw data (dark red), after subtraction of the chamber background (red) and after subtraction of the sample background (orange). The fit with parabola to define the minimum of the region is in black dashed line and the linear function is shown in blue. 29
4.6. Plot of three backgrounds with clamps at distance: 10 mm (dark blue), 13 mm (blue) and 16.5 mm (light blue). 30
4.7. Results of the fit of the experimental data for the two step steps of the fitting procedure. The data are for the 20% relative humidity and 0% extension. 31

5.1. Stress-strain curves for different relative humidities. 34
5.2. Plot taken from the paper by Kreplak et al. [3] presenting the profile extracted along the equator at 0, 24, 35 and 50% extension. The inset is the relative intensity of the second peak at 0.465 nm to the first peak at real space distance of 0.95 nm. 35
5.3. Data extracted from the equator, in reciprocal space, of the measurement at 20% relative humidity and 0% macroscopic strain for human hair. . . 36
5.4. Comparison between the data and the fit in this thesis 5.4a and in the paper by Kreplak et al. (2004)[3] 5.4b. 36
5.5. Waterfall plot of the integrated data of the equatorial direction for the series at 20% relative humidity from 0% to 70% extension. 38
5.6. Plot of the first peak position (in $Å^{-1}$) as a function of the strain in percentage of the initial length. 38
5.7. Positions of the second and third peak as a function of the extension percentage. 39
5.8. Plot of intensity of the first peak normalised by the intensity at the beginning of the experiment. 39
5.9. Plot of the normalised intensity of the second peak. 40
5.10. Plot of the normalised intensity of the third peak. 40
5.11. Plot of the relative intensity between the second and the first peak. . . 40
5.12. Plot of the relative intensity of the third and the first peak. 41
5.13. Plot of the relative intensity of the third and the second peak. 41
5.14. Waterfall plot of the integrated data of the equatorial direction for the series at 40% relative humidity from 0% and 70% extension. 42
5.15. Plot of the first peak position (in $Å^{-1}$) depending on the elongation in percentage of the initial length. 42
5.16. Positions of the second and third peak depending on the fibre strain. . 43
5.17. Plot of the normalised intensity of the first peak. 43
5.18. Plot of the normalised intensity of the second peak. 44
5.19. Plot of the normalised intensity of the third peak. 44
5.20. Plot of the relative intensity of the second and the first peak. 44
5.21. Plot of the relative intensity of the third and the first peak. 45

5.22. Plot of the relative intensity of the third and the second peak. 45
5.23. Waterfall plot of the integrated data of the equatorial direction for the series at around 50% relative humidity from 0% and 40% extension. . . 45
5.24. Waterfall plot of the integrated data of the equatorial direction for the series at 60% relative humidity from 0% and 70% extension. 46
5.25. Plot of the first peak position (in $Å^{-1}$) depending on the elongation in percentage of the initial length. 46
5.26. Positions of the second and third peak depending on the fibre strain. . 47
5.27. Plot of the normalised intensity of the first peak. 48
5.28. Plot of the normalised intensity of the second peak. 48
5.29. Plot of the normalised intensity of the third peak. 48
5.30. Plot of the relative intensity of the second and the first peak. 49
5.31. Plot of the relative intensity of the third and the first peak. 49
5.32. Plot of the relative intensity of the third and the second peak. 49
5.33. Waterfall plot of the integrated data of the equatorial direction for the series at 80% relative humidity from 0% and 70% extension. 50
5.34. Plot of the first peak position (in $Å^{-1}$) depending on the elongation in percentage of the initial length. 50
5.35. Positions of the second and third peak depending on the fibre strain. . 51
5.36. Plot of the normalised intensity of the first peak. 51
5.37. Plot of the normalised intensity of the second peak 52
5.38. Plot of the normalised intensity of the third peak. 52
5.39. Plot of the relative intensity of the second and the first peak. 52
5.40. Plot of the relative intensity of the third and the first peak. 53
5.41. Plot of the relative intensity of the third and the second peak. 53

6.1. Possible auxetic behaviour of two polymeric strands when strained in the logitudinal direction. a) the structure before extension and b) the distance modifications when strain is applied: d1>d1' (green arrows) and d2<d2' (red arrows) 57
6.2. Scheme of the auxetic behaviour of two β-sheets a) the structure before extension of one double strands and b) the distance modifications when strain is applied: d1>d1' (green arrows) and d2<d2' (red arrows). Two double strands are here shown. 58

A.1. Stress-strain plot at around 50% RH i
A.2. Waterfallplot at around 50% RH i
A.3. Plot of the first peak position (in $Å^{-1}$) depending on the elongation in percentage of the initial length. i
A.4. Position of the second and third peaks depending on the fibre strain. . ii
A.5. Plot of the relative intensity of the first peak. ii
A.6. Plot of the relative intensity of the second peak ii
A.7. Plot of the relative intensity of the third peak. ii
A.8. Plot of the intensity ratio between the second and the first peak. iii
A.9. Plot of the intensity ratio between the third and the first peak. iii
A.10. Plot of the intensity ratio between the third and the second peak. . . . iii

A. Appendix

A.1. Results of the series at 50% RH

In Section A.1the stress-strain plot, the waterfall plot and the results of the experiment at around 50% RH are presented. The incertainties were not computed for this series. The experiment was aborted before after 45% of the fibre strain and the relative humidity being not stable, an analysis of the data was not sensible.

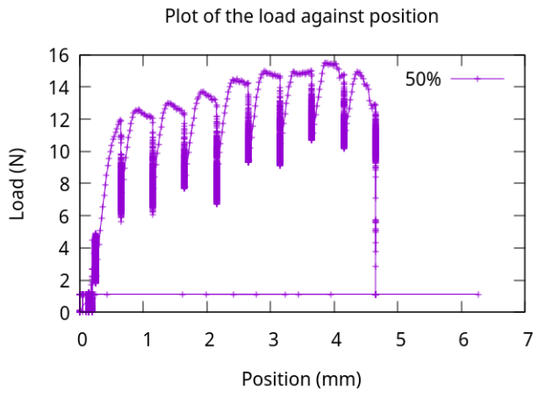

Figure A.1.: Stress-strain plot at around 50% RH

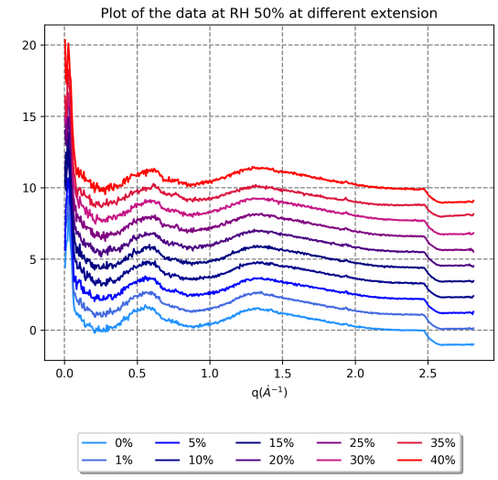

Figure A.2.: Waterfallplot at around 50% RH

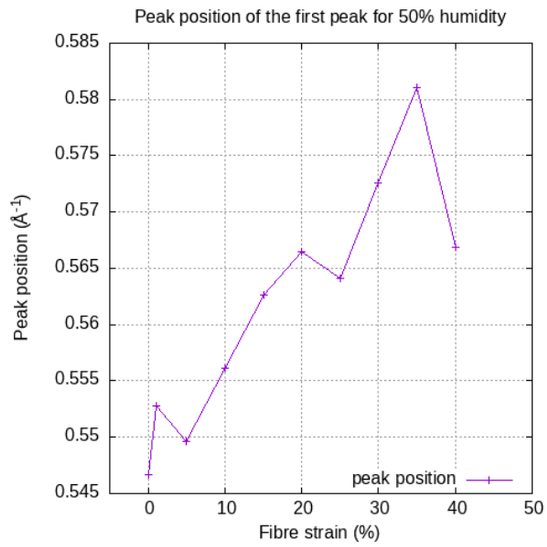

Figure A.3.: Plot of the first peak position (in $Å^{-1}$) depending on the elongation in percentage of the initial length.

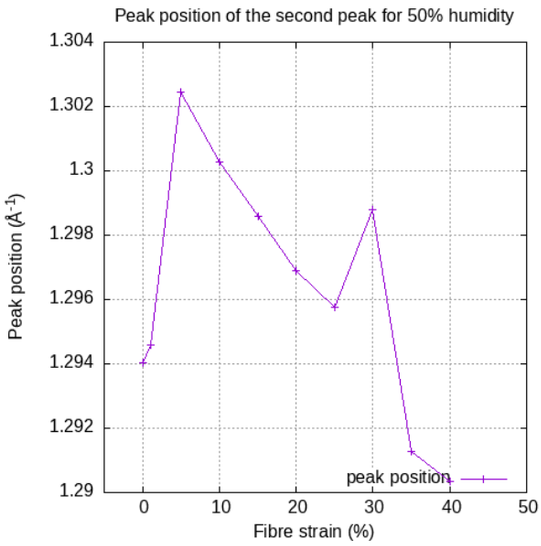

(a) Plot of the second peak position (in $Å^{-1}$) depending on the elongation in percentage of the initial length.

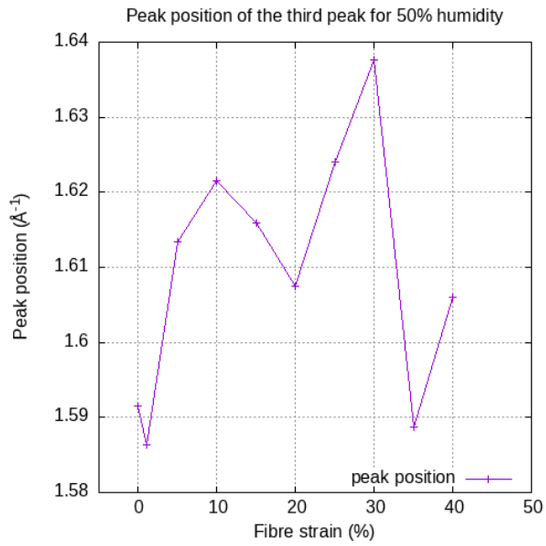

(b) Plot of the third peak position (in $Å^{-1}$) depending on the elongation in percentage of the initial length.

Figure A.4.: Position of the second and third peaks depending on the fibre strain.

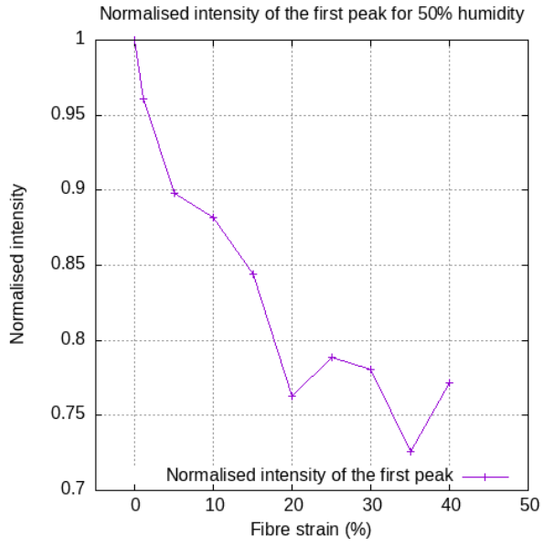

Figure A.5.: Plot of the relative intensity of the first peak.

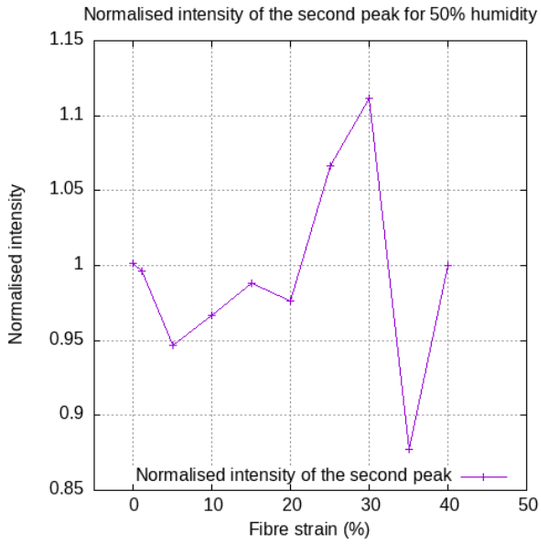

Figure A.6.: Plot of the relative intensity of the second peak

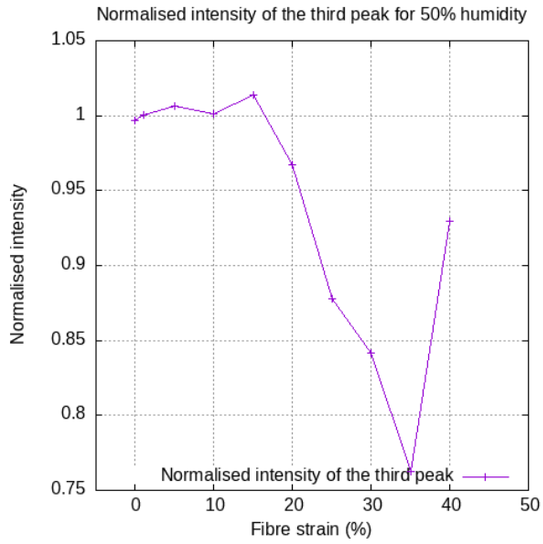

Figure A.7.: Plot of the relative intensity of the third peak.

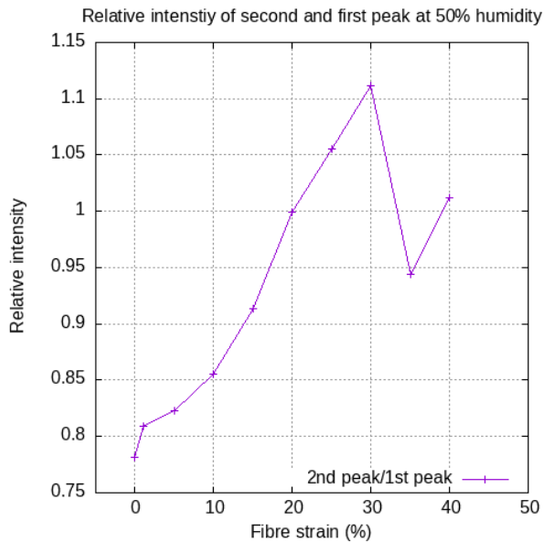

Figure A.8.: Plot of the intensity ratio between the second and the first peak.

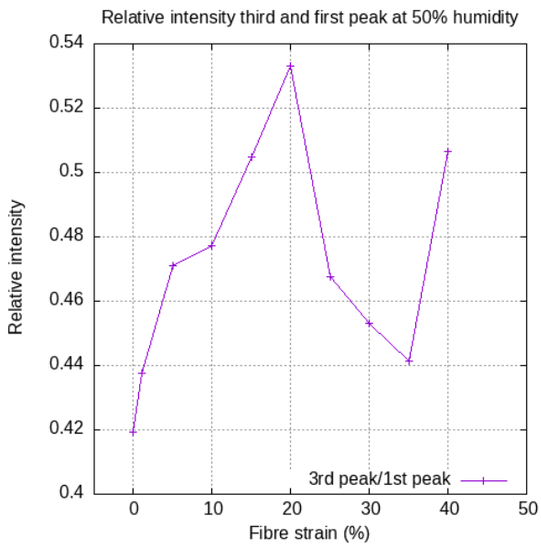

Figure A.9.: Plot of the intensity ratio between the third and the first peak.

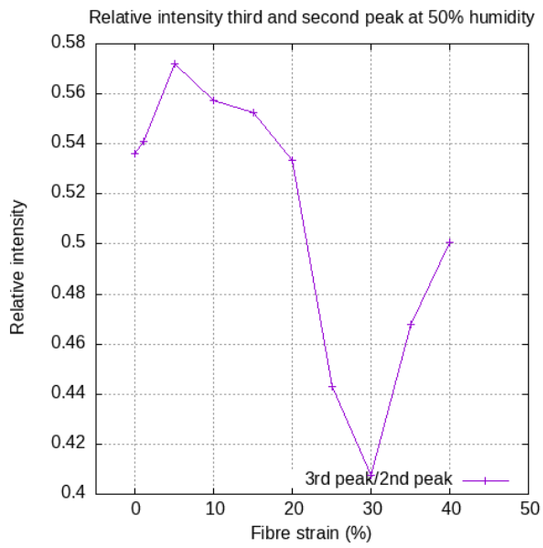

Figure A.10.: Plot of the intensity ratio between the third and the second peak.

A.2. Uncertainties calculation

Gnuplot script have been used to make the plots and to propagate the errors for the height ratios.
In this section are the programms and the gnuplot scripts used to compute the uncertainties in the fits. The pyhton programm is written by Martin Haßler and is part of a bigger library he wrote.
The gnuplot scripts is the one used for the series at 20% RH but a similar was used for all of them, to plot the data and to propagate the uncertainties in the height ratios.

A.2.1. Python code

```
# -*- coding: utf-8 -*-
"""
Created on Thu Feb 12 11:54:21 2026

@author: hassler
"""



from glob import iglob
import numpy as np
from scipy.stats import skewnorm
from scipy.stats import cauchy, norm

def skewSkewGauss(x, centreG, sigmaG, skewG, bG,):
    "skew_gauss"
    return bG*skewnorm.pdf(x, loc=centreG, scale=sigmaG, a=skewG)

def skewSkewGaussRaw(x, centreG, sigmaG, skewG):
    "skew_gauss_only_integral_part"
    V = 2./(sigmaG*np.sqrt(2.*np.pi))*np.exp(-(x-centreG)**2/2./sigmaG**2)
    return skewnorm.pdf(x, loc=centreG, scale=sigmaG, a=skewG)/V

def statsSkewGauss(centreG, sigmaG, skewG, bG, centreGSTD, sigmaGSTD,
     skewGSTD, bGSTD):
    delta = skewG/np.sqrt(skewG**2+1.0)
    muz = np.sqrt(2.0/np.pi)*delta
    sigz = np.sqrt(1.0-muz**2)
    gam1 = (4.0-np.pi)/2.0*(muz/sigz)**3
    # gam1 = (4.0-np.pi)/2.0*(delta*np.sqrt(2.0/np.pi))**3/(1.0-2.0*delta**2/np.pi
     )**1.5

    m0 = muz-gam1*sigz/2.0-np.sign(skewG)/2.0*np.exp(-2.0*np.pi/np.abs(skewG
     )) # eq. 2.33 "The Skew-Normal and Related Families" ISBN 9781139248891 p
     33.
    mode = centreG+sigmaG*m0

    height = skewSkewGauss(mode, centreG, sigmaG, skewG, bG)


    m0AlphaDelta = np.sqrt(2.0/np.pi)-(1.-np.pi/4.)*(3.*(2./np.pi)**3*delta
     **2*(1.-2./np.pi*delta**2)+((np.sqrt(2./np.pi)*delta)**3)*4./np.pi*delta)
     /(1.-2./np.pi*delta**2)**2
    deltaAlpha = 1./((1.+skewG**2)*np.sqrt(1.+skewG**2))
```

```
    sigMode2 = centreGSTD**2 + m0**2*sigmaGSTD**2 + (deltaAlpha*
     m0AlphaDelta*skewGSTD)**2

    sigMode = np.sqrt(sigMode2)

    x = mode

    eta = skewG*(x-centreG)/sigmaG
    dSeta = skewSkewGaussRaw(eta, centreG, sigmaG, skewG)
    V = 2./(sigmaG*np.sqrt(2.*np.pi))*np.exp(-(x-centreG)**2/2./sigmaG**2)


    sigHeight2 = (bG*skewGSTD*(V*dSeta*(x-centreG)/sigmaG))**2  # dalpha
    sigHeight2 = sigHeight2 + (bG*sigmaGSTD* ((2./np.sqrt(2.*np.pi)*(-1/sigmaG
     **2) * np.exp(-(x-centreG)**2/2./sigmaG**2) +
                                        V*(( x-centreG)**2/sigmaG**3))*
     skewSkewGaussRaw(mode, centreG, sigmaG, skewG)   +
                                       V*dSeta*(-skewG*(mode-centreG)/sigmaG**2))
     )**2  # domega

    sigHeight2 = sigHeight2 + (bG*centreGSTD*((V*(x-centreG)/sigmaG**2)*
     skewSkewGaussRaw(mode, centreG, sigmaG, skewG)   +    V*dSeta*(skewG/
     sigmaG*x)))**2  # d xi



    sigHeight2 = sigHeight2 + (bG*sigMode*((-V*(x-centreG)/sigmaG**2)*
     skewSkewGaussRaw(mode, centreG, sigmaG, skewG)   +    V*dSeta*(-skewG/
     sigmaG*centreG)))**2  # d x

    sigHeight2 = sigHeight2 + (bGSTD*(skewSkewGauss(x, centreG, sigmaG, skewG,
      bG,)))**2

    sigHeight = np.sqrt(sigHeight2)

    varianz = sigmaG**2*(1-2.*delta**2/np.pi)*bG

    return mode, sigMode, varianz, height, sigHeight



def Lorentz(x,centre1, sigma1, a1):
    return a1*cauchy.pdf(x, loc=centre1, scale=sigma1)


def FWHMLorentz(centre1, sigma1, a1, height,mode):
    h2 = height/2.0
    left = np.linspace(0,mode,500)
    ileft = 0
    iright= 499
    right = left + mode
    yleft = Lorentz(left,centre1, sigma1, a1)
    yright = Lorentz(right,centre1, sigma1, a1)
    ileft = np.argmax(yleft>h2)
    iright = np.argmax(yright<h2)
    # print(ileft, iright, h2, yleft[0], yright[499])
    if(ileft==0 or iright ==499):
        print("lorentz varianz failed")
```

```
        sdfsd
    return ((right[iright] - left[ileft])/2.0)**2


def statsLorentz(centre1, sigma1, a1,centre1STD, sigma1STD, a1STD):

    mode = centre1
    sigMode = centre1STD

    stats = list(cauchy.stats(scale=sigma1, loc=centre1, moments='mvsk'))
    height = Lorentz(mode,centre1, sigma1, a1)
    varianz = np.empty_like(mode)
    for i in range(0,len(mode)):
        varianz[i] = FWHMLorentz(centre1[i], sigma1[i], a1[i], height[i], mode[i])


    l = cauchy.pdf(mode, loc=centre1, scale=sigma1)

    sigHeight2 = (l*a1STD)**2 +(2.*(mode-centre1)*l**2*np.pi/sigma1*sigMode)
     **2
    sigHeight2 = sigHeight2 + (2.*(mode-centre1)*l**2*np.pi/sigma1*centre1STD)
     **2
    sigHeight2 = sigHeight2 + ((2.*(mode-centre1)**2*l**2*np.pi/sigma1**2-l/
     sigma1)*sigma1STD)**2

    sigHeight = np.sqrt(sigHeight2)
    return mode, sigMode, varianz, height, sigHeight


def Gauss(x,centre2, sigma2, a2):
    return a2*norm.pdf(x, loc=centre2, scale=sigma2)



def statsGauss(centre2, sigma2, a2,centre2STD, sigma2STD, a2STD):

    mode = centre2
    sigMode = centre2STD
    varianz = sigma2*a2
    height = Gauss(mode,centre2, sigma2, a2)

    g = norm.pdf(mode, loc=centre2, scale=sigma2)

    sigHeight2 = (g*a2STD)**2+(a2*g*(centre2**2-sigma2**2-2.*centre2*mode+
     mode**2)/sigma2**3*sigma2STD)**2
    sigHeight2 = sigHeight2 + (a2*g*(centre2-mode)/sigma2**2*sigMode)**2
    sigHeight2 = sigHeight2 + (a2*g*(mode-centre2)/sigma2**2*centre2STD)**2

    sigHeight = np.sqrt(sigHeight2)
    return mode, sigMode, varianz, height, sigHeight


path= r"/home/louloute/CoursMaster/MasterThesis/10mm/AFit"

for folder in iglob(path+'/integration?0p'):
    folderin = folder+'/fits/'
    print(folder)
```

```
    seqNum, Extension, centreG, centreGSTD, sigmaG, sigmaGSTD, skewG,
     skewGSTD, bG, bGSTD = np.loadtxt(folderin+r'
     skewGaussskewLorentz_h_fitData.dat',dtype=np.float64,unpack=True,skiprows
     =4, delimiter='␣' , usecols =(0,19,13,14,15,16,17,18,11,12))
    seqNum2, a1, a1STD, centre1, centre1STD, sigma1, sigma1STD, a2, a2STD,
     centre2, centre2STD, sigma2, sigma2STD = np.loadtxt(folderin+r'3
     peaks_h_fitData.dat',dtype=np.float64,unpack=True,skiprows=4, delimiter='␣' ,
      usecols =(0,11,12,13,14,15,16,17,18,19,20,21,22))
    resultSkew = statsSkewGauss(centreG, sigmaG, skewG, bG, centreGSTD,
     sigmaGSTD, skewGSTD, bGSTD)
    resultLorentz = statsLorentz(centre1, sigma1, a1,centre1STD, sigma1STD, a1STD
     )
    resultGauss = statsGauss(centre2, sigma2, a2,centre2STD, sigma2STD, a2STD)

    with open(folderin+'PeakStatError.dat', 'w') as f:
        f.write("Seq1␣Seq2␣Ext␣ModeSkewNorm␣ModeSkewNormSTD␣VarSkewNorm␣
     HeightSkewnorm␣HeightSkewNormSTD␣ModeLorentz␣ModeLorentzSTD␣
     VarLorentz␣HeightLorentz␣HeightLorentzSTD␣"+
                "ModeGauss␣ModeGaussSTD␣VarGauss␣HeightGauss␣HeightGaussSTD
     \n")
        for i in range(0,len(seqNum)):
            f.write(str(seqNum[i])+'␣' +str(seqNum2[i])+'␣' +str(Extension[i])+'␣' +
                    str(resultSkew[0][i])+'␣' +str(resultSkew[1][i])+'␣' +str( resultSkew[2][i
    ])+'␣' +str( resultSkew[3][i])+'␣' +str( resultSkew[4][i])+'␣' +
                    str(resultLorentz[0][i])+'␣' +str(resultLorentz[1][i])+'␣' +str(
     resultLorentz[2][i])+'␣' +str(resultLorentz[3][i])+'␣' +str(resultLorentz[4][i])+'␣'
     +
                    str(resultGauss[0][i])+'␣' +str(resultGauss[1][i])+'␣' +str(resultGauss
     [2][i])+'␣' +str(resultGauss[3][i])+'␣' +str(resultGauss[4][i])+'\n')




    # for i in range(0,16):
    #     print(seqNum[i], result[0][i], result[1][i], result[2][i], result[3][i], result[4][i])




    # Peaks3= np.loadtxt(folder+r'3peaks_h_fitData.dat',dtype=np.float64,unpack=
     False,skiprows=4, delimiter=' ')
```

A.3. Programm for background subtraction

```
#!/usr/bin/env python3
# −*− coding: utf−8 −*−
"""
Created on Fri Apr 25 15:07:11 2025

@author: louloute
"""
import csv
from pathlib import Path
import numpy  as np
import matplotlib.pyplot as plt
import os
from glob import glob
from os.path import basename
```

```
base_path = Path(__file__).parent
os.chdir("/home/louloute/CoursMaster/MasterThesis/10mm/AFit/BailsDeBG") #à
    changer ici
fpath=r"/home/louloute/CoursMaster/MasterThesis/10mm/AFit/BailsDeBG" #à
    changer ici


from os import getcwd, chdir
current_dir = getcwd()
print("New working directory:", getcwd())



                #import the background
v=[]
b=[]
with open('RHBG_12__inte_00000.dat') as bg: #à changer ici
    plots = csv.reader(bg, delimiter='  ')
    name = basename('RHBG_12__inte_00000.dat').split('_')[1]
    for row in plots:
        v.append(float(row[0]))
        b.append(float(row[1]))



                #import the data files in the folder
#for dat in glob(fpath + "/SU*.dat"):
counter=0
colour=["red","blue","orange","rebeccapurple","coral","lightblue","darkorange","
    firebrick","olive","slategrey","crimson","pink","darkgreen","moccasin","grey","
    peru","tomato","navy","deeppink"]
for dat in glob(fpath + "/RH2**.dat"):
    counter=counter+1
    u=[]
    a=[]
    with open(dat) as f:
        plots = csv.reader(f, delimiter='       ')
        naame = basename(dat).split('_')[1]
        for row in plots:
            u.append(float(row[0]))
            a.append(float(row[1]))
        #plt.scatter(u, a,c="green", label='test'+str(name) + '.dat',marker='+')
                #background subtraction
    y=[]
    for r in range(len(u)):
        y.append(float(a[r])-float(b[r])*0.9)
    #plt.scatter(u, a,c="blue", label='testBGsub'+str(name) + '.dat',marker='+')
    plt.scatter(u, y,c=colour[counter], label=str(name),marker='+') #à changer ici
                #saving the plot in images
    plt.xlabel("q(nm$^{-1}$)")
    plt.ylabel("Intensity AU")
    print('j\'ai mes loubou qui claquent','tulu'*counter)
plt.scatter(u, b,c='black', label="bg",marker='+') #à changer ici
plt.legend(loc='upper right', bbox_to_anchor=(0, 1))

plt.savefig('BG-compare'+str(name) +'.png') #à changer ici
plt.show()

                #saving the data in texte files
```

```
data = np.column_stack((u, y))
np.savetxt('BG-compare'+str(name) +'.txt' , data) #à changer ici

print("u=",u)
print("y=",y)


print('no_shade')

"""
A=[]
for i in a:
    A.append((i)/1.9302021E+04)
"""
#os.chdir("/home/louloute/CoursMaster/MasterThesis/Files/Data/p1/")


"""
B=[]
for i in b:
    B.append((i-1.7500011E+02)/2.1483600E+04)

#UHU100
file_UHU100 = ("../doc py/wireUHU100PLOT.txt").resolve()

v=[]
b=[]
with open(file_UHU100) as f:
    plots = csv.reader(f, delimiter=',')
    for row in plots:
        v.append(float(row[2]))
        b.append(float(row[3]))

#LOC15
file_LOC15 = (base_path / "../doc py/wireLOC15PLOT.txt").resolve()

w=[]
c=[]
with open(file_LOC15) as f:
    plots = csv.reader(f, delimiter=',')
    for row in plots:
        w.append(float(row[2]))
        c.append(float(row[3]))

#LOC100
file_LOC100 = (base_path / "../doc py/wireLOC100PLOT.txt").resolve()

x=[]
d=[]
with open(file_LOC100) as f:
    plots = csv.reader(f, delimiter=',')
    for row in plots:
        x.append(float(row[2]))
        d.append(float(row[3]))

#EPO15
file_EPO15 = (base_path / "../doc py/wireEPO15PLOT.txt").resolve()
```

```
y=[]
e=[]
with open(file_EPO15) as f:
    plots = csv.reader(f, delimiter=',')
    for row in plots:
        y.append(float(row[2]))
        e.append(float(row[3]))

#EPO100
file_EPO100 = (base_path / "../doc py/wireEPO100PLOT.txt").resolve()

z=[]
g=[]
with open(file_EPO100) as f:
    plots = csv.reader(f, delimiter=',')
    for row in plots:
        z.append(float(row[2]))
        g.append(float(row[3]))


plt.scatter(u, A,color='darkred',marker='.') #data
plt.scatter(v, B,color='darkblue',marker='.') #data

plt.scatter(u, a,c="green", label='UHU15')
plt.scatter(v, b,c="lightgreen", label ="UHU100")
#plt.scatter(w, c,c="red", label ="LOC15")
#plt.scatter(x, d,c="orange", label ="LOC100")
#plt.scatter(y, e,c="blue", label ="EPO15")
#plt.scatter(z, g,c="cyan", label ="EPO100")

plt.legend(loc='upper left', bbox_to_anchor=(0, 1))


plt.xlabel("Extension(mm)")
plt.ylabel("Load(Na)")

plt.show()
"""
```

Kurzfassung

Die vorliegende Arbeit hat zum Ziel, einen Aspekt der strukturellen Veränderungen in menschlichen Haaren unter feuchten Bedingungen und longitudinaler Belastung der Fasern darzustellen. Frühere Studien zu Haarfasern haben Hinweise auf einen strukturellen Übergang in Keratin von α- zu β-Konfiguration bei verschiedenen Arten geliefert, während die Haarfasern in Wasser oder Dampf gedehnt wurden. Dies zeigt die Bedeutung von Feuchtigkeit und Spannung für komplexe biologische Materialien wie Säugetierhaare. Diese Arbeit baut auch auf einer früheren These von Johannes Liebhart auf, mit dem Ziel, einige der dort auftretenden Probleme zu lösen und herauszufinden, ob Dampf notwendig ist und ob der α- zu β-Übergang ab einer bestimmten Schwelle stattfindet. Um die Qualität der Ergebnisse im Vergleich zur vorherigen Arbeit zu verbessern, wurde ein neues Fenster entwickelt, das größer war und mit einer Kunststofffolie verschlossen wurde, um die Feuchtigkeitsbedingungen zu garantieren. Das Experiment wurde dann bei relativen Luftfeuchtigkeiten von 20 %, 40 %, 60 % und 80 % durchgeführt, wobei die Belastung eines Bündels von 20 Fasern während der Messung schrittweise erhöht wurde. Der äquatoriale Teil des Musters wurde hier untersucht und spiegelt im reziproken Raum die Faserorganisation über den Querschnitt wider; Für die vorhandenen Entfernungen bietet es Zugang zum Abstand zwischen den intermediären Filamenten, zur Größe der Keratinketten, deren Abstand und deren Entwicklung unter zunehmender Spannung.

Bei unterschiedlichen Dehnungen und bei jeglichen Luftfeuchtigkeiten wurden keine signifikanten Änderungen wie Erscheinen oder Verschwinden von Peaks in den Röntgendiagrammen beobachtet. Während des gesamten Dehnungsprozesses traten jedoch nur allmähliche Veränderungen in den SAXS-Bildern und in der Mechanik der Fasern von niedriger zu hoher Luftfeuchtigkeit auf. Diese Ergebnisse deuten auf keinen plötzlichen Übergang von α-Helices zu β-Sheets hin, aber die Veränderungen in den Peak-Positionen sowie in den Peak-Intensitäten geben Hinweise darauf, wie sich menschliches Haar während der Dehnung verformt.

Diese Ergebnisse unterscheiden sich grundlegend von denen in der Literatur, in denen man bei Pferdehaar eine signifikante Änderung der Röntgendaten fand, die als α-zu-β-Übergang interpretiert wurden. Solche grundlegenden Unterschiede zwischen menschlichem und Pferdehaar - der α-zu-β-Übergang in Pferdehaar, der im menschlichen Haar fehlt, könnten auf Unterschiede in ihrer inneren Zusammensetzung und Struktur zurückgeführt werden. Eine weitere mögliche Ursache könnte sein, dass beide, Spannung und Dampf, notwendig sind, um solche Veränderungen zu beobachten.

Weitere SAXS-Untersuchungen an Pferdehaaren und menschlichem Haar sowie zusätzliche Spektroskopiemessungen sollten die Unterschiede in der Haarstruktur der beiden Lebewesen, Pferd und Mensch, klären.